



A New Limit of the Flux Ratio He/He in Cosmic Rays

Sasaki, Makoto

(Degree)

博士 (理学)

(Date of Degree)

2000-03-31

(Date of Publication)

2015-10-20

(Resource Type)

doctoral thesis

(Report Number)

甲2080

(JaLCD0I)

<https://doi.org/10.11501/3173019>

(URL)

<https://hdl.handle.net/20.500.14094/D1002080>

※ 当コンテンツは神戸大学の学術成果です。無断複製・不正使用等を禁じます。著作権法で認められている範囲内で、適切にご利用ください。



A New Limit on the Flux Ratio
 $\overline{\text{He}}/\text{He}$ in Cosmic Rays

By
SASAKI Makoto

Graduate School of Science and Technology
Kobe University

2000

Abstract

We have searched for antihelium in the cosmic rays using the BESS¹ balloon-borne magnetic spectrometer in every summer since 1993. Up to now, we have six successful scientific flights and achieved 100 hours data taking time. In this paper, we analyzed the data which were obtained in 1997 and 1998. The total number of collected helium nuclei was 6.2×10^6 . No antihelium candidates were found in this sample over the rigidity from 1 to 16 GV/c. Combined with previous data, the resulting upper limit for the ratio of antihelium to helium in cosmic rays over this region is 8.8×10^{-7} at 95 % confidence.

¹Balloon-borne Experiment with a Superconducting magnet Spectrometer

Contents

1	Introduction	1
2	The Instrument	5
2.1	Detector Layout	5
2.1.1	Detector Configuration	5
2.1.2	Particle Identification	6
2.1.3	Issues Specific to Balloon Payload	7
2.2	Superconducting Solenoidal Magnet	10
2.3	Tracking	13
2.3.1	JET Chamber	13
2.3.2	Inner Drift Chamber	14
2.3.3	Chamber Gas	16
2.3.4	High Voltages	17
2.3.5	Readout Electronics	17
2.3.6	Performance of Tracking System	18
2.4	Time Of Flight Hodoscope	27
2.4.1	TOF Hodoscopes	27
2.4.2	Electronics and Signal Processing	29
2.4.3	Performance of TOF System	29
2.4.4	dE/dx Measurement	31
2.5	Aerogel Čerenkov Counter	34
2.6	Data Acquisition System	36
2.6.1	Trigger	36
2.6.2	Event Building	40
2.6.3	Transputer Bank	41
2.6.4	Data Strage	42
2.6.5	Monitor	43
2.6.6	Communication	43

3	Flights Status	45
3.1	BESS-97 Scientific Flight	45
3.2	BESS-98 Scientific Flight	45
3.3	Trigger conditions	46
4	Search for Antihelium	51
4.1	Flight Data Sample	51
4.2	Event Reconstruction	54
4.2.1	Track Reconstruction	54
4.2.2	Time-of-Flight Measurement	56
4.2.3	dE/dx Measurement	58
4.3	Event Selections	60
4.3.1	Single Track Selection	60
4.3.2	β Selection	61
4.3.3	dE/dx selection	62
4.4	Track Quality Cut	70
4.5	Antihelium Search	79
5	Determination of the upper limit on $\overline{\text{He}}/\text{He}$	81
5.1	Ionization Energy Loss	82
5.2	Monte Carlo Simulation	82
5.2.1	Geometrical Acceptance	83
5.2.2	Single Track Efficiency	83
5.2.3	Loss of He and $\overline{\text{He}}$ in the air	84
5.3	Trigger Efficiency	85
5.4	Off-line Selection Efficiency	86
5.4.1	β Cut Efficiency	86
5.4.2	dE/dx Cut Efficiency	87
5.4.3	Track Quality Cut Efficiency	87
5.5	Upper limit on $\overline{\text{He}}/\text{He}$	87
6	Results	97

List of Figures

1.1	Summary of the experiments setting upper limit on $\overline{\text{He}}/\text{He}$. Saeki, et al (1998) [8]	4
2.1	Cross section of the BESS detector.	5
2.2	A typical helium event (top) and an event with interaction (bottom).	9
2.3	Cross section of the superconducting solenoid.	10
2.4	Flux line (top) and field strength contour (bottom) of the superconducting solenoid.	12
2.5	Schematic view of the JET chamber.	13
2.6	Schematic view of IDC. The cross sections shows in a circle. . .	15
2.7	Read-out scheme for IDC signals.	16
2.8	Fitting residuals for (a)JET and for (b)IDC in r - φ plane. . .	20
2.9	JET chamber r - φ resolution as a function of the drift distance.	21
2.10	Residual distribution of the JET chamber along the z -coordinate.	22
2.11	Scatter plot of the ε parameter of the inner (ε_I) and outer (ε_O) pad.	23
2.12	Residual distribution of the IDC along the z -coordinate. . . .	24
2.13	dE/dx measurement by JET.	25
2.14	TOF counter module in BESS-97 and 98 detector.	28
2.15	Scatter plot of $1/\beta$ vs. rigidity for cosmic-ray data at ground- level using cuts of dE/dx , track quality, and $1/\beta < 1.2$	30
2.16	The ΔT distribution for BESS data at ground-level.	31
2.17	Scatter plots of dE/dx versus rigidity for down-going positive- charged particles (a) at the top counters and (b) at the bot- tom counters.	32
2.18	Overview of the aerogel Čerenkov counter.	34
2.19	Basic concept of the Track Trigger.	38
2.20	Block diagram of TT process.	39

2.21	Simulated (solid line) and measured (dot) Track Trigger efficiency for the antiproton search.	40
2.22	Block diagram of the data acquisition system.	41
3.1	House-keeping data on altitude, temperatures and pressures in BESS '97 flight.	47
3.2	House-keeping data on altitude, temperatures and pressures in BESS '98 flight.	48
3.3	Flight trajectory for BESS '97.	49
3.4	Flight trajectory for BESS '98.	49
4.1	Method of the rigidity measurement	55
4.2	Method of the TOF measurement	57
4.3	β^{-1} vs. rigidity ('97)	61
4.4	β^{-1} vs. rigidity ('98)	62
4.5	dE/dx(upper) vs. rigidity after β cut ('97)	63
4.6	dE/dx(upper) vs. rigidity after β cut ('98)	64
4.7	dE/dx(lower) vs. rigidity after β cut ('97)	65
4.8	dE/dx(lower) vs. rigidity after β cut ('98)	66
4.9	dE/dx(JET) vs. rigidity after β cut ('97)	67
4.10	dE/dx(JET) vs. rigidity after β cut ('98)	68
4.11	dE/dx(upper) distribution at various rigidities.	69
4.12	Track Quality Cut 1,2,3,4. ('97)	72
4.13	Track Quality Cut 1,2,3,4. ('98)	73
4.14	Track Quality Cut 5. ('97 (top) and '98(bottom))	74
4.15	Track Quality Cut 6. ('97)	75
4.16	Track Quality Cut 6. ('98)	76
4.17	Track Quality Cut 7. ('97)	77
4.18	Track Quality Cut 7. ('98)	78
4.19	1/rigidity distribution without track quality cut ('97 + '98)	79
4.20	1/rigidity distribution ('97 + '98)	80
5.1	Acceptance	84
5.2	Single Efficiency	85
5.3	Survival probability of helium nuclei (filled squares) and antihelium (open squares) for 5 g/cm ² of the atmosphere.	90
5.4	Track pattern selection efficiency.	91
5.5	Track rigidity selection efficiency.	92
5.6	Online selection efficiency.	93
5.7	The efficiency of the various quality cuts	94

5.8	The efficiency of the all quality cut	95
5.9	The antihelium efficiency-product in the energy region.	96
6.1	Upper limit	98

List of Tables

1.1	Summary of experiments setting upper limit on $\overline{\text{He}}/\text{He}$	3
2.1	Summary of the material thickness in g/cm^2	8
2.2	Main parameters of the superconducting solenoidal magnet (MAG).	11
2.3	Parameters of tracking chambers.	26
2.4	Parameters of TOF counters.	27
2.5	Summary of the track trigger selection patterns. $(i, j, k, l)_p$ means the permutation $(N_{iu}, N_{il}, N_{tu}, N_{tl})$ matches (i, j, k, l) , where N_{iu} – the number of hit-cells in upper IDC, N_{il} – the number of hit-cells in lower IDC, N_{tu} – the number of hit-cells in upper TOF and N_{tl} – the number of hit-cells in lower TOF.	39
3.1	The conditions of the T0 trigger and the trigger rates	46
3.2	The settings of the Master Trigger and the trigger rate ('97 and '98)	50
4.1	Summary of BESS flight data ('97)	52
4.2	Summary of BESS flight data ('98)	53
5.1	Summary of the number of heliums and minimum efficiency-product of antihelium.	89
5.2	Summary of the calculation of upper limit with model dependent assumption.	89

Chapter 1

Introduction

Whether the Universe all consists of the matter or not? This question arose in 1928 when Dirac proposed the existence of antiparticle based on relativistic quantum mechanics. It is not obvious from the laws of nature that the Universe consists only of the matter, but we have to recognize it from the fact of observations, at least within the galaxy.

An idea to understand the matter-antimatter asymmetry in the Universe from first principles has been studied for the last several decades, and has been an important issue both for cosmology and particle physics. But so far, it seems safe to say that there is no concrete theory for matter-antimatter asymmetry despite a vast effort.

According to the current understanding of Big Bang cosmology, at the very beginning of the Universe there must have been the same amount of matter and antimatter. If we believe it, we must evolve the matter and antimatter asymmetry at present from the symmetric initial state. It is shown that to resolve this problem, three basic ingredients are needed.

- an interaction which violates baryon number conservation must be allowed,
- an interaction which violates C and CP conservation must be allowed,
- a period out of thermal equilibrium is required.

They were first mentioned by Sakharov [1] and called ‘Sakharov conditions’. It is obvious that the first condition is needed. If baryon number was conserved in all interactions, the net baryon number of the Universe remained in a symmetric initial state, i.e. zero. It is the matter-antimatter symmetric state. Although B-nonconserving interactions were allowed, it is not enough

to generate non-zero net baryon number. Because of the symmetry of the physical law, even if an interaction to produce baryon excesses was allowed, it is also allowed that a mirror interaction to produce antibaryon excesses, consequently maintaining zero net baryon number. The second condition is necessary to avoid such cancel out. The last condition is a request of thermodynamics, and is met in standard Big Bang cosmology.

The modern grand unified theories (GUTs), now most generally accepted one, the goal of the theories is to unify the strong, weak, and electromagnetic interactions and the quarks and leptons within the framework of a gauge field theory, satisfy first two conditions. GUTs predict the existence of X-particle whose mass is $M_X \sim 10^{15}$ GeV and this particle have two dominant decay modes:

$$X \rightarrow q + q \quad (\bar{X} \rightarrow \bar{q} + \bar{q}), \quad X \rightarrow \bar{q} + \bar{l} \quad (\bar{X} \rightarrow q + l)$$

where q (\bar{q}) labels a quark (antiquark) and f (\bar{f}) labels a fermion (antifermion). Since the two final states have different baryon number, the decays of X bosons violate B. It is not obvious that C and CP is violated in the decay of X bosons. However, CP violation is observed in the neutral kaon system and since its origin is not well understood, it is easy to imagine that C and CP violation manifest themselves in all sectors of the theory, including the superheavy boson sector. Here, we should be noted that the theory do not mention about the type of CP violation. If CP violation is explicit in the Lagrangian, the sign of the CP violation will determine whether matter or antimatter prevails throughout the entire Universe. However, if the CP violation is arising from spontaneous symmetry breaking at some time as the Universe cools, the Universe will have a domain structure of baryon number.

The absence of annihilation radiation from the nearby clusters of galaxies shows that little antimatter is to be found within ~ 20 Mpc. However it is not completely excluded that there are regions of antimatter in the far-off distance and cosmic rays from such antimatter domains might be able to diffuse across intergalactic space and enter our Galaxy. Since the probability to produce antihelium in collisions of cosmic ray with the interstellar medium is too small, if one antihelium candidate is observed, we must consider the event to be originated in the evolution of Early Universe mentioned above. In addition, as antihelium has negative charge, it is easy to identify experimentally.

The search for antihelium in cosmic rays is good to examine the evolution of Early Universe and give some information to elementary particle physics.

Some experiments searching for antihelium have been done and upper limit now $\overline{\text{He}}/\text{He} < 3.1 \times 10^{-6}$ was set [8] (See Fig. 1.1 and Table 1.1). In this dissertation, we report a more sensitive search for antihelium using the data from the '97 and '98 flights of the BESS detector.

Table 1.1: Summary of experiments setting upper limit on $\overline{\text{He}}/\text{He}$.

Rigidity(GV)	$\overline{\text{He}}/\text{He}$ limit	Reference
< 2.7	$< 7 \times 10^{-3}$	Aizu et al. (1961) [2]
$1 \sim 10$	$< 1 \times 10^{-3}$	Evenson et al. (1972) [3]
$10 \sim 25$	$< 8 \times 10^{-3}$	Evenson et al. (1972) [3]
$4 \sim 33$	$< 5 \times 10^{-4}$	Smoot et al. (1975) [4]
$33 \sim 100$	$< 2 \times 10^{-2}$	Smoot et al. (1975) [4]
$10 \sim 33$	$< 1.6 \times 10^{-4}$	Badhwar et al. (1978) [5]
$1 \sim 20$	$< 9 \times 10^{-5}$	Golden et al. (1997) [6]
$1 \sim 2$	$< 2.2 \times 10^{-5}$	Buffington et al. (1981) [7]
$1 \sim 16$	$< 3.1 \times 10^{-6}$	Saeki et al. (1998) [8]

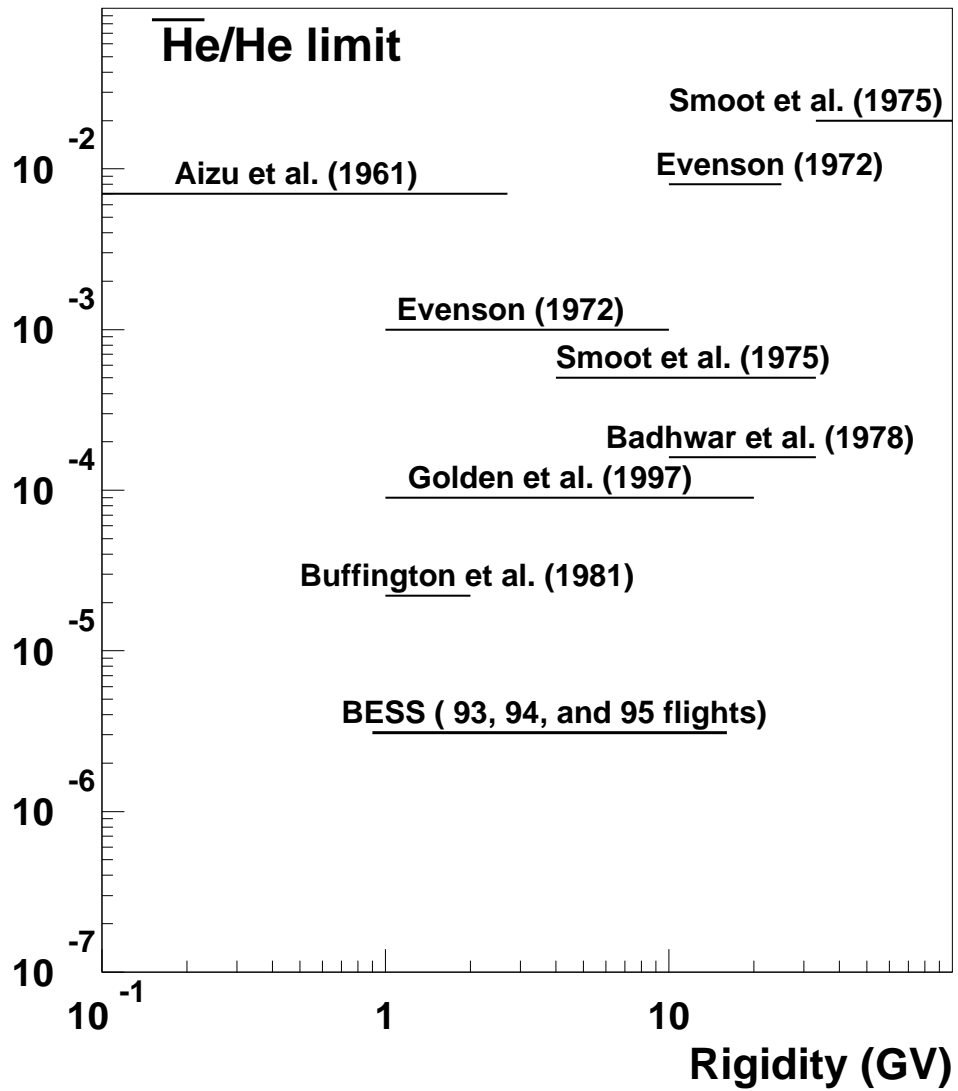


Figure 1.1: Summary of the experiments setting upper limit on $\bar{H}e/H$. Saeki, et al (1998) [8]

Chapter 2

The Instrument

2.1 Detector Layout

2.1.1 Detector Configuration

The detector components were arranged concentrically as shown in Figure 2.1. A particle traversing the apparatus passes through, from outside to

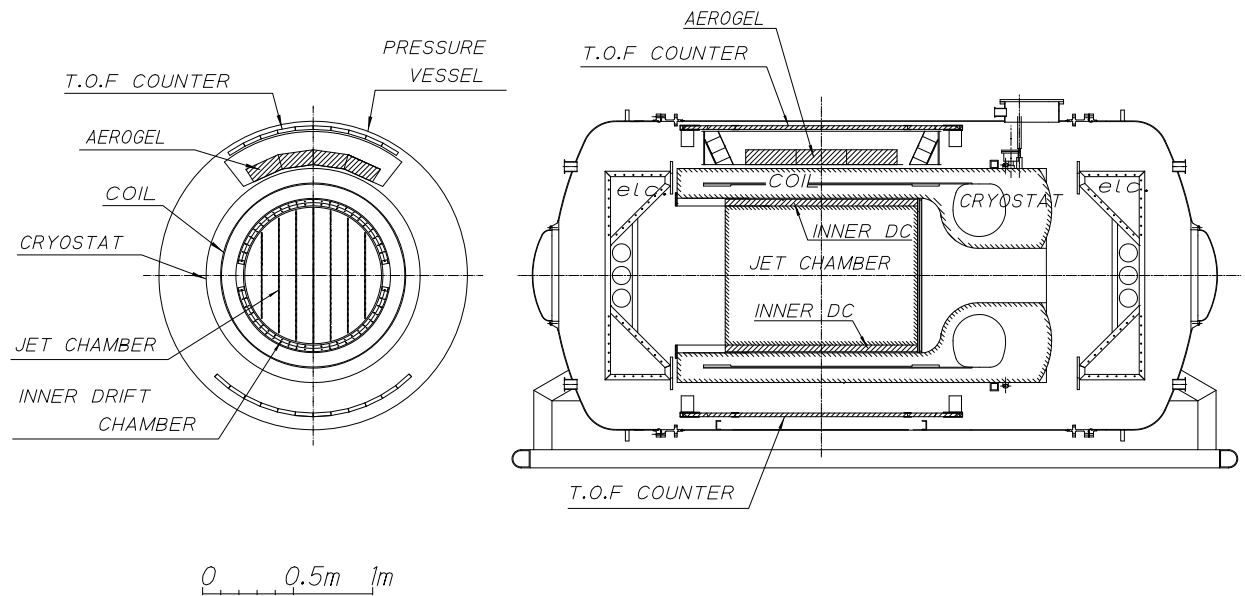


Figure 2.1: Cross section of the BESS detector.

inside, a plastic scintillator hodoscope (TOF), an Aerogel Čerenkov counter (AGL), a superconducting solenoid (MAG), two layers of inner drift chambers (IDC) before entering a central jet type drift chamber (JET). All these detector components were contained in a pressure vessel.

Solenoidal magnets have often been disfavored in previous cosmic ray experiments [10, 11, 12, 13, 14] because of the unavoidable material in the particle passage. However, a thin superconducting solenoid developed at KEK[15, 16, 17] enabled us to adopt this concentric configuration. The amount of material in the coil and its cryostat has been reduced to a level comparable to the material in the other detector components such as plastic scintillators, chamber walls and pressure vessel (see Table 2.1) and also to the residual air ($\sim 5 \text{ g/cm}^2$) above the detector.

The cylindrical configuration, usually used in the high energy collider experiments, has many advantages in the cosmic ray application too. A strong and uniform magnetic field are generated in a large volume inside the solenoid where a large and transparent tracking device can reside. Therefore a good momentum resolution is easily obtained while keeping the whole detector size compact. The detector has a wide-open geometry and the JET can fully “visualize” the incident track or any interactions inside the apparatus. Inelastic interactions accompanied by several secondary tracks can easily be identified (see Figure 2.2). A probability of charge mis-identification due to large angle scattering is negligibly small.

The uniform magnetic field strength over the large tracking volume assures an almost constant geometrical acceptance for a wide energy range. The acceptance changes only a few percent from the lowest detectable energy ($\sim 200 \text{ MeV}$) up to $> 100 \text{ GeV}$. The detector performance changes little for various hit positions and incident angles too. These characteristics are essential in the reliable determination of the absolute flux of the cosmic radiation.

We use hereafter a cylindrical coordinate system; r , φ and z , and a Cartesian coordinate; x , y and z , where y and z being the vertical axis and the axis of the solenoid, respectively.

2.1.2 Particle Identification

Particle identification in the BESS experiment is performed by mass reconstruction according to the relation, $m = ZeR\sqrt{1/\beta^2 - 1}$. The rigidity, momentum per charge ($R \equiv p/Ze$), is precisely measured by the reconstructed particle trajectory. The velocity, β , is derived from the path length and the time-of-flight between the upper and the lower layers of the TOF. The energy

deposit in the TOF provides the magnitude of the charge, Z , and additional information on the velocity according to the relation, $dE/dx \approx (Ze/\beta)^2 f(\beta)$. The sign of charge is determined by the deflection and the particle direction, up-going or down-going, determined by the TOF. The mass is finally calculated from these measurements. The electron/antiproton separation is performed by ACC. Antiprotons of energies below Cherenkov threshold are distinguished from the electrons, the main background to antiprotons.

2.1.3 Issues Specific to Balloon Payload

Since the apparatus is to be launched by a balloon, the performance of the detector should sometimes be compromised with the requirements specific to the balloon experiment. Weight and power are the primary issues. Since the lifting capacity of the balloon is limited, heavier weight on board results in a lower altitude be reached and thicker residual air above the apparatus. The more power requires more batteries, otherwise the flight time becomes short. Most of the electronics on board, including all the CAMAC (Computer Automated Measurement And Control) modules[18], are specially designed for this experiments. The functions of each module is carefully selected and minimized in order to simplify the circuits and to reduce their power consumption while keeping the signal processing speed as fast as possible.

Low power consumption also benefits the temperature control of the payload. The local temperature near certain power consuming components increases in the daytime and might reach to the maximum tolerable level. The optimization of heat insulation and ventilation to stabilize the temperature inside the vessel becomes a difficult task for high power dissipation.

Stray magnetic field is another issue. Since a magnet return yoke is too heavy to be loaded in the payload, a dipole magnetic field is maintained around the detector. Any detector components sensitive to the magnetic field should be properly treated. Detailed descriptions are given in the relevant sections.

As a balloon payload, the apparatus should be robust enough to withstand the impacts of launching, parachute opening and landing. It was estimated that a 10 G acceleration is applied to the detector. The support structure of each detector component was designed so that the 10 G acceleration would not cause fatal damage. As for the suspension system of the superconductor, we have performed mechanical analysis and have confirmed that the operating magnet did not quench during the 10 G impact test.

Table 2.1: Summary of the material thickness in g/cm².

	BESS-97	BESS-98
TOF (per counter)	2.10	2.10
Scintillator (Polystyrene)	2.06	2.06
Wrapping (Mylar, Vinyl)	0.04	0.04
AGL (per counter)	1.55	1.55
Honeycomb plate (Aramid, Aluminum)	0.18	0.18
Aerogel	1.02	1.02
Glue (Epoxy)	0.02	0.02
Aluminum plate	0.27	0.27
Reflector (Goretex)	0.03	0.03
Cardstock paper	0.03	0.03
MAGNET (per wall)	4.70	4.70
Coil (NbTi(Cu), Al stabilized)	1.88	1.88
Support Cylinder (Aluminum)	0.54	0.54
Super insulation (Mylar)	0.24	0.24
Cryostat (Aluminum honeycomb)	1.83	1.83
Glue (Epoxy)	0.21	0.21
IDC (per chamber)	0.64	0.64
Honeycomb plate (Aramid, Kapton)	0.14	0.14
Field shaping patterns (Copper)	0.10	0.10
Glue (Epoxy)	0.13	0.13
Aluminum plate	0.27	0.27
JET (per wall)	0.17	0.17
Honeycomb plate (Aramid, Kapton)	0.07	0.07
Field shaping patterns (Copper)	0.05	0.05
Glue (Epoxy)	0.05	0.05
Pressure Vessel (per wall)	0.67	0.67
Vessel wall (Aluminum)	0.54	0.54
Gas (CO ₂ /Ar)	0.13	0.13
Total thickness	9.83	9.83

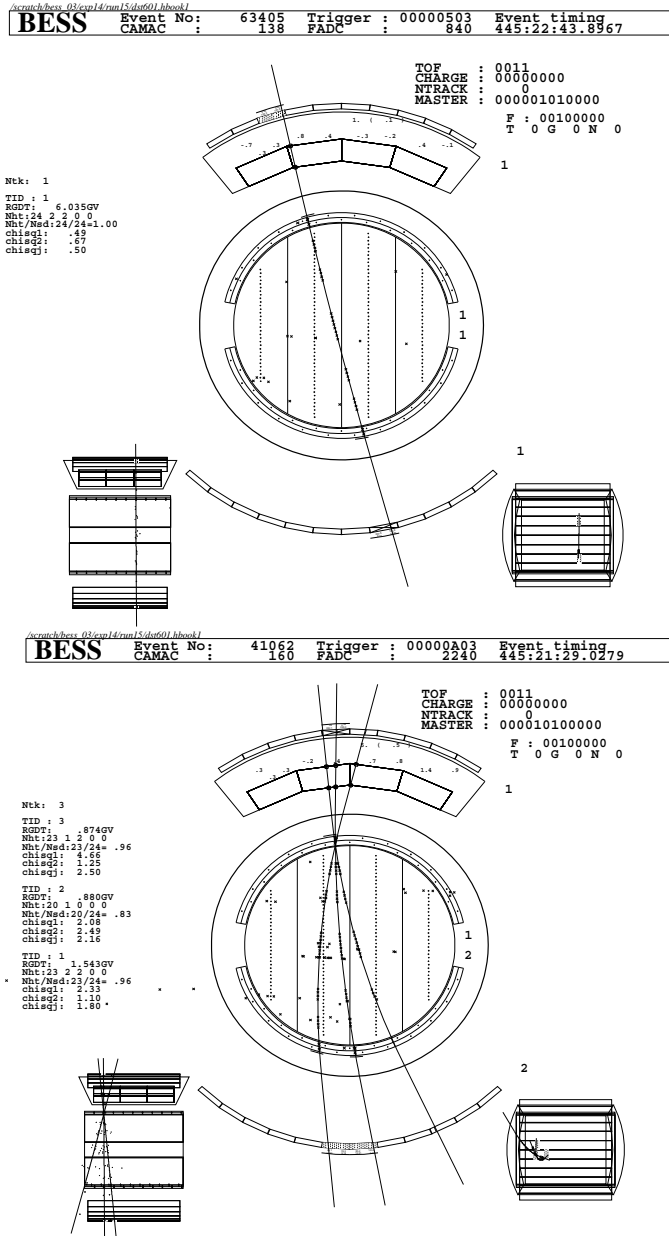


Figure 2.2: A typical helium event (top) and an event with interaction (bottom).

2.2 Superconducting Solenoidal Magnet

The superconducting solenoid magnet is the central core component of the magnetic rigidity spectrometer. The magnet was specially designed to provide uniform magnetic field in a large solid-angle acceptance with minimizing incoming particle interaction with the magnet wall material[9, 15].

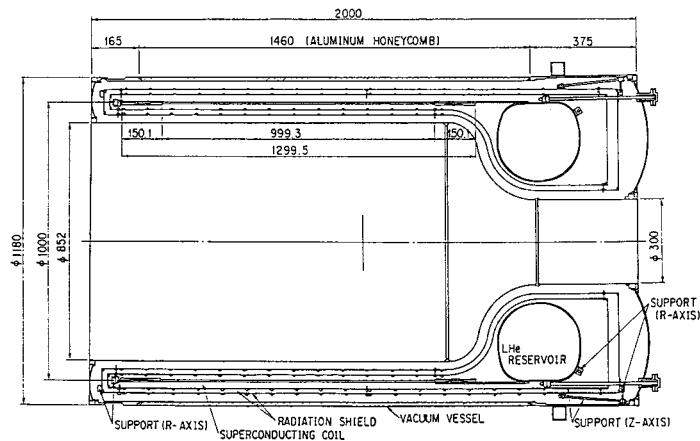


Figure 2.3: Cross section of the superconducting solenoid.

The superconducting coil was wound with aluminum-stabilized NbTi/Cu superconductor in four layers in the central area and in eight layers in both axial ends for better field uniformity. Figure 2.3 shows the cross section of the solenoid. A central magnetic field of 1.2 tesla was generated with a field of uniformity of 12 % in the central trackers (JET/IDC) with a wall transparency of 0.2 radiation length.[16]

The coil was indirectly cooled by thermal conduction through pure-aluminum strips and the outer support cylinder linked to a liquid helium reservoir located in one end of the solenoid coil. This configuration realized advantages of the minimum wall material in the detector acceptance and also an intrinsic safety protection against a magnet quench with suppressing sudden pressure rising in the reservoir.

The solenoid coil was successfully tested up to a central magnetic field of 1.2 tesla and was operated at 1 tesla in the scientific balloon flights[17]. Major parameters of the solenoid magnet are summarized in Table 2.2, and

the flux line and the field strength contour are shown in Figure 2.4.

Table 2.2: Main parameters of the superconducting solenoidal magnet (MAG).

Dimensions		
Coil diameter	1.0 m	
length	1.3 m	
coil thickness (center)	5.2 mm	
(end notch)	10.4 mm	
Cryostat diameter	1.18 m	
length	2.0 m	
Useful aperture diameter	0.85 m	
length	1.0 m	
Central field	1.0 T	(1.2 T*)
Current	430 A	(520 A*)
Stored energy	815 kJ	
Wall thickness	0.22 X_0 per wall	
	4.7 g/cm ² per wall	
Total weight	430 kg	
Conductor	Nb/Ti/Cu	
Stabilizer	Pure Al(99.999%)	

*Tested

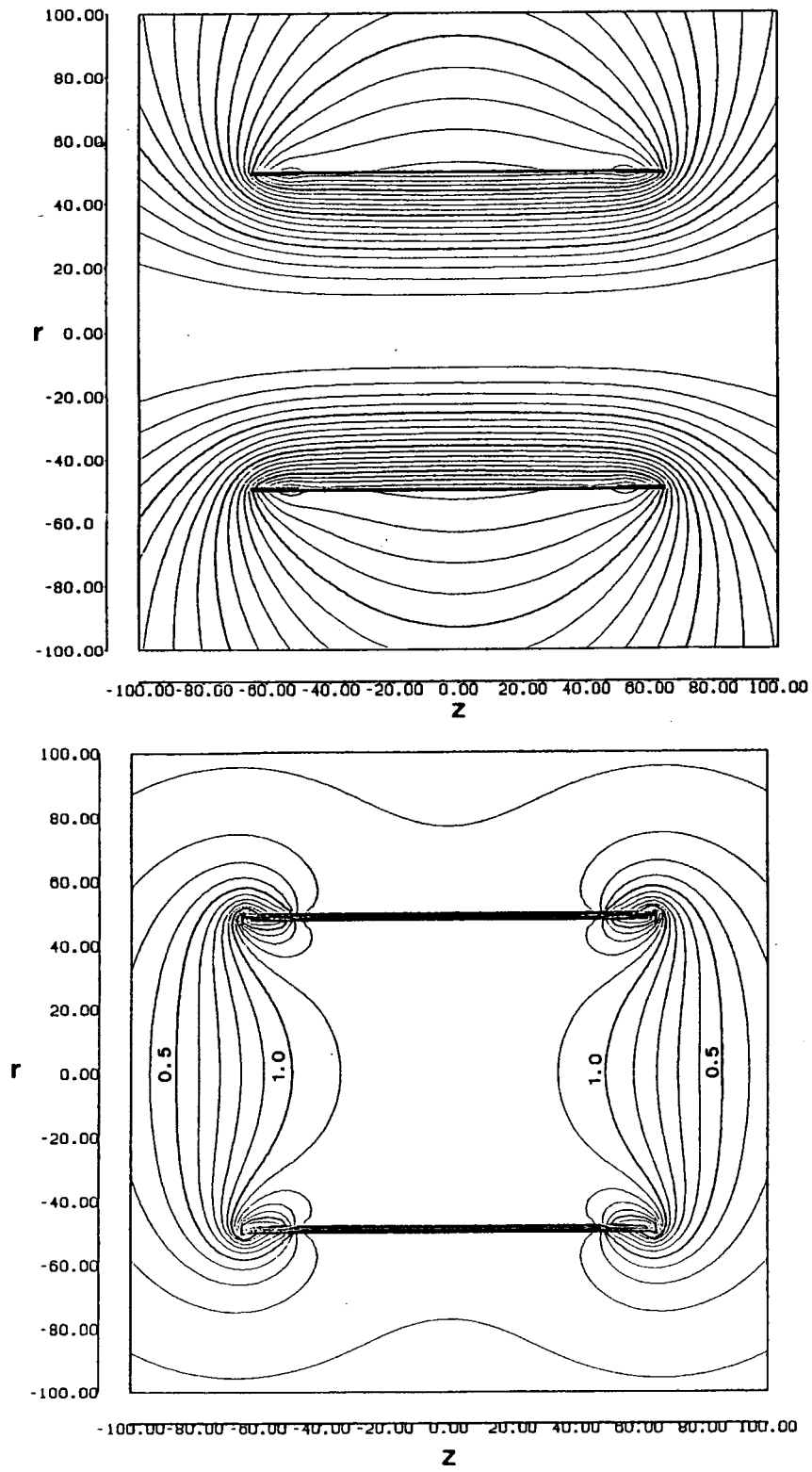


Figure 2.4: Flux line (top) and field strength contour (bottom) of the superconducting solenoid.

2.3 Tracking

2.3.1 JET Chamber

The JET chamber was located inside the warm bore (0.85 m in diameter and 1.34 m in length) of the solenoidal magnet, providing a particle trajectory in r - φ plane by drift time measurement and in z direction by charge division read-out.

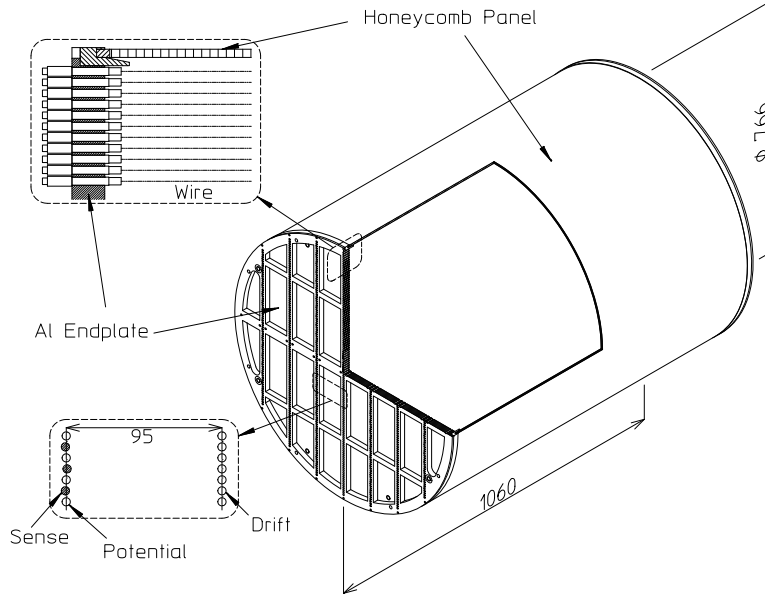


Figure 2.5: Schematic view of the JET chamber.

A schematic view of the JET is shown in Figure 2.5, and its parameters are summarized in Table 2.3. The sensitive volume of the JET is a cylinder of 1 m in length and 754 mm in diameter. The chamber is subdivided into four sections in vertical by cathode planes in which gold-plated aluminum wires of 200 μm in diameter are stretched at 6.7 mm interval. At the center of each section, there is a signal wire plane in which sense wires (gold-plated tungsten-rhenium alloy, 20 μm in diameter) are equally spaced at 13.4 mm intervals alternated with potential wires (gold-plated aluminum, 200 μm in diameter). Each of the two central (side) sections contains 52 (32) sense wires. In order to resolve left-right ambiguity, the sense wires are staggered by $\pm 500 \mu\text{m}$ from the center plane defined by the potential wires. The

maximum drift distance of one section is 95 mm.

The high voltages of the potential and cathode wires are -2.85 kV and -10.80 kV, respectively. The sense wires are kept at ground level. The electric field strength in the drift region is about 0.85 kV/cm, which corresponds to the maximum drift time of 12.3 μ s using a gas mixture described below.

Every wire is positioned and fixed by a feed-throughs, which is stuck in a hole drilled through the end plate. The feed-through has a Derlin bush for positioning, a brass lead for soldering and a Derlin sleeve for electrical insulation. The inner diameter of the bush is 270 μ m for potential/cathode wires and 80 μ m for sense wires enabling us to achieve a positioning precision better than 50 μ m. The wire tensions are adjusted to be half their elastic limits to allow for deformation of the chamber due to temperature variation and acceleration impact.

In order to reduce weight and material, the wall of the cylinder was constructed with a honeycomb plate. It was made of 6 mm thick Aramid core with skins of 125 μ m thick copper plated Kapton sheets. The field shaping strips with various widths depending on the azimuth were etched on the inner surface of the cylinder. Resistors connect the neighboring strips with proper resistance to form a uniform drift field.

The end plates were made of 20 mm thick aluminum, rigid enough to support a total wire tension of 1.53 kN. From the weight consideration, many pits of 15 mm depth were scooped out in the end plates. The pits are used to house preamplifier boards. Inside the end plates, G10 boards with copper-etched field shaping patterns were glued to complete the field cage.

The total weight of the JET chamber is about 80 kg. The average material passed by a penetrating particle is 0.48 g/cm² including two chamber walls and wires.

2.3.2 Inner Drift Chamber

The IDCs, located just inside the cryostat, provide track hit positions in the z -direction with high precision through diamond-shaped vernier strip readout as well as in the azimuthal direction through drift time measurement. Their cell structure in the azimuthal direction is also used by the track trigger for track-pattern recognition making a quick determination of the angular deflection and the sign of charge of incident particles.

The IDCs are arc-shaped drift chambers with identical double layer structure except for their dimensions. A schematic view of them is shown in Figure 2.6 and main parameters are summarized in Table 2.3.

Each chamber is composed of four Aramid-core honeycomb panels with

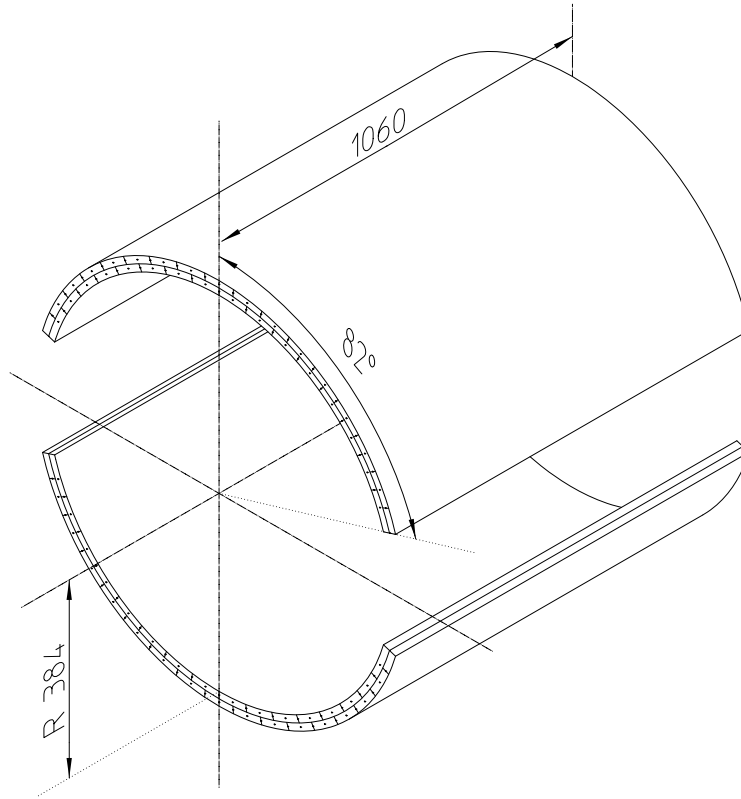


Figure 2.6: Schematic view of IDC. The cross sections shows in a circle.

G10-plastic end and side plates. The skins of the honeycomb panels, copper-plated Kapton sheets, electrically isolate the two layers. The sensitive volume of each layer is 12 mm thick and is divided into cells by alternately stretched sense and potential wires. The wires are fixed by the same feed-throughs as used in the JET at an interval of 6.50° (4.47°) in azimuth for the IDC, corresponding to a half-cell size of about 50 mm. The wire position in one layer is shifted by a half-cell pitch with respect to the other layer. By adopting this double layer configuration, the left-right ambiguity can be automatically resolved and quick hit cell information is available by making a coincidence of the two overlapping cells.

Field shaping strips of 1.5 mm in width are etched on the inner surface of the copper-plated Kapton sheet at a 3 mm interval. The strip pattern on opposite side of the IDC layer is slightly shifted so that the direction of the

electric field is tilted by 5.5° with respect to the drift (azimuthal) direction in order to compensate for the Lorentz angle arising from the magnetic field of 1 Tesla.

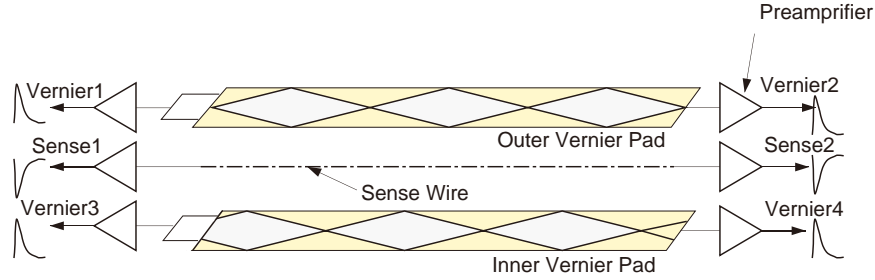


Figure 2.7: Read-out scheme for IDC signals.

Vernier-cathode-strip pairs of 7.5 mm width are etched on both sides of the sense wires. As shown in Figure 2.7, each pair consists of a diamond-shaped inner strip and an outer strip with complementary shape. A cycle length of the pattern is 100 mm for the IDC. The strip patterns on opposite sides are shifted by a quarter pitch along the z -direction to give a precise hit coordinate. There are four strips in total associated to a single sense wire, which are read out separately.

In order to set a potential of vernier strips at ground level, the high voltage applied to the sense wires is +2.70 kV and the high voltage to the potential wires is -4.00 kV for the IDC. The average electric field in the drift region is 0.8 kV/cm.

Since the chamber structure is fragile against over-/under-pressure, a 0.5 mm thick aluminum plate is glued to the outer surface of the chamber for mechanical reinforcement.

2.3.3 Chamber Gas

The JET and the IDCs are filled with the same gas mixture of CO_2 90 % and Ar 10 %, called “slow gas”. The drift velocity at 1 atm and with an electric field of 1 kV/cm is about $8.1 \text{ mm}/\mu\text{s}$. Owing to its slow drift velocity and small longitudinal diffusion of drift electrons, good spatial resolution and good double-track separation can be achieved by using reasonably low power and moderate speed readout electronics, at the expense of delicate control of high voltages and pressure of the gas.

The pressure vessel is also filled with the same chamber gas. Thus any chamber suffering a small leak would still be operational during flight. The valves at the inputs and the outputs of the chambers are closed just before launching and the chambers are operated without gas circulation and supplies during a one-day flight.

2.3.4 High Voltages

High voltage power supplies are compact DC-DC converter modules. The high voltages are applied to the chambers through low-pass filters. The output voltage is adjusted by an external resistor and is switched on/off by a command issued from the ground station. The ramping profile of the output voltage is internally controlled so that it takes five minutes before reaching the nominal value. The output voltage and current are monitored by the monitor system. A small iron cylinder inside the module shields magnetic components.

2.3.5 Readout Electronics

Preamplifiers

The signals from the sense wires of all the chambers and the vernier strips of the IDCs are fed to the same type of preamplifiers (Fujitsu MB43458), which can cope with both polarities, negative signals from the wires and positive signals from strips. The preamplifier chip is a monolithic IC with four equivalent amplifier circuits with a gain of $7 \text{ mV}/\mu\text{A}$ and 96Ω input impedance[19]. Typical pulse height of the preamplifier output is 10 mV while the noise level remains below 0.2 mV.

The preamplifier boards for the JET have four or three amplifier chips (16 or 12 channels/board). They are individually buried in the pit of the aluminum end plates covered with aluminum plates for noise shielding. Because of the high power consumption of the digitizing electronics, all the wires of the JET could NOT be read out. The number of channels was compromised considering a required momentum resolution and the total power consumption. In each of the two central (side) sections, 24 (16) sense wires out of 52 (32) are read out. The signals of sense wires are read at both ends for charge division. Up to 24 points in r - φ and in z are sampled for an incident charged particle penetrating the central region of the JET.

The preamplifier boards for the IDCs have a single chip. They are attached to the end plates of the chambers and are housed in a copper shield

cage. The IDCs are read out from a single end of each sense wire and four strips.

FADC

The output of preamplifiers of the JET wires and the IDC vernier strips were fed to flash analog-to-digital converter (FADC) modules. The FADC module has 16 input channels. 21 modules (336 channels in total) were housed in two EUROCARD industry standard crates. The 160 channels were used for JET chamber readout and the remaining 176 channels for IDC vernier strips.

The FADC system was newly developed to meet the requirements of this experiment, low power consumption and fast data compression[20]. The input signal of the FADC module is further amplified by a main-amplifier with a gain of 10 (40) for the JET (IDC). It is digitized by a FADC (HITACHI HA19211BMP) with 8-bit resolution at a rate of 28.5 Msps for a duration of 18 μ s (512 samples in total). A digital comparator then compares the digitized data with a preset value and only data above the threshold are written in a FIFO memory. This zero suppression process is executed synchronously with the digitization on each FADC channel without costing any extra time. Then a data compressor module in the FADC crate further compresses a sequence of the non-zero data train into a small number of useful information; the channel number, the total charge of the pulse, the timing of the signal arrival, the pulse width and the first two raw data of the pulse. Thus the data volume was reduced by a factor of 3 in average. For a typical single track event, the data compression process took less than 200 μ s.

Amplifier/Discriminator

The sense wire signals from the IDCs are further amplified and discriminated by amplifier/discriminator (A/D) modules. The discriminated sense wire signals from the A/D modules are used to issue a second level trigger. A detailed discussion on the trigger process is made in Section ??.

2.3.6 Performance of Tracking System

The transverse and total rigidity of a particle is determined by fitting the three-dimensional hit positions measured by the drift chambers. Energy loss in the chamber gas is also measured using the charge information of the JET. To obtain hit positions in r - φ plane, the drift velocity was calibrated using the flight data. Although the drift length is approximately proportional to

the drift time, some nonlinear effects exist due to distortion of the electric field. This non-linearity was corrected by fitting the $x-t$ relation with a third-order polynomial function.

Rigidity Measurement

The JET and the IDCs determine the rigidity of a track. First, good hits, defined as hits with enough charge and pulse width, are selected. They are connected to form a candidate trajectory. The transverse rigidity, R_T , is then calculated by applying a circular fitting to those hits associated to the track. This procedure is iterated adding new hits close to the track and dropping deviant hits. The resultant R_T is then corrected for the non-uniformity of the magnetic field. From a Monte Carlo simulation for various trajectories in the exactly calculated magnetic field, correction factors to the rigidities were derived as a function of track position, inclination, and rigidity. The correction factors reproduce the original rigidities within a typical accuracy of $\pm 0.2\%$ for tracks within a fiducial volume, the central sections plus the inner half of the side sections of the JET.

To determine the total rigidity, R , we obtain a dip angle, θ_{dip} , which is defined as an angle between the total rigidity vector and $r-\varphi$ plane. A sinusoidal fitting in $r-z$ plane is applied to the selected hits in the JET and the IDCs iteratively, as in the $r-\varphi$ fitting, to eliminate irrelevant hits. All possible combinations of IDC hits are examined, since the IDCs provide only the z -positions within a vernier strip pattern cycle of 100 mm. The resultant θ_{dip} is the one obtained from the combination which gives the minimum χ^2 value. The total rigidity R are derived from R_T and θ_{dip} as $R = R_T / \cos \theta_{\text{dip}}$.

Based on the residual distributions shown in Figure 2.8, the overall spatial resolutions of the JET and the IDCs in $r-\varphi$ plane are respectively estimated to be $175\ \mu\text{m}$ and $220\ \mu\text{m}$. Figure 2.9 shows drift length dependence of the spatial resolution. This position resolution in $r-\varphi$ plane of the tracking system enables transverse momentum measurement with a resolution of $\Delta p_T / p_T = 0.5 p_T (\text{GeV}/c)\%$, giving the maximum detectable rigidity (MDR) of $200\ \text{GV}/c$.

z -position Measurement

The z -coordinate of a hit position is obtained by using the charge division of the JET, and the vernier strip readout for the IDCs.

First we roughly determine hit positions along the sense wires of the JET by the charge division method. The z -coordinate of a hit position is

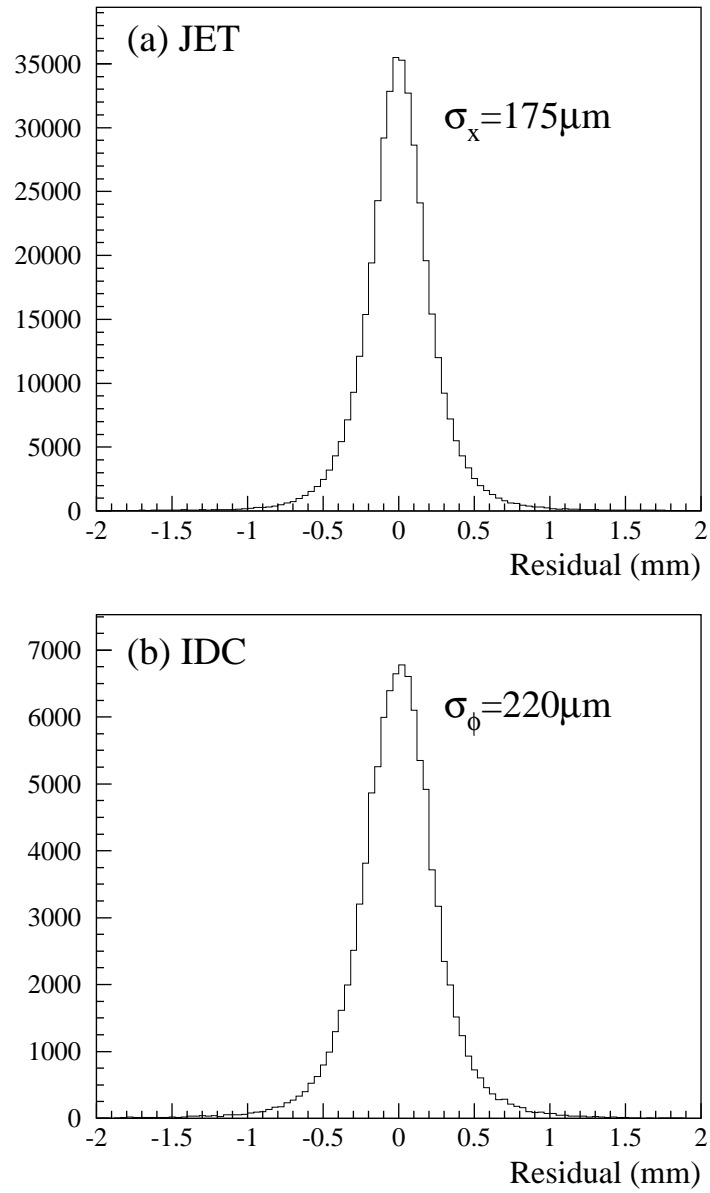


Figure 2.8: Fitting residuals for (a)JET and for (b)IDC in r - φ plane.

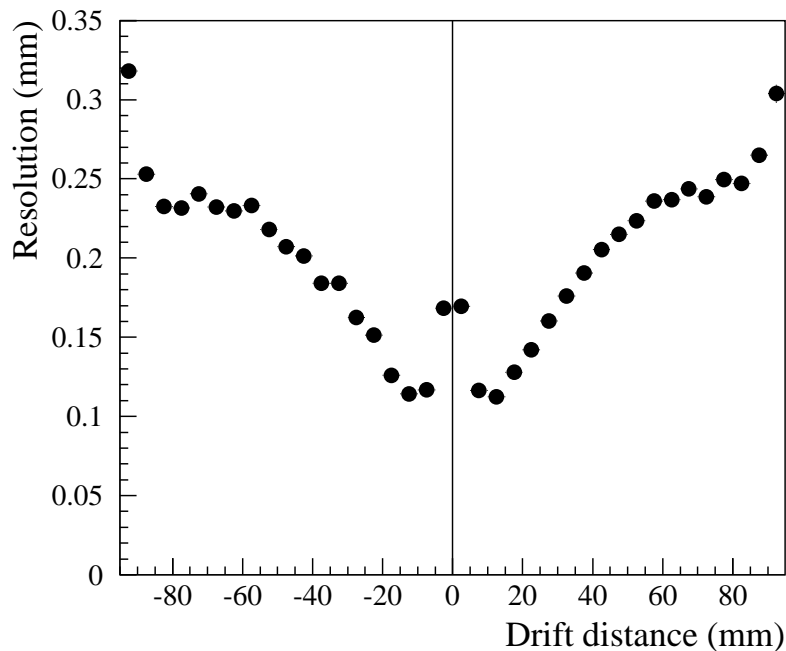


Figure 2.9: JET chamber r - ϕ resolution as a function of the drift distance.

derived from the charges read out at both ends of the hit wire (Q_a and Q_b). Hit position (z) is given by

$$\frac{z}{L} = \frac{(R+r)Q_b - rQ_a}{R(Q_a + Q_b)}$$

where L and R are the length and the resistivity of the sense wire and r is the input impedance of the preamplifier. We obtained the z -position resolutions of 20.3 mm for single-charged particles (Figure 2.10), by the JET, which are precise enough to identify the particular vernier strip cycle of the IDCs hit by a track.

After the coarse determination of the z -coordinate, we use the vernier strips of the IDCs to get the z -coordinate precisely. The hit position along the z -axis is measured using the signal charges induced on the associated vernier-strip pairs. We define a normalized charge ratio, ε , for a pair of vernier-strips, A and B.

$$\varepsilon_{I(O)} = \frac{Q_{AI(O)} - Q_{BI(O)}}{Q_{AI(O)} + Q_{BI(O)}}$$

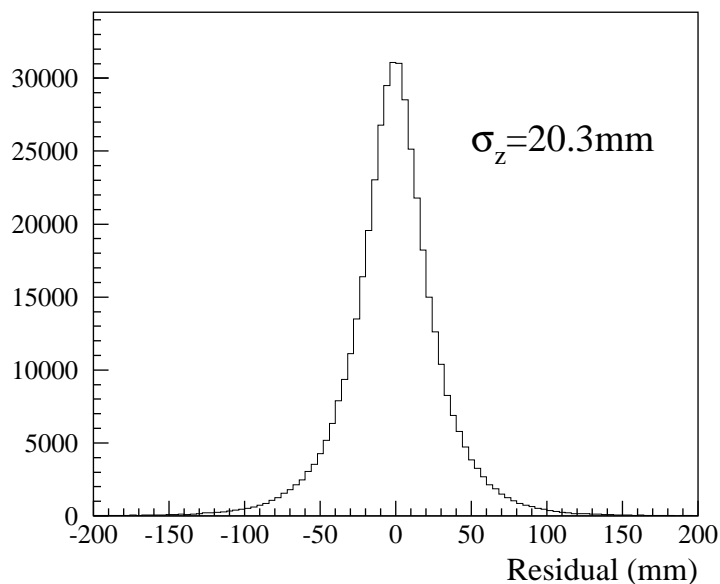


Figure 2.10: Residual distribution of the JET chamber along the z -coordinate.

where $Q_{AI(O)}$, $Q_{BI(O)}$ denote the charges induced on A and B of the inner vernier-pad pair (outer vernier-pad pair). The ε parameters are linearly related to the z -axis position of the avalanche point. Figure 2.11 shows a scatter plot of ε_1 vs. ε_0 for the IDC vernier strips. A line in the figure shows numerically calculated values for various z -positions. A circuit along the round-square locus corresponds to a vernier-strip pattern cycle of 100 mm (120 mm) along the z -axis. We can derive the z -coordinate of a hit position by comparing a measured ε pair with the numerically calculated values. The deviations of the measured ε values from the calculated line are translated to the z -position resolution, giving the resolution of $470 \mu\text{m}$ by the IDC vernier strips as shown in Figure 2.12. The performance of the tracking system is summarized in Table 2.3.

Energy Loss Measurement

The pulse height measurement of the JET provides independent and redundant information as to particle identification. However, it was found that the dE/dx resolution of the JET deteriorates, particularly in the higher sig-

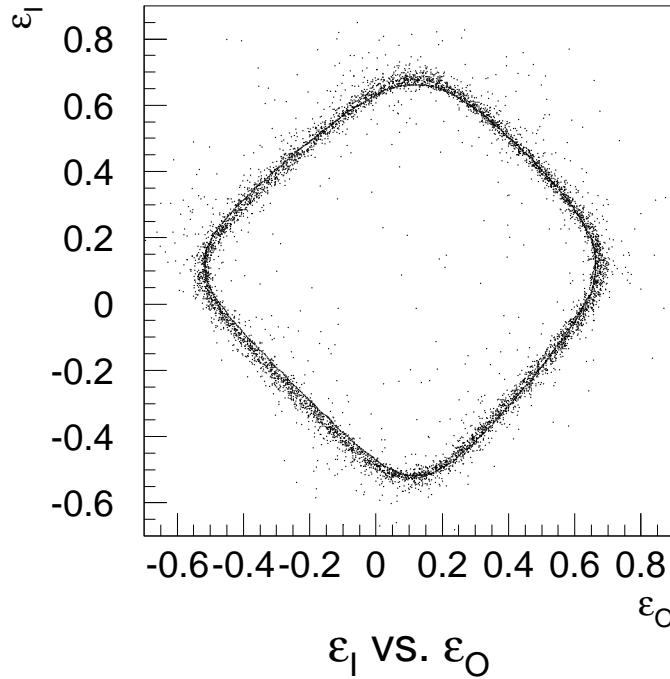


Figure 2.11: Scatter plot of the ε parameter of the inner (ε_I) and outer (ε_O) pad.

nal charge region, due to the space charge effect. After a detailed study of the effect, a correction method for saturation was obtained as follows.

The saturation strongly depends on the inclination angle θ_{y-z} between the track and the z -direction, and also slightly depends on the inclination angle $\theta_{r-\varphi}$ of the track in the r - φ plane. Using pure helium and proton samples, the energy deposit is derived from the two-dimensional function of the θ_{y-z} and the measured charge, and then corrected for the $\theta_{r-\varphi}$ dependence.

The correction for the drift length is then applied to obtain the energy loss \bar{E} . In order to remove the Landau tail and delta ray effects, a truncated mean method is adopted. The points in lower 10 % and higher 50 % are eliminated, and the mean dE/dx is calculated using the rest of the hit points.

Figure 2.13 shows the dE/dx measured by the JET for an unbiased data sample. We can clearly distinguish clusters of protons, muons/pions/electrons,

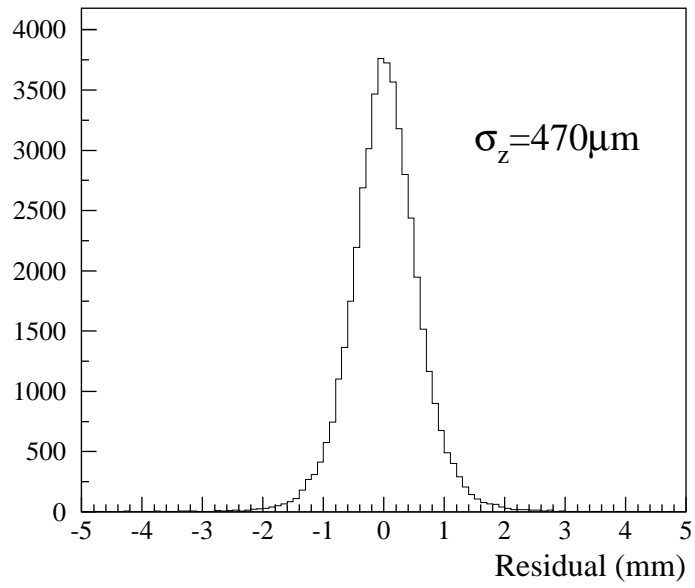


Figure 2.12: Residual distribution of the IDC along the z -coordinate.

deuterons, and heliums. The truncated mean method effectively removes the higher tail of the dE/dx distribution.

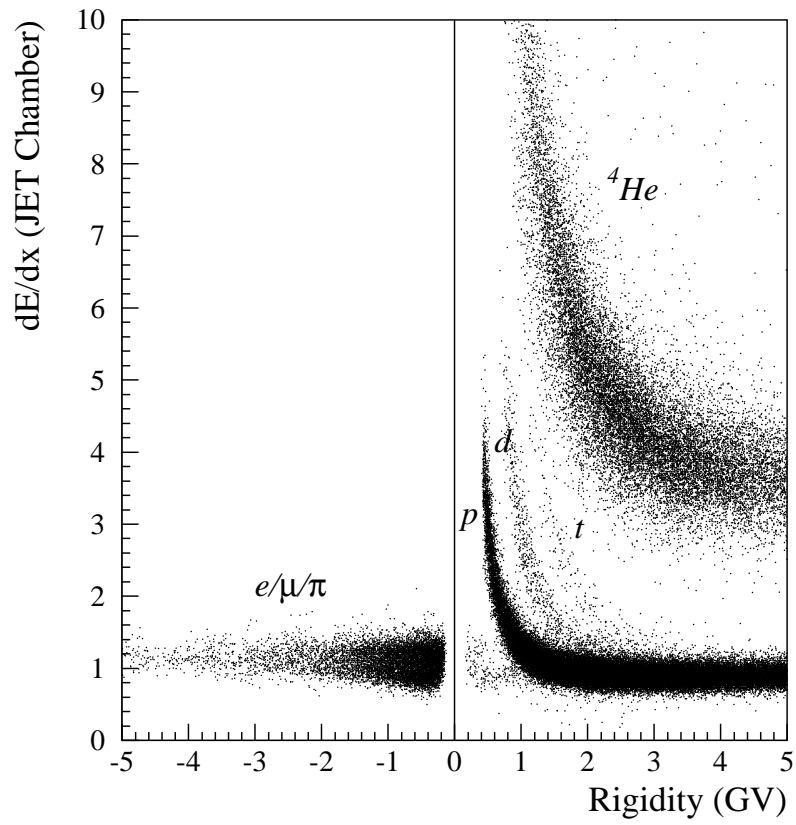
Figure 2.13: dE/dx measurement by JET.

Table 2.3: Parameters of tracking chambers.

JET	
Shape and Size	Cylindrical, 766 mm ϕ \times 1060 mm
Sense wires	W/Re(Au plated), 20 μ m ϕ , 176 wires
Tension	0.392 N
Wire spacing	13.4 mm (y), Staggering of ± 500 μ m (x)
Potential wires	Al(Au plated), 200 μ m ϕ , 196 wires
Tension	2.94 N
Wire spacing	13.4 mm
Cathode wires	Al(Au plated), 200 μ m ϕ , 301 wires
Tension	2.94 M
Wire spacing	6.7 mm
Maximum drift length	95 mm
Spatial resolution	175 μ m (x), 2.0 cm (z)
Maximum Detectable Rigidity	200 GV/ c
IDC	
Shape and Size	Arc-shaped, $R = 384\text{--}420$ mm, $ \varphi < 82.0^\circ$, $L = 1060$ mm
Sense wires	W/Re(Au plated), 20 μ m ϕ , 11(inner)/12(outer) wires
Tension	0.392 N
Wire spacing	13.0 $^\circ$
Potential wires	Al(Au plated), 200 μ m ϕ
Tension	3.43 N
Spatial resolution	220 μ m (φ), 470 μ m (z)

2.4 Time Of Flight Hodoscope

2.4.1 TOF Hodoscopes

The TOF hodoscopes were cylindrically located at a radius of 800 mm at the top and 760 mm at the bottom of the spectrometer (Fig.2.1). The upper (lower) hodoscope consisted of eight (twelve) counters. Each counter (Fig. 2.14) was composed of plastic scintillator (Bicron BC404) with a dimension of 950 mm (length) \times 100 mm (width) \times 20 mm (thickness), viewed by a 2.5-inch photomultiplier tube (Hamamatsu R6504S) at each end through a fishtail-shaped UV-transparent acrylic light guide. BC404 was chosen for its good characteristics such as a short rise time (0.7 ns) and a high light output (68 % Anthracene). The photomultiplier (PMT), which was developed for the use in a strong magnetic field, has 19-stage fine-mesh dynodes and provides a high gain (4×10^6) and a fast rise time (2.5 ns).

We utilized GUIDE7[21] optical simulation package to obtain the best timing resolution by optimizing the shape of the counter within the spatial and positioning restrictions of the counter and of the PMT. Since the gain of the PMT does not depend only on the magnitude of the magnetic field but also on the angle between the PMT's axis and the field direction, special care was taken to the position of the PMT. The strength of the fringe magnetic field is about 0.2 Tesla around the PMT and the inclination angle should be

Table 2.4: Parameters of TOF counters.

	BESS – 97 & 98
No. of upper counters	10
No. of lower counters	12
Dimensions	95 cm \times 10 cm \times 2 cm
Position of upper counters (radius)	800 mm
Position of lower counters (radius)	760 mm
Scintillator	BC404
Light guide shape	Fish-tail
Conversion gain of TDC	25 ps

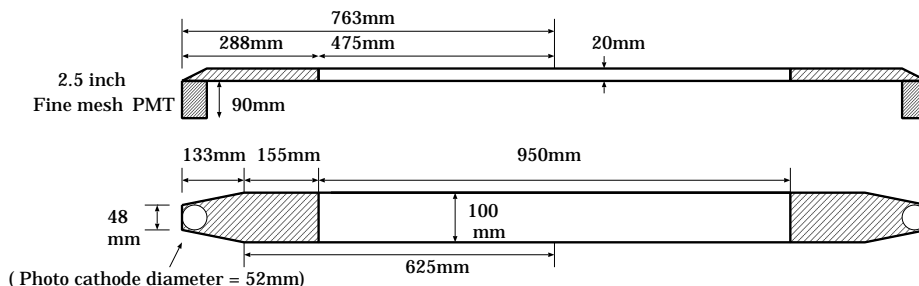


Figure 2.14: TOF counter module in BESS-97 and 98 detector.

less than ~ 20 degrees from the magnetic properties of the PMT which we had studied. The performance tests of a few prototype counters were made using test-beams at KEK, and the optimum design was fixed with a timing resolution of 80 ps. Each PMT was attached to the surface of the light guide perpendicularly with the inclination angle of about 15 degrees, minimizing the performance degeneration.

The light guides were glued to the scintillators with transparent epoxy-resin adhesive. The connection between PMT and light guide was made optically with a silicon rubber (1 mm thick disk) with optical grease on its both sides. Both the silicon rubber and grease were carefully chosen with considering light transmission efficiency, reflection index and mechanical flexibility. The PMTs were fixed with springs of stainless steel to the aluminum mounting bracket attached the light guide. The whole counters have mechanical strength strong enough to withstand the gravitational acceleration during experiments and transportation.

Each scintillator was wrapped in a white sheet (Millipore IPVH00010) for diffusive reflection of light. The light guide was wrapped in a thin aluminized Mylar, except its end part near PMT in silver-vapored Mylar, to minimize light losses. Two layers of black vinyl sheet wrapped the overall counter for light shield.

The bleeder circuit in the PMT was designed to give good timing resolution and also to provide 18th and 19th dynode signals in addition to the anode signal. Various high voltages between -1.7 kV and -2.1 kV were applied to adjust the gains of all PMTs to the same value. Due to sufficient electric current in the bleeder, the gain is stable against a high rate during the flight. Each high voltage power supply contains a DC-DC converter and a distributor which applies high voltages to four PMTs. Since they were also located in the strong magnetic field, step-up transformers were shielded

by iron shield boxes.

2.4.2 Electronics and Signal Processing

The output signals from the counters were used for three different purposes; timing measurement, charge measurement and first-level trigger generation. To avoid the *interference in the electronics* with each other, three signals extracted from the anode, 18th and 19th dynodes were utilized for the above purposes, respectively.

The anode signals were used to issue STOP pulses for timing measurements, because they have the highest pulses suitable for the discrimination. The leading-edge type discriminator was implemented in a 16 channel single-width CAMAC module developed for this experiment, being composed of ECL comparators and differential drivers for output STOP pulses. Threshold levels were set to 15 mV, that are about 1/60 compared to the anode pulse-heights of minimum ionizing particles (MIPs). Pulses from the discriminators are fed into CAMAC TDC module [22], which has a 12 bit resolution with the conversion gain of 25 ps/count. Data of STOP channels are only written in the event-data.

Every 18th dynode signal is distributed, after converted its polarity by a pulse-transformer (with a low permeability material core) and delayed by a air-core delay-line, to the CAMAC ADC module [23] for charge measurement during a common gate of 250 ns.

The 19th dynode signals were used to generate the first-level trigger, from which START pulse was issued for digitization. Concerning the trigger process, details are discussed in Section 2.6.1.

2.4.3 Performance of TOF System

Using the full BESS'97 configuration, counter performance was evaluated with cosmic-ray data collected at ground-level at KEK in May 1997.

TOF data were analyzed with incident angle correction of the ADC counts using scintillator path length, time-walk correction, and correction of timing z -dependence using $dif(z)$. Figure 2.15 shows muon (μ) bands after the cuts of dE/dx , track quality, and $1/\beta < 1.2$, where μ sample area is indicated. Based on the selected sample, the timing resolution was determined by calculating the ΔT , which is the difference between the TOF obtained from the data of TOF PMTs, T_{tof} , and the TOF expected from the tracking information, T_{trk} , i.e.,

$$\Delta T = T_{tof} - T_{trk} \quad (2.1)$$

$$T_{trk} = \frac{L}{c} \beta_{trk}(R, m) = \frac{L}{c} \frac{p}{E} = \frac{L}{c} \sqrt{(ZR)^2 / ((ZR)^2 + m^2)} \quad (2.2)$$

where L is the path length of the incident particles from upper to lower layer, Z the electric charge of the incident particles, R the rigidity of the incident particles, and c the velocity of light. Due to the error in R being small, the error in T_{trk} (Eq. (2.2)) is also small and the rms of ΔT represents the resolution of the TOF hodoscopes.

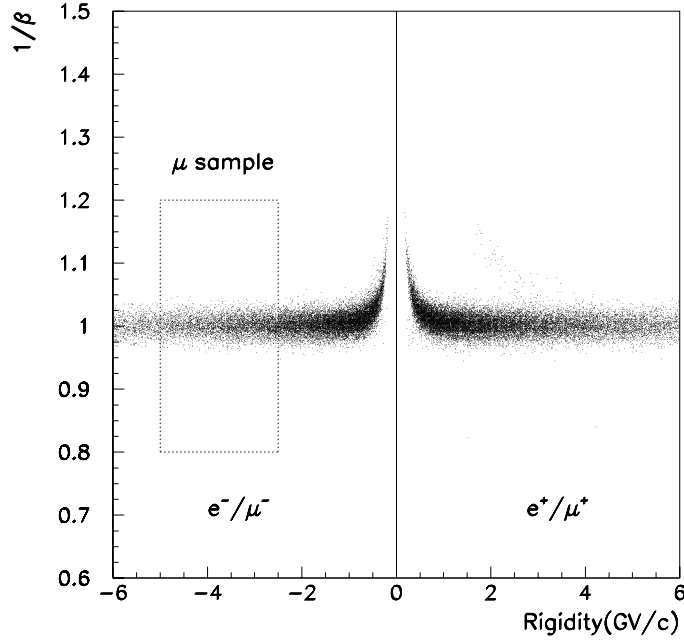


Figure 2.15: Scatter plot of $1/\beta$ vs. rigidity for cosmic-ray data at ground-level using cuts of dE/dx , track quality, and $1/\beta < 1.2$.

Accordingly, a TOF resolution of 71 ps is obtained for TOF hodoscopes in the BESS detector. Figure 2.16 shows the ΔT distribution fitted by pure Gaussian resolution function with no tail. Actually, however, since T_{tof} is the time-of-flight between upper and lower TOF counters, each individual counter has a timing resolution of 50 ps.

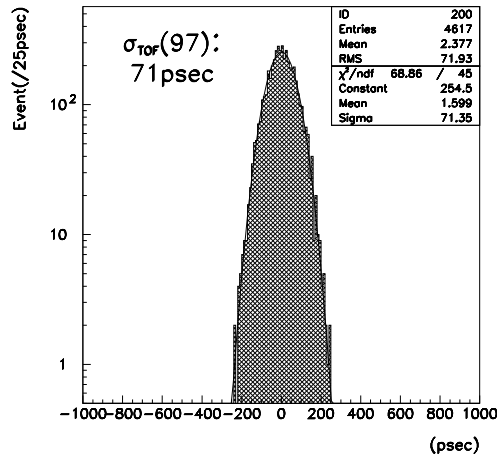


Figure 2.16: The ΔT distribution for BESS data at ground-level.

2.4.4 dE/dx Measurement

For ADC data analysis, we first subtracted its pedestal, and then normalized for the gains of the PMTs and the ADCs and for the efficiency of light collection, using the MIPs vertically traversing the center ($z = 0$) of the counter which yield about 500 photo-electrons at the photo-cathode. Coarse z -position is obtained from the ratio of these normalized ADC values of the both ends' PMTs, and is used for the matching with the extrapolated trajectory.

The dE/dx in a scintillator is calculated, at first, for each PMT by dividing by the traverse length in the scintillator and by correcting for the attenuation of light in the scintillator using the extrapolated trajectory, and we finally adopted the dE/dx by averaging these dE/dx values of both ends. Although the z -position dependence of the attenuation nearly obeys an exponential law and consequently the geometrical average of both ends' ADCs is not expected to depend on the position, the obtained value have slightly position dependence especially near both ends, and the former method produced the better resolution.

Figure 2.17 shows scatter plots of dE/dx versus rigidity measured in the chambers for the top and the bottom scintillators. In the figure are shown proton and helium bands as well as their isotopes, and the energy cut-off

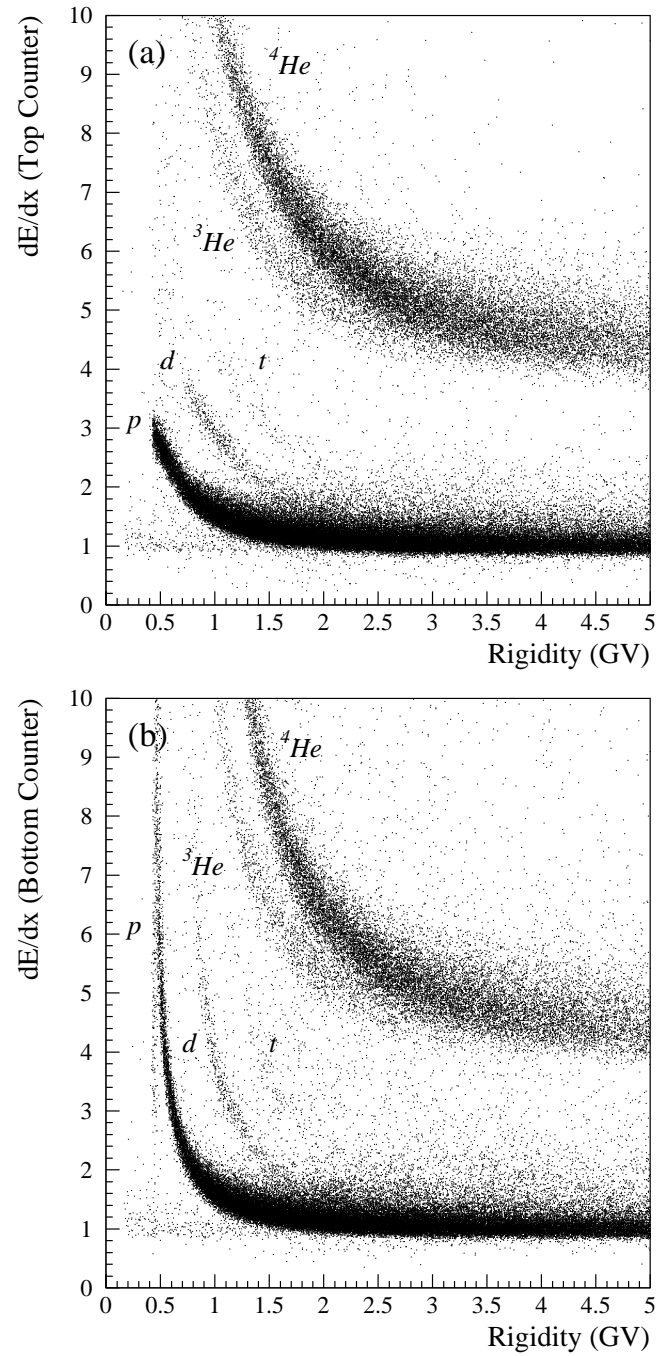


Figure 2.17: Scatter plots of dE/dx versus rigidity for down-going positive-charged particles (a) at the top counters and (b) at the bottom counters.

due to the energy losses between the top and bottom counters. Because the dE/dx distributions have longer tail on the upper side (Landau tail), we evaluated from the lower-side tail that the dE/dx resolution is 6 % for all counters for MIPs in BESS-97 flight data.

2.5 Aerogel Čerenkov Counter

A Čerenkov counter with a silica aerogel radiator (aerogel Čerenkov counter) is installed, in order to detect antiprotons up to 3 GeV by eliminating the overwhelming e^-/μ^- background.

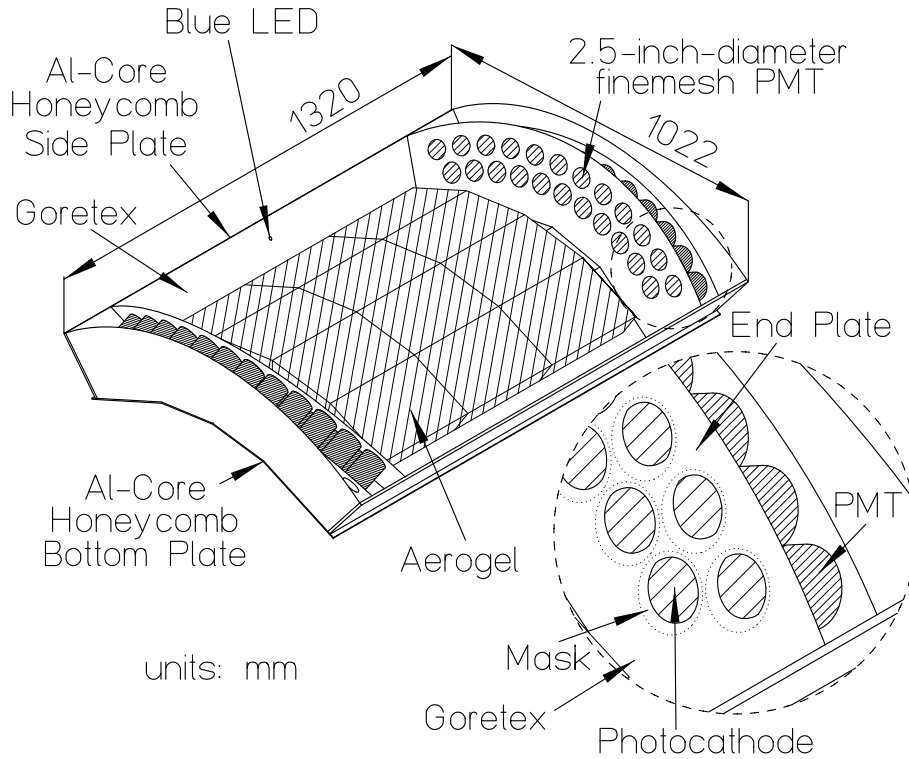


Figure 2.18: Overview of the aerogel Čerenkov counter.

As a Čerenkov radiator, we selected silica aerogel (Mori-Seiyu Co.) having a refractive index of 1.032, which was optically measured in several pieces of sample using a He-Ne laser with wavelength of 632.8 nm [24]. This aerogel was manufactured using a new method [24] which ensures that it retains its hydrophobicity such that long-term stability and good clarity are afforded.

Choosing an effective reflector material is a key aspect in counter design since most photons generated in the diffusion box will undergo numerous reflections prior to reaching the PMTs. We accordingly tested various type of sheet material, *i.e.*, Millipore, Tibex, and Goretex; ultimately finding that Goretex, which exhibits high reflectivity in the short-wavelength region

(300–400 nm), is most suitable. From the standpoint of photon collection, this is consistent with the fact that the number of Čerenkov photons is inversely proportional to the square of wavelength; thereby making reflectivity in the short-wavelength region important.

In consideration of operating the counter in a 0.2-T fringe magnetic field, we selected 2.5-inch-diameter finemesh type PMTs (R6504S, Hamamatsu Photonics K. K.) whose sensitive region lies between 300 and 700 nm. Read-out electronics consists of summing amplifiers that combines 46 PMT signals into 8 channels, which are digitized by a charge-integrated ADC. Blue LEDs (NLPB, NICHIA) with a peak of 450 nm are used to adjust the PMT gain such that all the PMTs provide the same ADC counts per photoelectron. Since PMT gain shows magnetic field dependence, final high-voltage tuning must be done in the counter after exciting the solenoidal magnet to the nominal field. Therefore, the blue LEDs were mounted on the both sides of the side plate at its center point; a configuration allowing PMT gain to be monitored throughout the experiment.

2.6 Data Acquisition System

2.6.1 Trigger

Because of its large geometry factor of the BESS detector, the expected rate of particles penetrating the apparatus exceeds 2 kHz, mostly low energy protons. The typical data size of a single track event is 1 kbytes even after the zero suppression process is applied to the FADC data. If all the events were collected, the data rate would be 2 Mbytes/s and the total data size to be recorded during a 20-hour flight exceeds 100 Gbytes, which is far beyond the on-board storage capacity. An intelligent trigger system has been developed to reduce the overall trigger rate while interesting events should not be lost.

The trigger generation proceeds in three stages. The first-level trigger (T0) is a simple coincidence between the TOF counters and initiates digitization of various FADC/ADC/TDC modules and event building processes. The second level trigger, or the track trigger (TT), is a hard-wired logic which determines the coarse track rigidity (deflection⁻¹) based on the IDC/TOF hit cell information. In order to enrich the recorded data with negative particles such as antiprotons, the majority of the low energy positive tracks were rejected at this trigger level. However, a small portion ($\sim 1/100$) of the events bypassed the TT and were recorded irrespective of their track rigidity. This event sample forms an unbiased data set and is used to study most abundant protons and helium nuclei and to evaluate various efficiencies and correction factors in the off-line analysis. The third level trigger (on-line filter/selection) performed by the microprocessor cluster will be described in detail in the section 2.6.3.

Level-1 Trigger

The T0 was provided by a coincidence between the top and the bottom layers of the TOF counters. A pair of 19th dynode output pulses from PMTs at the both end of each TOF counter were integrated with a time constant of 20 ns and were then linearly summed with a simple capacitor/resistor circuit. The integration was to smooth the pulse shape so that the timing of the peaks were equalized irrespective of the hit position.

The summed signal was discriminated with a discriminator developed for this experiment. It was implemented in a single width CAMAC module and had 16 input channels. The power consumption is 6.7 W/module. The design is almost the same as the one used for the TOF measurement, except that it inverts polarization of input signal adjusting to dynode pulse. The

threshold voltage should be low enough to trigger single-charged particles with good efficiency. It was set at $\sim 1/3$ of the pulse height of vertically incident MIPs at the center of the TOF counter. The discriminated signals in each layer (top and bottom) were ORed and then coincided between the top and bottom to generate trigger signal, named ‘Proton trigger’, in T0-trigger module which has been developed to minimize the propagation delay. Furthermore, in order to calibrate the instrument, we generate a trigger signal independent of the signal of TOF counters, named ‘External trigger’, rate about 1.25 Hz, using electric vibrations of a quartz crystal. The ‘logical AND’ of ‘Proton trigger’ and ‘External trigger’ start data digitization processes. (T0 trigger)

In addition, to consider the charge information of incident particle, we generate two more triggers. They are generated the same way of ‘Proton trigger’, but set different threshold levels. One was set at ~ 2.5 times the MIP signals, which is to $Z \geq 2$ particles, and the other was set at ~ 12 times the MIP signals, which is to $Z \geq 4$ particles, respectively, and generated triggers correspondent to each threshold are named ‘Helium trigger’ and ‘High-Charge trigger’ in turn. These two charge dependent triggers and components of the T0 trigger (i.e. ‘Proton trigger’ and ‘External trigger’) constitute ‘T0 trigger bits’, which are used to make ‘unbiased trigger (CD)’ in Master trigger module explain below.

Level 2 Trigger

The TT module performs the hit pattern recognition and the track curvature determination. The basic concept of the TT is illustrated in Figure 2.19 and the block diagram of the circuit is shown in Figure 2.20. The TT module was implemented in a double width CAMAC module. An on-board microcode-programmable sequencer controlled the entire operation of the module as described below.

The TT is enabled on receiving the T0 with a delay of $\sim 5 \mu s$, the maximum drift time of the IDCs. A coincidence between the overlapping pair of cells defines a hit cell in each chamber and TOF counters. The number of hits in each chamber and TOF counter is obtained from a look-up-table and is encoded into a 5-bit integer. A 20-bit *N-hit* pattern expresses the number of hits in the chambers and TOFs .

When the *N-hit* pattern matches with one of the six acceptable patterns, (1,1,1,1) for example, the events are subject to rigidity analysis. The micro-sequencer scans all the hit cells and picks up a combination of four hits in the four chambers. From the location of hit cells, it then retrieves a 6-bit

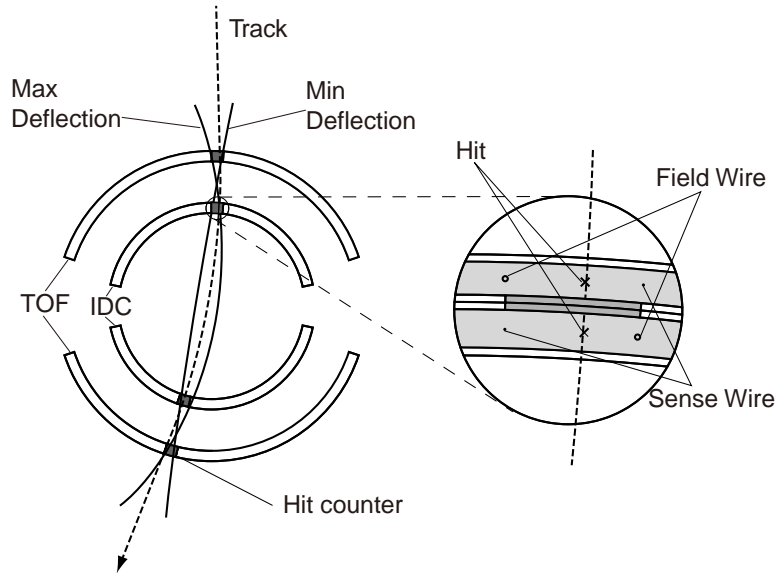


Figure 2.19: Basic concept of the Track Trigger.

deflection from a look-up-table. The minimum and the maximum possible deflection corresponding to each hit pattern was calculated prior to the experiment and their mean value was stored in a 16M-bit EEPROM.

There are six different threshold values prepared for the track rigidity selection. A 6-bit rigidity-selection flag is retrieved by specifying the 6-bit deflection. The above process repeats for all the combinations one after another. The TT can be switched to three hit mode in case of some trouble with one of the chambers. By combining the N -hit pattern and the 6-bit rigidity-selection flag, the final TT trigger bits are set. The N -hit pattern and the rigidity-selection patterns are summarized in Table 2.5.

Since the trigger rate and the dead time depends largely on the rigidity threshold values, they should be carefully tuned by a simulation study before the flight. As shown in Figure 2.21, the trigger efficiencies obtained by the real data and the simulation are in good agreement.

Master Trigger

The T0 trigger bits and the TT trigger bits are combined and the final trigger decision is made in the master trigger (MT) module. The MT module distributes fast clear signals to all the digitizing modules for rejected events.

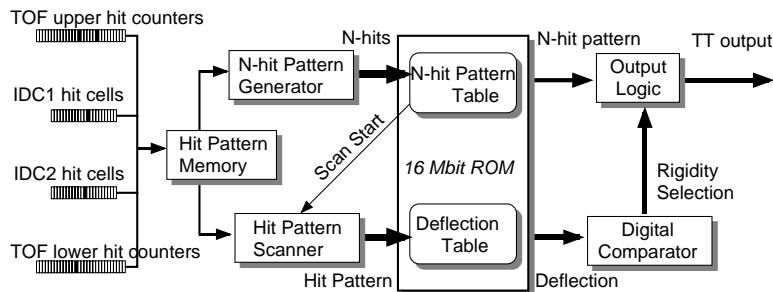


Figure 2.20: Block diagram of TT process.

Table 2.5: Summary of the track trigger selection patterns. $(i, j, k, l)_p$ means the permutation $(N_{iu}, N_{il}, N_{tu}, N_{tl})$ matches (i, j, k, l) , where N_{iu} – the number of hit-cells in upper IDC, N_{il} – the number of hit-cells in lower IDC, N_{tu} – the number of hit-cells in upper TOF and N_{tl} – the number of hit-cells in lower TOF.

Mode	<i>N-hit</i> Pattern	Description	Thres. (GV^{-1})	T0 Mask
0	$(1, 1, 1, 1)_p, (1, 1, 1, 2)_p$	Single negative charged	-0.097	T0-Proton
1	$(1, 1, 1, 3)_p, (1, 1, 2, 2)_p$	Single negative charged with some additional hits	-0.097	T0-Proton
2	$(1, 1, 1, 1)_p, (1, 1, 1, 2)_p$	Multiple negative charged	-0.274	T0-HIGH
3	$(1, 1, 2, 3)_p, (1, 2, 2, 2)_p$ $(1, 2, 2, 3)_p, (1, 1, 3, 3)_p$ $(2, 2, 2, 2)_p$	Multiple negative charged with some additional hits	-0.016	T0-HIGH
4	$(0, 1, 1, 1)_p$	Missing hit in one chamber	0.790	T0-LOW
5	$(1, 1, 1, 1) - (1, 4, 1, 4)$	Multi-track negative	0.790	T0-Proton

The accepted events are subject to the transputer farm for on-line filtering, which is called the third level trigger in the previous section. The CD events are accepted irrespective of the TT trigger bits. The master trigger rate of the 1997 flight was ~ 260 Hz including ~ 60 Hz of unbiased events.

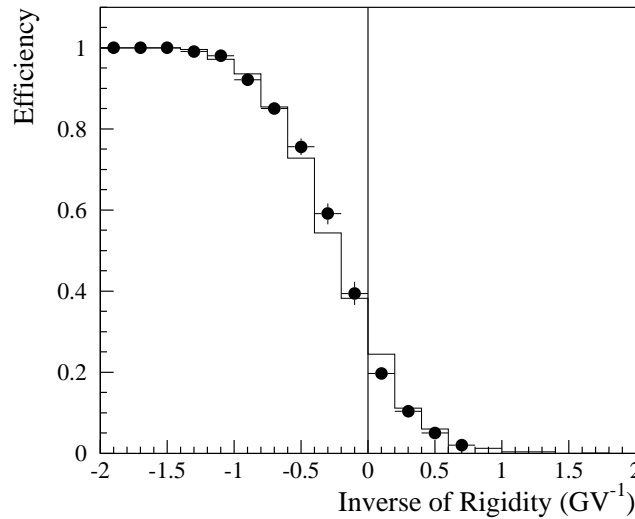


Figure 2.21: Simulated (solid line) and measured (dot) Track Trigger efficiency for the antiproton search.

2.6.2 Event Building

The event-process subsystem was designed to collect digitized data from front-end electronics of sub-detectors and to build formatted data for an event. The subsystem consisted of a subsystem controller (NEC V50), a FADC system, a CAMAC system, an event builder (EVB), and a Transputer farm (Figure 2.22). The digitized data from FADC and CAMAC front-end modules were gathered through FADC and CAMAC Crate Controller's (CC) and processed into "an event-data" by EVB. The event-data was sent to the Transputer farm for further on-line filtering.

In the subsystem, a total of twenty-one Transputers were employed. Each Transputer possesses a processing speed of 20 MIPS and supports execution of parallel tasks. In addition, each Transputer is provided with four serial bus line ports. Two Transputers can be connected with a serial "Transputer link" using these ports and can communicate each other. The Transputer link has a data transfer rate of 20 Mbps[25], but a rate of 1 Mbytes/s has been achieved in our particular application. Each crate controller had a Transputer inside and the Transputer farm contained sixteen Transputers. These were connected with transputer links to construct a "Transputer network". Programs for the Transputer network are written in OCCAM high

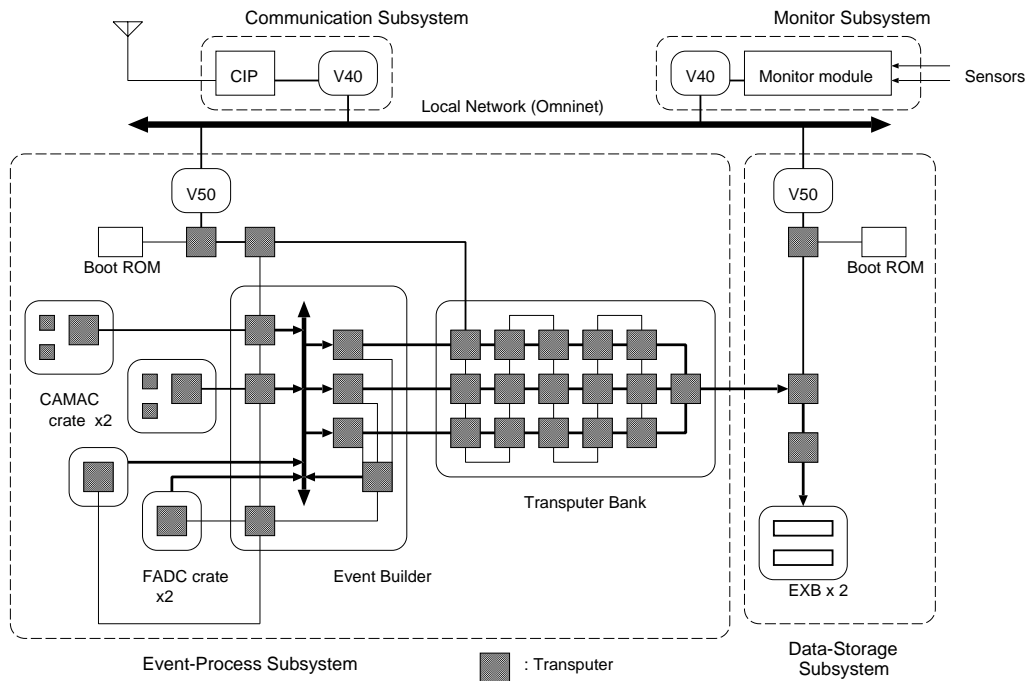


Figure 2.22: Block diagram of the data acquisition system.

level language[26] to utilize Transputer's hardware implementation most effectively.

This unique design enabled high-speed parallel data processing and transferring of the BESS DAQ. Under typical experimental conditions, the subsystem is expected to operate at the event rate of 100 Hz with about 10 % dead time.

2.6.3 Transputer Bank

The main role of the Transputer bank is to select desirable events using the whole detector information: (1) Trigger mode, (2) TOF hits, and (3) rigidity of JET tracks reconstructed using FADC data. We have called this selection the third level trigger in the previous section and have had it since 1997 flight.

For JET track reconstruction and rigidity calculation, the following algorithm is employed:

1. Determine hit position, total amount of charge, and pulse width using FADC data. Since the charge information in FADC data is the sum of pedestal and charge of the hit, the pedestal is subtracted for each hit. The pedestal value of each FADC channel is automatically updated at every 1 hour of the calibration run.
2. Select “good” hits which are defined as hits enough charge and width.
3. Find arrays by connecting the “good” hits in central region of JET chamber, and perform line fitting.
4. Extrapolate each of the line trajectories to find “good” hits near the trajectory, and associate the hits to the array.
5. Perform circular fitting on the array and the associated hits. The circular fitting algorithm is based on non-iterative method by following Karimaki [27].
6. Scan all of “good” hits in JET chamber to check whether they are close enough to the circular trajectory or not. Only the hits passing this check are used in the following process.
7. Perform circular fitting once more and calculate the transversed rigidity in $r\phi$ -plane.

Fifteen Transputers arranged in a 3×5 matrix are dedicated to this job in the Transputer bank. They execute the same program to process events simultaneously. One of the first three Transputers receives the formatted event-data from the EVB through a Transputer link. Then the Transputer processes the event-data, or otherwise if it is already busy, the event-data is relayed down to the following Transputers. Consequently, the Transputer bank can process fifteen events concurrently. If all the Transputers are occupied and busy, the EVB stops sending event-data to the Transputer bank.

Each Transputer executes the above task typically within 20 ms. Therefore, the whole bank including fifteen Transputers is capable of processing events at 1 kHz. The accepted event-data are relayed down and are finally sent to the data-storage subsystem via a Transputer link.

2.6.4 Data Strage

The data-storage subsystem communicates with other subsystems via Omninet, and receives the event-data from the event-process subsystem through a

Transputer link. The communication-, monitor-, and event-data from the other subsystems are recorded into an EXABYTE 8-mm magnetic tape. Three Transputers and a subsystem controller (NEC V50) are employed for this task (see Figure 2.22). The subsystem controller receives the data from the Omninet and transmits them to the Transputer (TRP-1) which is interfacing the V50. Another Transputer (TRP-2) is connected with both the TRP-1 and the event-process subsystem via Transputer links. The TRP-2 multiplexes the data from Omninet and the event-process subsystem to the third Transputer (TRP-3) which handles the SCSI bus interface and records the data into the magnetic tape. The peak speed of the data transfer to the tape drive is 500 kbytes/s.

The data storage capacity of an 8-mm tape is 20 Gbytes and is not large enough to record all the data collected during a one-day flight. Therefore two tape drives were employed and the data recording was switched from one drive to the other serially after running through the first tape. The tape drives were housed in an iron steel box located outside the pressure vessel for the magnetic shield.

2.6.5 Monitor

The monitor subsystem handles the monitor-data which are sent from various sensors distributed in the payload for the house-keeping purpose. The transducers generate voltage outputs according to the measured values of temperature, pressure and attitude of the payload. Instrumentation amplifiers with differential inputs transform them into a common voltage range from 0 to 5 volts. A monitor module receives up to 64-channel inputs: temperatures (16 points), pressures (7 points), a magnet status (16 points), a chamber high voltage status (15 points), and solar sensors and clinometers. Those are multiplexed and digitized by a single 12-bit analog-to-digital converter. The subsystem controller (NEC V40) collects the digitized values for all channels. The data are transmitted to the ground station via the communication subsystem and are utilized to monitor and check the detector status during a flight. They are also transferred to the data-storage subsystem to be recorded for the off-line analysis.

2.6.6 Communication

The communication subsystem manages communication between the payload and the ground station. A serial radio link is used for the transmission media. As a transceiver terminal of the radio link, Consolidated Instrument

Package (CIP) is provided and attached to the payload by the National Scientific Balloon Facility (NSBF). The ground station sends commands to the payload through the radio link, and the CIP receives and interprets the commands as a 16-bit data. The communication subsystem controller fetches the data from the CIP and issues them into the Omninet, to be received by the other subsystem controllers. Inversely, responses to the commands, message-data generated constantly by all subsystems, monitor-data for the house-keeping, and event-data sampled at one-second intervals are sent via the communication subsystem controller to the CIP. Then the CIP sends them to the ground station through the radio link. Communication history is also recorded by the data-storage subsystem for off-line analysis.

Chapter 3

Flights Status

3.1 BESS-97 Scientific Flight

The BESS apparatus was launched from Lynn Lake, Manitoba, Canada in the evening of July 27. in 1997. In this flight, the balloon of 29 Mft^3 ($8.3 \times 10^5 \text{ m}^3$) lifted BESS detecotr into an altitude over 36 km (residual atmosphere of 5 g/cm^2). After about 22 hour level flight, the balloon flight was terminated under the condition of both magnetic field and power off. The instrument was recovered near Peace River, Alberta, which locates 1000 km east from Lynn Lake. During this level flight, a scientific data taking run were carried out for 18 hours. Total of 1.2×10^8 charged cosmic rays were triggered at T0 level and 1.69×10^7 of these triggers were recorded.

The environment in the pressure vessel was kept in good state, as shown in Figure 3.1.

3.2 BESS-98 Scientific Flight

In the '98 instrument, the refractive index of the aerogel was changed to be 1.02, however, the flight procedure was very similar to the previous one. BESS was successfully launched by a balloon from Lynn Lake air port in the evening of July 29. in 1998. The balloon lifted BESS into the alttude over 36 km (redidual atmosphere of 5 g/cm^2) for 21 hours. During the level flight, thata includes 17 hours scientific data taking time, total of 1.1×10^8 charged cosmic rays were triggered at T0 level and 1.68×10^7 events were recorded. The environment in the pressure vessel was kept in good state, as shown in Figure 3.2.

3.3 Trigger conditions

Trigger parameters were carefully adjusted to achieve the desired trigger rate, based on the counting rate obtained in the short test run just before the level flight. The actual trigger rates derived from the scaler data are summarized in Table 3.1 for T0 trigger and 3.2 for Master trigger.

A calibration run of 100 seconds was carried out every hour to re-adjust the thresholds for FADC data suppression as low as possible, because the pedestal value of FADC outputs varied depending on temperature.

Table 3.1: The conditions of the T0 trigger and the trigger rates.

Mode	Top			Bottom			Ext	Sample Rate	T0 Trigger
	Low	High	Hich	Low	High	Hich			
'97 Flight									
T0-Low	1	x	x	1	x	x	x	1/1	2.1 kHz
T0-High	x	1	x	x	1	x	x	1/1	270 Hz
T0-High_ch	x	x	1	x	x	1	x	1/1	11 Hz
T0-external	x	x	x	x	x	x	1	1/1	1.25 Hz
'98 Flight									
T0-Low	1	x	x	1	x	x	x	1/1	2.1 kHz
T0-High	x	1	x	x	1	x	x	1/1	330 Hz
T0-High_ch	x	x	1	x	x	1	x	1/1	13 Hz
T0-external	x	x	x	x	x	x	1	1/1	1.45 Hz

1 : Signal should be asserted.

0 : Signal should not be asserted.

x : Signal is not concerned.

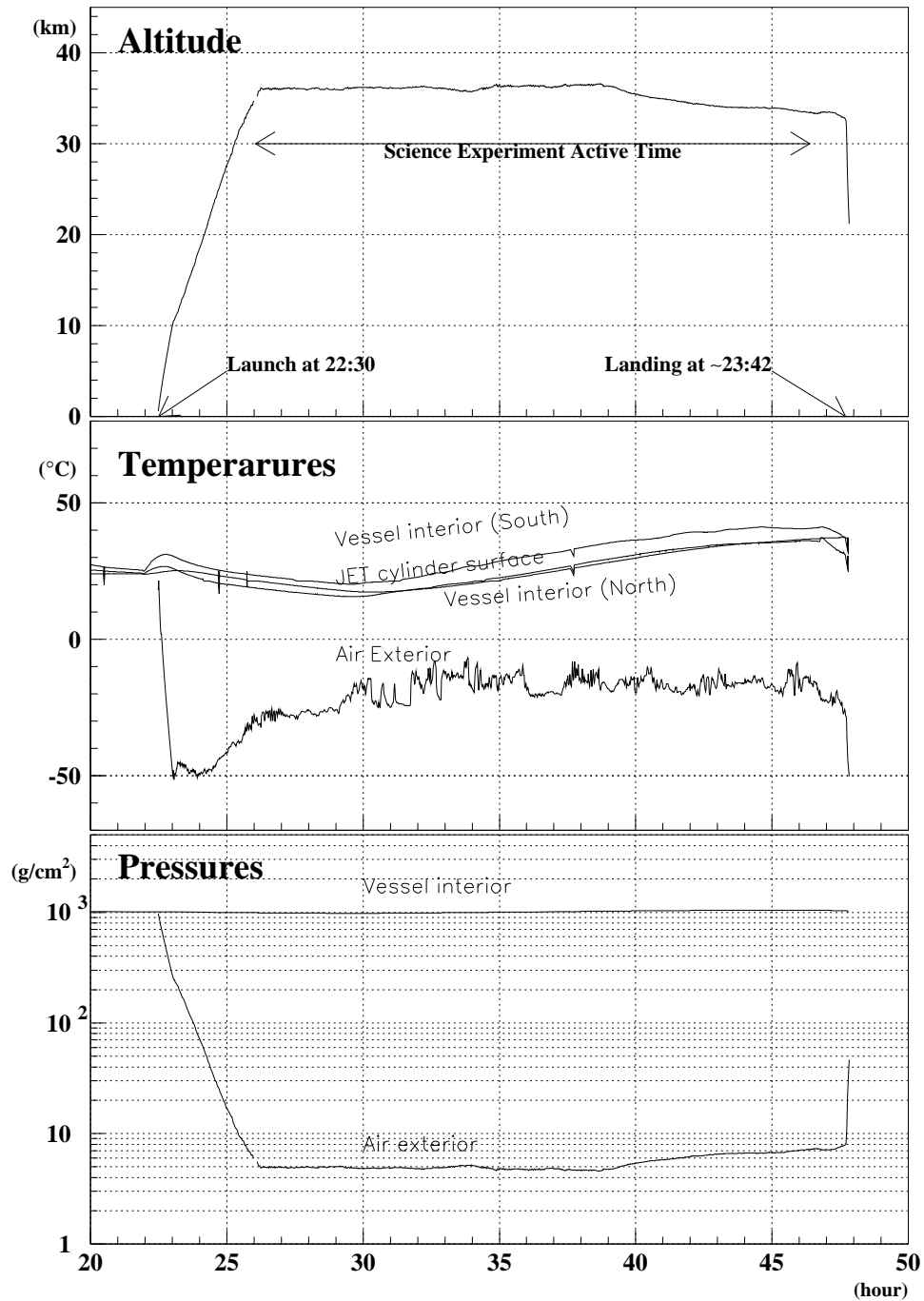


Figure 3.1: House-keeping data on altitude, temperatures and pressures in BESS '97 flight.

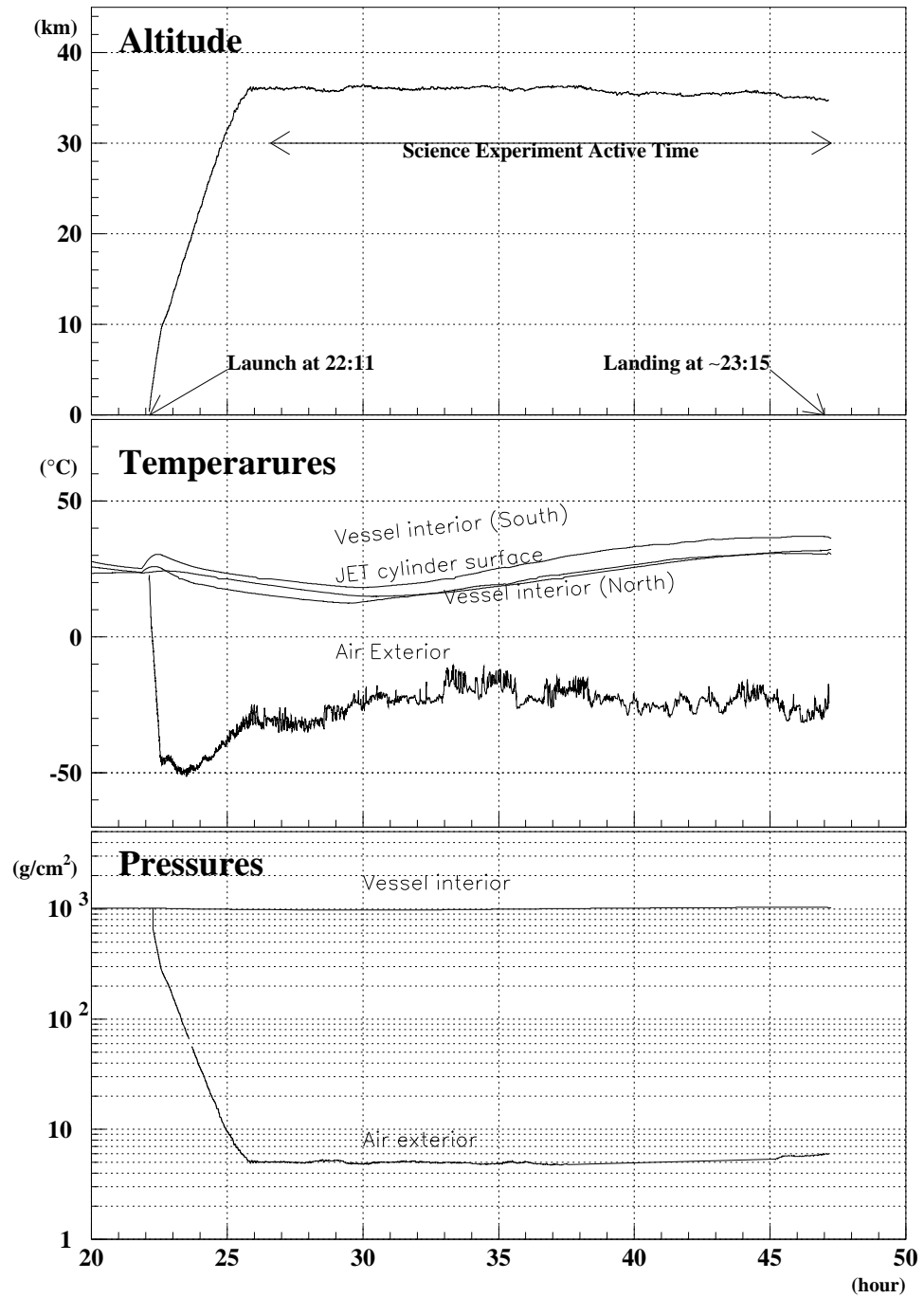


Figure 3.2: House-keeping data on altitude, temperatures and pressures in BESS '98 flight.

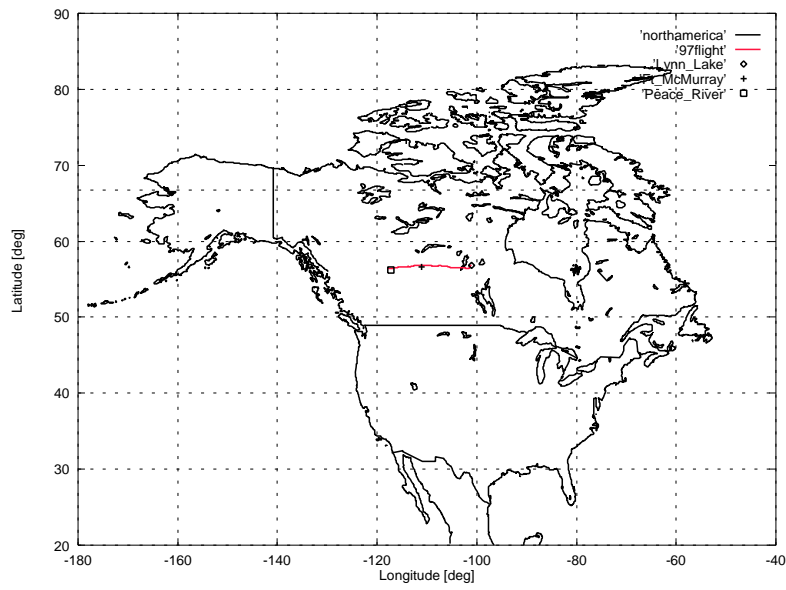


Figure 3.3: Flight trajectory for BESS '97.

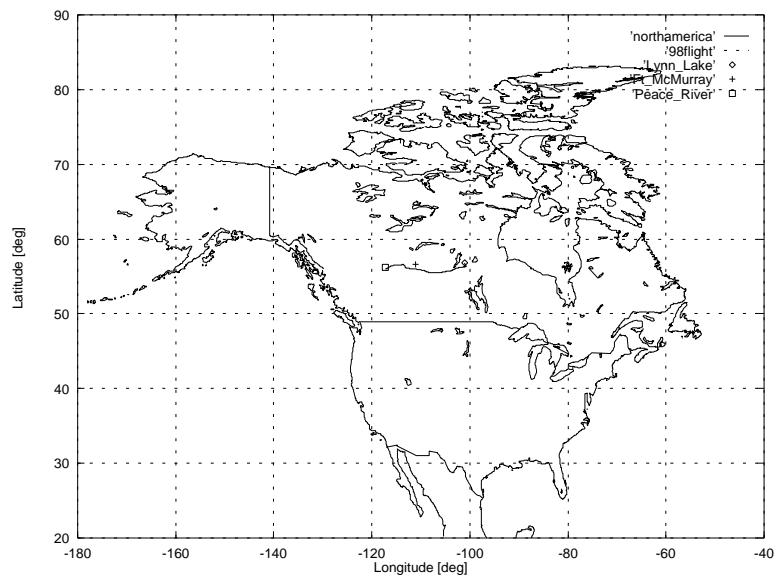


Figure 3.4: Flight trajectory for BESS '98.

Table 3.2: The settings of the Master Trigger and the trigger rate ('97 and '98).

MT Mode		T0 Mode Mask	Sampling	Accepted	Triggered
'97 Flight					
Biased	\bar{p} -clear	1 0 0 0	1/1	140 Hz	120 Hz
	\bar{p} -dirty	1 0 0 0	1/1	42 Hz	37 Hz
	$\overline{\text{He}}$ -clear	0 1 0 0	1/1	24 Hz	21 Hz
	$\overline{\text{He}}$ -dirty	0 1 0 0	1/1	13 Hz	12 Hz
	Missing-a-hit	1 1 0 0	1/1	29 Hz	26 Hz
	Multi-clear	1 1 0 0	1/1	3.7 Hz	3.3 Hz
	Multi-dirty	1 1 0 0	x	0 Hz	0 Hz
	Gamma	0 0 1 0	x	0 Hz	0 Hz
Unbiased	T0-Low	1 0 0 0	1/60	2.1 kHz	35 Hz
	T0-High	0 1 0 0	1/25	270 Hz	11 Hz
	T0-High_ch	0 0 1 0	1/1	11 Hz	11 Hz
	T0-External	0 0 0 1	1/1	1.25	1.25 Hz
Total				2.1 kHz	260 Hz
'98 Flight					
Biased	\bar{p} -clear	1 0 0 0	1/1	180 Hz	150 Hz
	\bar{p} -dirty	1 0 0 0	1/1	51 Hz	43 Hz
	$\overline{\text{He}}$ -clear	0 1 0 0	1/1	28 Hz	24 Hz
	$\overline{\text{He}}$ -dirty	0 1 0 0	1/1	16 Hz	14 Hz
	Missing-a-hit	1 1 0 0	1/1	26 Hz	22 Hz
	Multi-clear	1 1 0 0	1/1	35 Hz	30 Hz
	High-p	1 0 0 0	1/1	158 Hz	130 Hz
	High-p	1 0 0 0	1/1	158 Hz	130 Hz
Unbiased	T0-Low	1 0 0 0	1/60	2.1 kHz	36 Hz
	T0-High	0 1 0 0	1/25	330 Hz	13 Hz
	T0-High_ch	0 0 1 0	1/1	13 Hz	13 Hz
	T0-External	0 0 0 1	1/1	1.45 Hz	1.45 Hz
Total				2.1 kHz	360 Hz

Chapter 4

Search for Antihelium

4.1 Flight Data Sample

As already mentioned in Chapter 3, the data acquisition was stopped every hour to take some calibration data, yielding 21 data acquisition runs in 1997 flight and 22 runs in 1998 flight, respectively.

In Table 4.1 and 4.2 are summarized the number of events in each run, where T0 is the number of the T0 triggers at the first level, Master is the number of the MT trigger, *i.e.*, the number of the events the data acquisition system collected. The right half of the table shows the trigger modes of the recorded data, each of which corresponds to the Master Trigger mode. (see also Table 3.2). We have had the third level trigger since 1997 flight, and used it from the last half run (17 ~ 22), but changed other trigger conditions. In 1998 flight, we used the third level trigger from the beginning of the flight.

The first step of the data processing was to decompress the raw flight data which contain event data, house-keeping data, command and message data. To analyze the data, we extract properties of hits in detector components and trigger conditions from event data. The event frames had different sizes varying from several hundred to three kilo bytes depending on the number of hits in detectors, and then variable length data format is needed. The ZEBRA [28] system of CERN program library was employed to store the properties extracted from the raw flight data, because it has dynamic data structuring capability with tree structures of data storage units (called 'bank') and linkage of these structures. The HEPDB [29] database management package of CERN program library, which is available in the ZEBRA system, was employed to store the geometries of the detector components, the read-out channel assignment tables and the calibration parameters.

Table 4.1: Summary of BESS flight data ('97).

run #	time ($\times 10^3$ s)	T0 ($\times 10^6$)	Master ($\times 10^6$)	Record ($\times 10^6$)	T0 L ($\times 10^5$)	T0 H ($\times 10^5$)	MT \bar{p} ($\times 10^5$)	MT $\bar{\text{He}}$ ($\times 10^5$)
97-2	3.36	6.28	1.01	1.00	1.19	0.36	6.07	1.27
3	3.83	7.00	1.13	1.11	1.36	0.41	6.78	1.42
4	3.39	6.37	1.03	1.01	1.21	0.37	6.17	1.29
5	3.38	6.33	1.02	1.00	1.20	0.37	6.10	1.28
6	3.42	6.42	1.04	1.02	1.22	0.37	6.20	1.30
7	3.64	6.86	1.11	1.09	1.30	0.39	6.62	1.38
8	3.68	6.95	1.12	1.10	1.32	0.39	6.73	1.39
9	3.56	6.65	1.07	1.06	1.26	0.37	6.44	1.33
10	0.74	1.37	0.22	0.22	0.26	0.08	1.33	0.27
11	3.32	6.19	1.00	0.99	1.17	0.34	6.02	1.24
12	3.49	6.51	1.05	1.04	1.23	0.35	6.31	1.29
13	3.52	6.55	1.06	1.04	1.24	0.35	6.36	1.29
14	1.10	2.05	0.33	0.33	0.39	0.11	1.99	0.40
15	3.53	6.52	1.05	1.04	1.24	0.34	6.34	1.27
16	3.21	5.98	0.96	0.95	1.13	0.30	5.81	1.14
17	2.71	5.06	0.81	0.45	0.96	0.25	4.91	0.95
18	2.43	4.52	0.73	0.40	0.85	0.22	4.40	0.85
19	3.52	6.45	1.03	0.57	1.24	0.31	6.27	1.20
20	3.47	6.45	1.03	0.58	1.22	0.30	6.27	1.19
21	3.68	5.92	0.95	0.53	1.29	0.32	5.77	1.09
22	2.50	5.92	0.95	0.41	0.88	0.21	4.53	0.84
97-total	65.48	122.35	19.70	16.94	23.16	6.51	117.42	23.68

Table 4.2: Summary of BESS flight data ('98).

run #	time ($\times 10^3$ s)	T0 ($\times 10^6$)	Master ($\times 10^6$)	Record ($\times 10^6$)	T0 L ($\times 10^5$)	T0 H ($\times 10^5$)	MT \bar{p} ($\times 10^5$)	MT $\bar{\text{He}}$ ($\times 10^5$)
98-4	2.95	5.53	1.27	0.86	1.07	0.39	6.91	1.30
5	3.03	5.68	1.31	0.88	1.10	0.40	7.09	1.32
6	2.91	5.46	1.26	0.85	1.05	0.39	6.81	1.29
7	2.95	5.54	1.28	0.86	1.07	0.40	6.89	1.32
8	2.66	4.99	1.15	0.78	0.96	0.36	6.22	1.18
9	2.94	5.51	1.27	0.86	1.06	0.40	6.84	1.30
10	3.05	5.72	1.32	0.89	1.10	0.41	7.12	1.36
11	3.03	5.70	1.32	0.89	1.10	0.41	7.12	1.36
12	0.46	0.87	0.20	0.14	0.24	0.09	1.09	0.21
13	3.00	5.72	1.32	0.89	1.11	0.40	7.13	1.34
14	1.51	2.88	6.66	0.45	0.61	0.22	3.61	0.68
15	3.03	5.78	1.33	0.90	1.12	0.40	7.24	1.36
16	3.00	5.73	1.32	0.89	1.11	0.39	7.17	1.34
17	3.02	5.77	1.33	0.89	1.11	0.38	7.21	1.32
18	3.01	5.72	1.31	0.89	1.10	0.37	7.15	1.30
19	2.84	5.40	1.24	0.84	1.07	0.36	6.76	1.22
20	2.94	5.58	1.28	0.86	1.07	0.35	6.97	1.26
21	2.77	5.21	1.19	0.80	1.00	0.33	6.53	1.18
22	2.95	5.54	1.27	0.85	1.06	0.35	6.95	1.25
23	0.85	1.59	0.36	0.24	0.31	0.10	2.00	0.36
24	3.13	5.86	1.34	0.91	1.13	0.36	7.36	1.31
25	1.34	5.86	1.34	0.40	0.50	0.16	3.25	0.58
98-total	57.37	111.64	31.67	16.82	21.05	7.42	135.42	25.14

The off-line calibrations were made on each run to derive temperature-dependent or pressure-dependent parameters, for instance, timing offsets in TOF measurement and drift velocity in the drift chambers.

Primary calibrations were performed to obtain pedestals and gain factors. After initial calibrations, pattern recognition was performed using the hits of JET chamber to find tracks of the incident particles and track information banks are formed. The hits of IDC and TOF made by the particle were acquired by extrapolating the fitted trajectory of the track and then linked to the track information bank. Thus, all informations of the hits which an incident particle induced on the detectors were to be retrieved by accessing the track information bank, and the properties of the particle were to be obtained.

Detailed calibrations were performed using the track information retrieved as above. In order to reduce the time consumption or the process, the information of the track and associated hits were stored into data summary files, which are flat files consisting of fixed length records. The results of the calibrations were put into the database, and pattern recognition and track fitting were performed in the ZEBRA-based system again. The final data summary files were obtained from the re-created track information banks and were used for the further analysis.

4.2 Event Reconstruction

4.2.1 Track Reconstruction

The rigidity of a particle was determined by the JET and IDC drift chambers. First the transverse rigidity (R_t), the rigidity component perpendicular to the magnetic field direction, was determined by circular fitting in the $r\phi$ -plane (Fig. 4.1).

In order to select the hits induced by the particle in the trajectory fitting, the following algorithm was employed.

1. Select ‘good’ hits, which are defined as hits with enough charge and width.
2. Find trajectories by connecting the ‘good’ hits in JET chamber and perform circular fitting.
3. Extrapolate each of the trajectories to IDCs to find ‘good’ IDC hits near the trajectory, they are associated to the track.

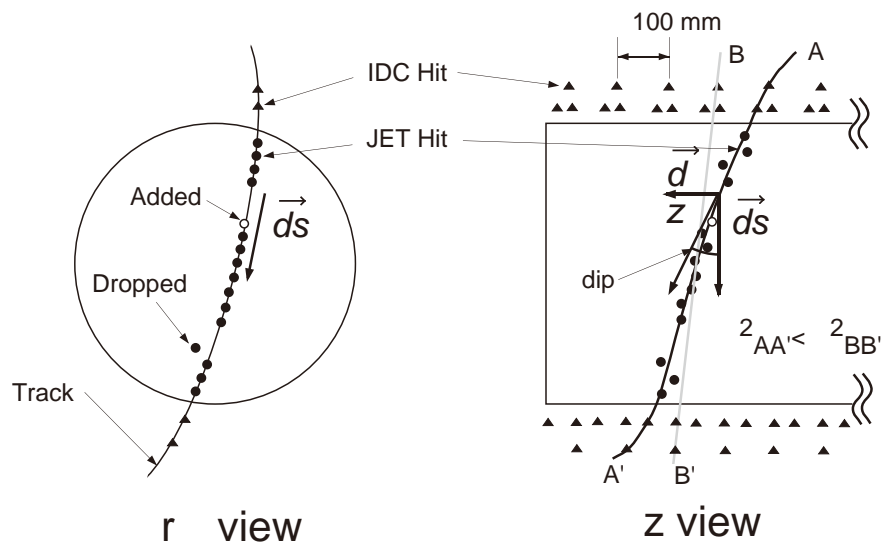


Figure 4.1: Method of the rigidity measurement.

4. Perform trajectory fitting again using all hit points in the JET and IDCs which are associated to the track. We used ‘Karimäki method’ [32] for the fitting algorithm at this stage.
5. Scan all of ‘good’ hits in JET chamber and check if they are well close to the track, *i.e.*, within the distance 5times of the position resolution, 5σ . Only the hits checked here are used in the following processes.
6. Repeat step 4) and 5) twice.

The resultant R_t should be then corrected for non-uniformity of the magnetic field, which varies up to 10%. Monte Carlo calculations with the computed magnetic field indicates that the correction factor to the rigidity of various trajectories, expressed as a function of the track position, path length, and mean strength of B field, is able to obtain the corrected rigidity which is within an relative accuracy of 0.2% from the actual one.

To obtain the total rigidity (R) from R_t , we find the dip angle θ_{dip} , which is defined as an angle between the $r\phi$ -component ($\vec{d}s$) and the z -component ($\vec{d}z$) of R , by fitting in the yz -plane (Fig. 4.1). We use a similar iterative procedure as used in the $r\phi$ fitting to eliminate irrelevant hits. The selected hits are fitted to a sine-curve. Since the IDCs provide the only z positions modulo $100mm$, all possible combinations of the IDC hits are examined. The resultant θ_{dip} are obtained from the combination having minimum χ^2 value in the fitting.

Finally rigidity R are derived from R_t and θ_{dip} as;

$$R = \frac{R_t}{\cos\theta_{dip}}$$

4.2.2 Time-of-Flight Measurement

Figure 4.2 illustrates the measurement scheme of time-of-flight (TOF). The TOF between top and bottom TOF hodoscopes is calculated for each track by the following procedure. We use here the suffix ‘elec’ for the PMT on the side of the electronics and the suffix ‘tank’ for the PMT on the side of the helium reservoir tank.

1. Correct a timing walk using the charge information for each PMT. We use following formulae:

$$\hat{t}_{elec} = t_{elec} - a_i / \sqrt{q_{elec}},$$

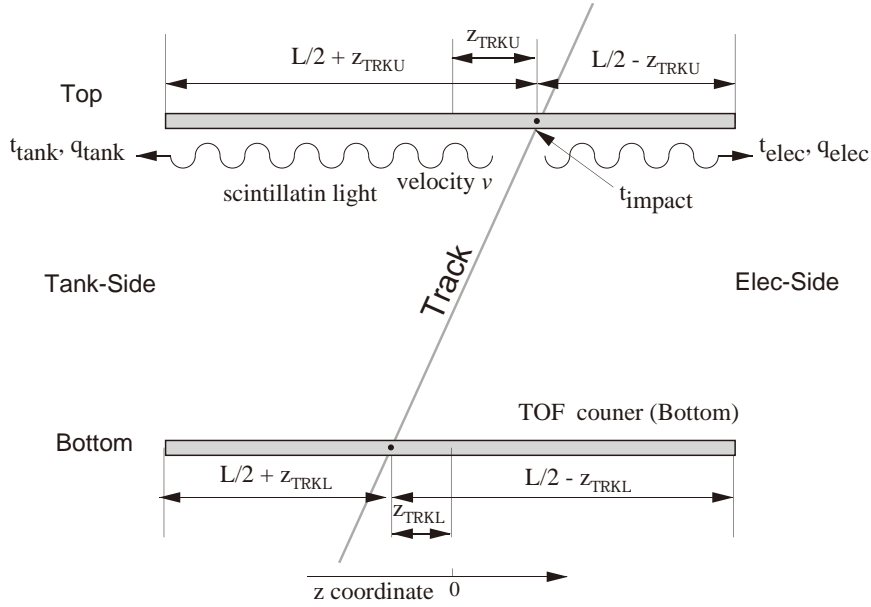


Figure 4.2: Method of the TOF measurement.

and

$$\hat{t}_{tank} = t_{tank} - a_i / \sqrt{q_{tank}},$$

where $t_{elec,tank}$ is the measured timing, $\hat{t}_{elec,tank}$ the timing after the correction, q the measured charge of the PMT, and a_i is the correction parameter of the i th PMT. Parameter a_i was determined by the beam test.

- Derive the timing that the particle passed through the counter (t_{impact}) from the corrected timing of each PMT. Using the z -impact point (z_{trku}, z_{trkl}) of the particle which is calculated by extrapolating the combined track, t_{impact} is obtained for elec-side as;

$$t_{elec}^{impact} = \hat{t}_{elec} - \frac{\frac{L}{2} - z_{trku, trkl}}{v_{eff}} - t_{offset}(z_{trku, trkl}),$$

and for tank-side as,

$$t_{tank}^{impact} = \hat{t}_{tank} - \frac{\frac{L}{2} - z_{trku, trkl}}{v_{eff}} - t_{offset}(z_{trku, trkl}),$$

where v_{eff} is the effective light velocity in the counter and L is the length of the counter including light guides. The second term is the propagation time for the scintillation light to reach to each PMT. The last term $t_{offset}(z)$ is the timing offset as a function of the z position. This is introduced to correct the effective velocity variation depending on the z position and is determined by calibration for each counter. The averaged impact time of the counter is then obtained as;

$$t_{impact} = \left(\frac{t_{elec}^{impact}}{\sigma_{elec}(z)^2} + \frac{t_{tank}^{impact}}{\sigma_{tank}(z)^2} \right) / \left(\frac{1}{\sigma_{elec}(z)^2} + \frac{1}{\sigma_{tank}(z)^2} \right),$$

where $\sigma(z)$ is the timing resolution of the each PMT as a function of z .

3. The value t_{impact} is individually calculated for both top and bottom counters, and then the TOF is obtained as the time difference between them.

The $\beta \equiv v/c$ of the particle can be determined from the TOF and the path length derived from the trajectory.

4.2.3 dE/dx Measurement

The energy deposit of a particle, dE/dx , in a scintillator is derived from the pulse size of the PMT output, which is measured by ADC as a charge, by following steps:

1. Subtract the pedestal value from the ADC count and correct it for the gain of PMT and ADC.

$$q = (\text{count} - \text{pedestal})/\text{gain}$$

The gain is determined by the calibration to normalize the energy deposit dE/dx of minimum ionizing particle to be 1.

2. Correct the z dependence of the signal amplitude due to the attenuation of scintillation light in the scintillator using the z -impact position of the extrapolated track. The detailed study shows that the measured charge $q_{measured}$ has the z dependence as follows:

$$q_{measured} \simeq (a + be^{cz})dE,$$

where a, b and c are parameters that should be determined by the calibration, and dE is the deposited energy.

3. Average the energy deposit dE derived from the PMT signals of two ends both at top and bottom counters.
4. Divide the average energy deposit by the path length in the scintillator through which the particle passed. This gives dE/dx in the TOF counters.

The energy deposit in the JET chamber is also calibrated and utilized following analysis. Because the JET chamber is filled with the slow gas, it was found that space charge effect degrades the dE/dx resolution, particularly in the high charge region. After an exhaustive study of the effect, the correction method for saturated charge is obtained as follows:

1. Subtract the pedestal value from the FADC charge and normalize it in each channel.
2. The degree of saturation greatly depends on the inclination of the track towards the z -direction (θ_z) and also slightly depends on the inclination of the track in the $r\phi$ -plane ($\theta_{r\phi}$). Using pure helium and proton samples, charge is corrected for (θ_z) by fitting to the data as a two-dimensional function, and then corrected for ($\theta_{r\phi}$), in each wire.
3. The correction for drift length is applied to obtain dE because of loss of charge by the diffusion during the drift.
4. Divide the dE by the path length for the wire in the gas through which the particle passed. This gives dE/dx for one wire.
5. In order to remove Landau tail or δ ray effects, truncated mean method is applied in which lower 10 % and higher 50 % of measured dE/dx values are removed and the rest are used to calculate the mean dE/dx .

4.3 Event Selections

4.3.1 Single Track Selection

The T0 trigger requires only the coincidence of the hits at the top and the bottom scintillation counters, and the MT trigger requires the hits in IDCs and TOFs. Thus, there are events in which the incident particle did not pass through JET chamber, or left too few hits in it to reconstruct the track with a desired accuracy. We exclude such events and use events with a long enough track in the analysis, which corresponds to a reduction of the geometrical acceptance of the instrument. There are also events which contain multi-tracks or too many hits in the detectors. A shower-like event with too many hits makes it difficult to reconstruct the tracks, and a multi-track event is not fiducial in the TOF measurement, for more than one track might have passed through the same scintillator, or the incident particle might have been scattered and changed its direction and energy. Following cuts were applied to obtain reconstructible events with a good single track which passed through the fiducial region for JET chamber.

1. $N_{\text{TOFU}} = 1 \quad N_{\text{TOFL}} = 1 \text{ or } 2$

There should be one and only one hit in the scintillation counters at the top and, taking the delta lay into account, we permit one more hit at the bottom.

2. $N_{\text{longtrack}} = 1$

The number of tracks with 10 or more hits found in JET chamber should be one and only one.

3. $N_{\text{expect}} \geq 20$

The number of hits in JET chamber expected from the trajectory N_{expect} is 20 or more. This cut defines the fiducial region of the JET chamber and eliminates the track which scratches the outermost region, where the position measurement is less accurate than the central region due to the distortion of the electric field.

After this selection, we have exactly one track in an event to analyze. Total 8,849,936 (8,288,879) events, including 180,708 (198,809) unbiased trigger events, passed through this cut in 1997 (1998) flight.

4.3.2 β Selection

The velocity β of the observed particles can be calculated from the mass m , charge e , and rigidity R as

$$\frac{1}{\beta^2} = \left(\frac{m}{e}\right)^2 \frac{1}{R^2} + 1$$

Then we have a band structure in a plot for $1/\beta$ vs. rigidity according to the value of (m/e) as shown in Figure 4.3 (4.4). Theoretical values for ${}^3\text{He}$ and ${}^4\text{He}$ are denoted in dashed lines in the plot. To extract ${}^3\text{He}$ and ${}^4\text{He}$ samples, a cut indicated by the solid lines is applied.

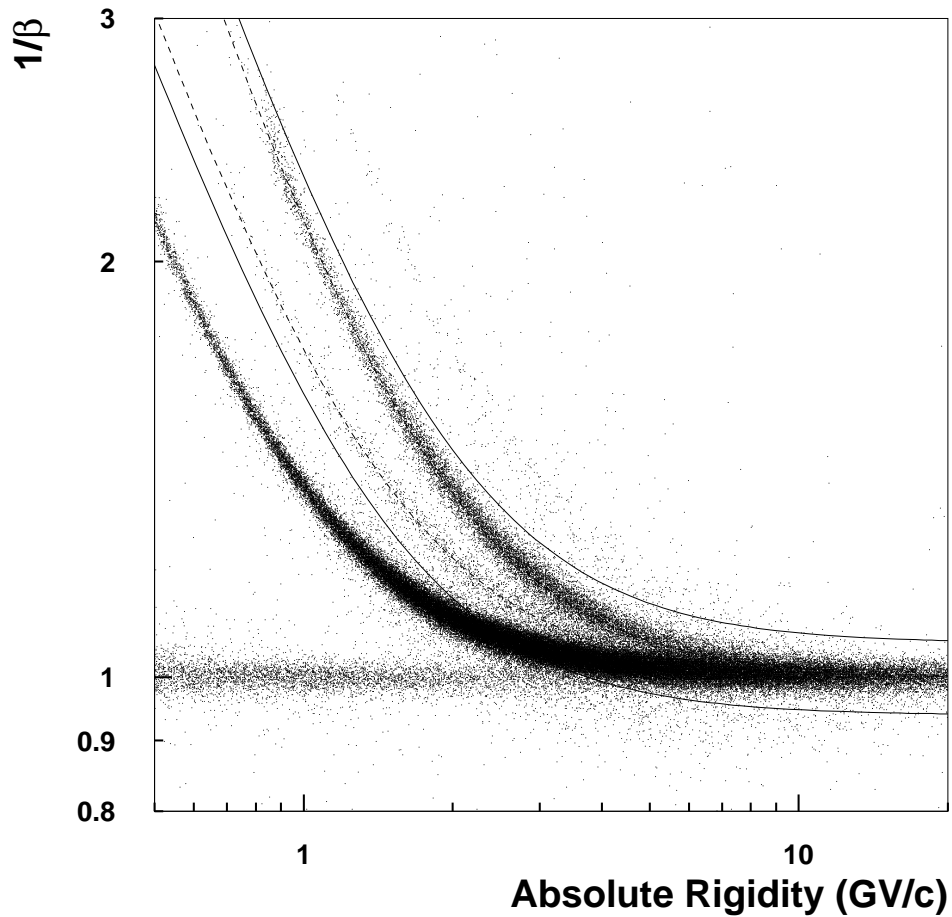


Figure 4.3: β^{-1} vs. rigidity ('97)

4.3.3 dE/dx selection

We utilize the band structures in dE/dx - rigidity plot to extract only heliums and antiheliums among other species. Figure 4.5 (4.6) and 4.7 (4.8) show dE/dx -versus-rigidity plots of the upper and the lower scintillators in 1997 (1998) flight. The solid lines is determined to contain the 99.9 % of helium (antihelium) assuming Vavilov or Landau distribution (see fig 4.11). The dashed lines is the peak of ^3He and ^4He fitted with Bethe-Bloch equation. Figure 4.9 (4.10) show dE/dx -versus-rigidity plots of the JET chamber with cut lines.

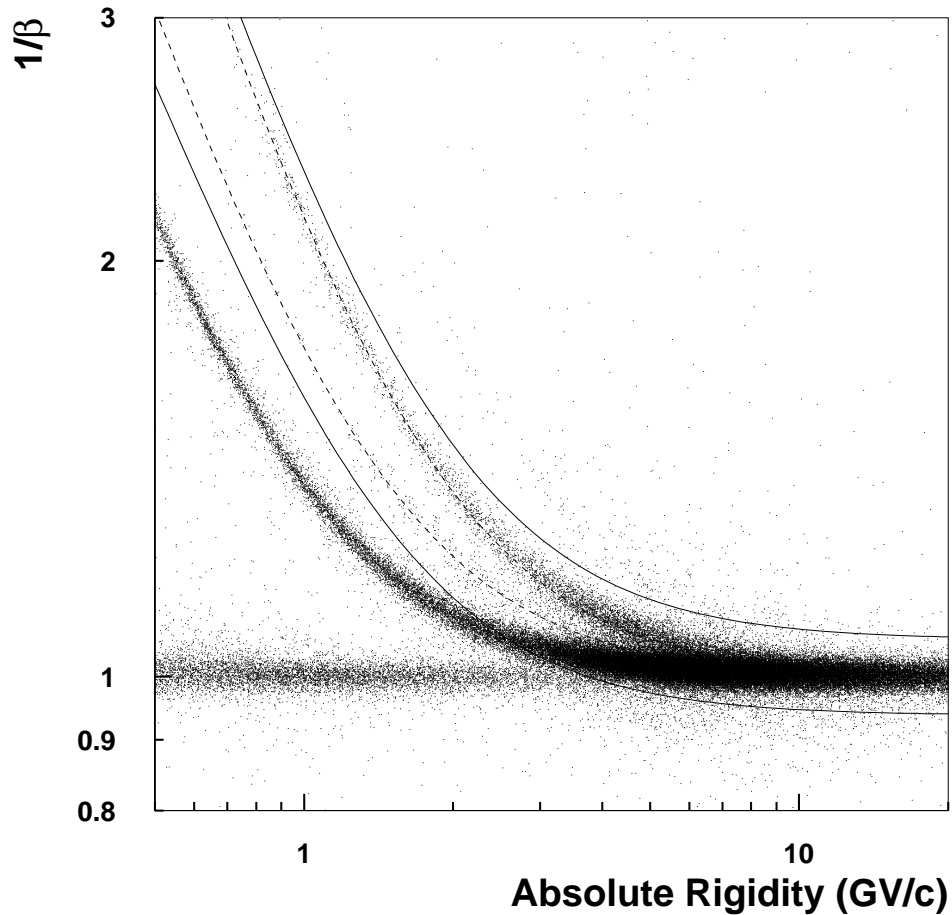


Figure 4.4: β^{-1} vs. rigidity ('98)

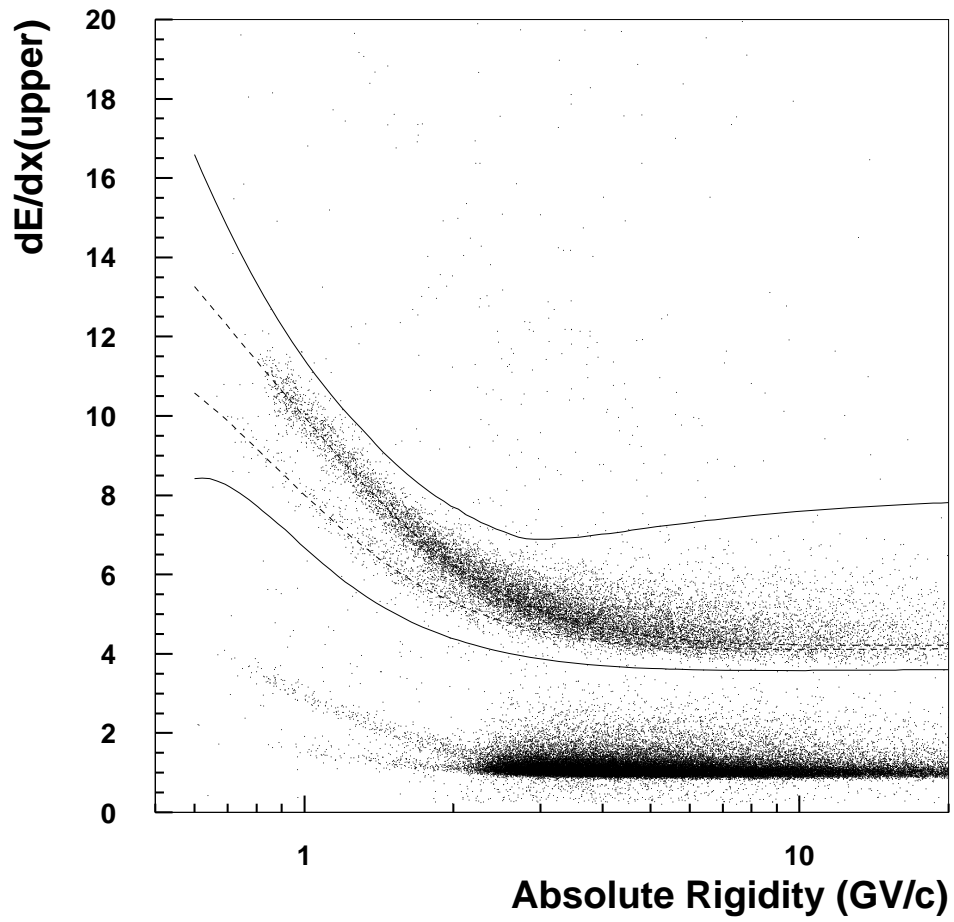


Figure 4.5: $dE/dx(\text{upper})$ vs. rigidity after β cut ('97)

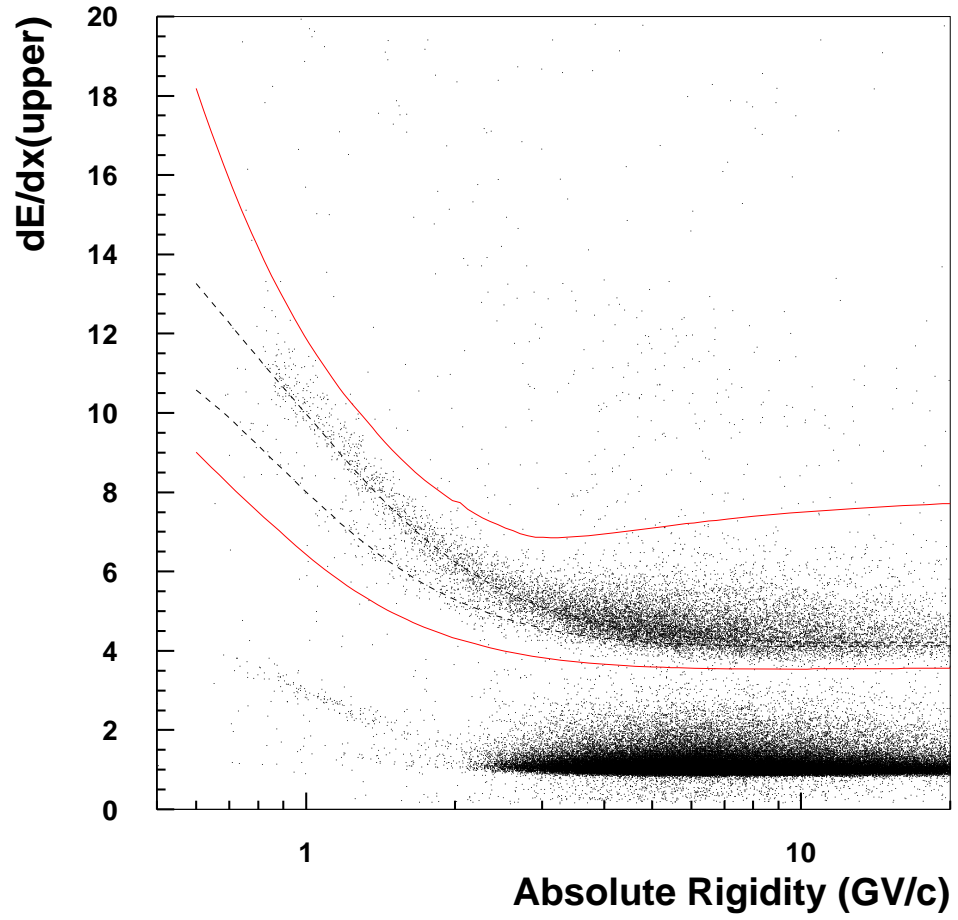


Figure 4.6: $dE/dx(\text{upper})$ vs. rigidity after β cut ('98)

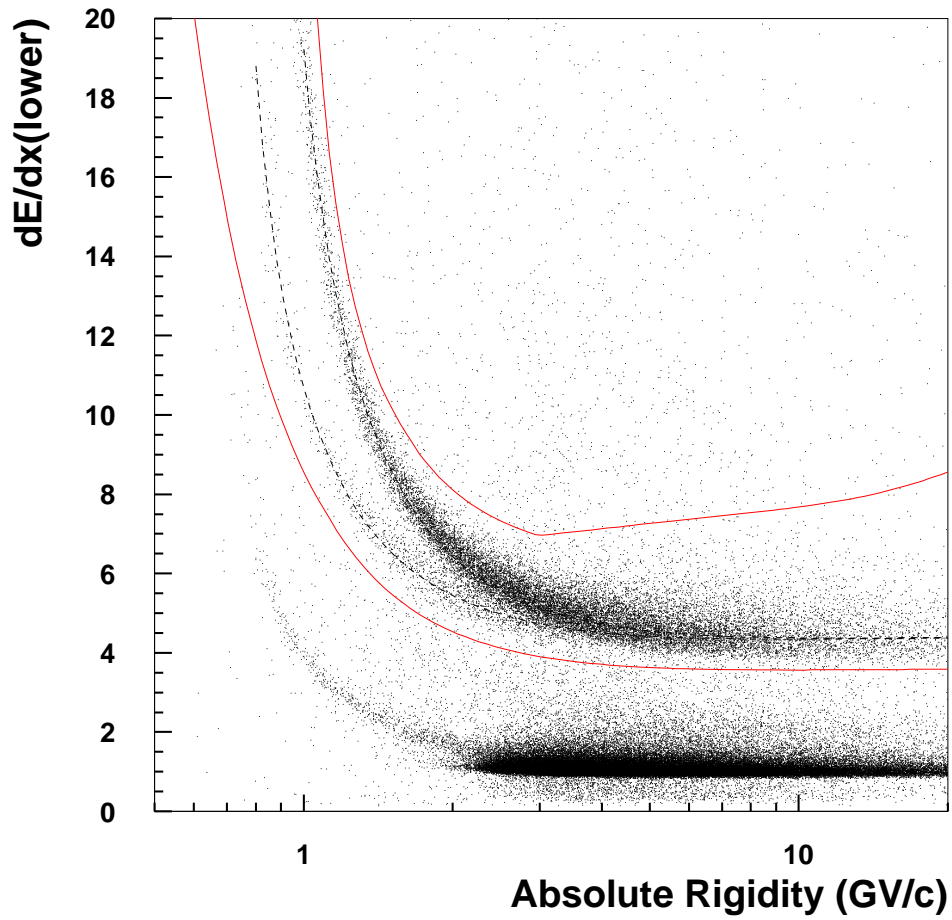


Figure 4.7: $dE/dx(\text{lower})$ vs. rigidity after β cut ('97)

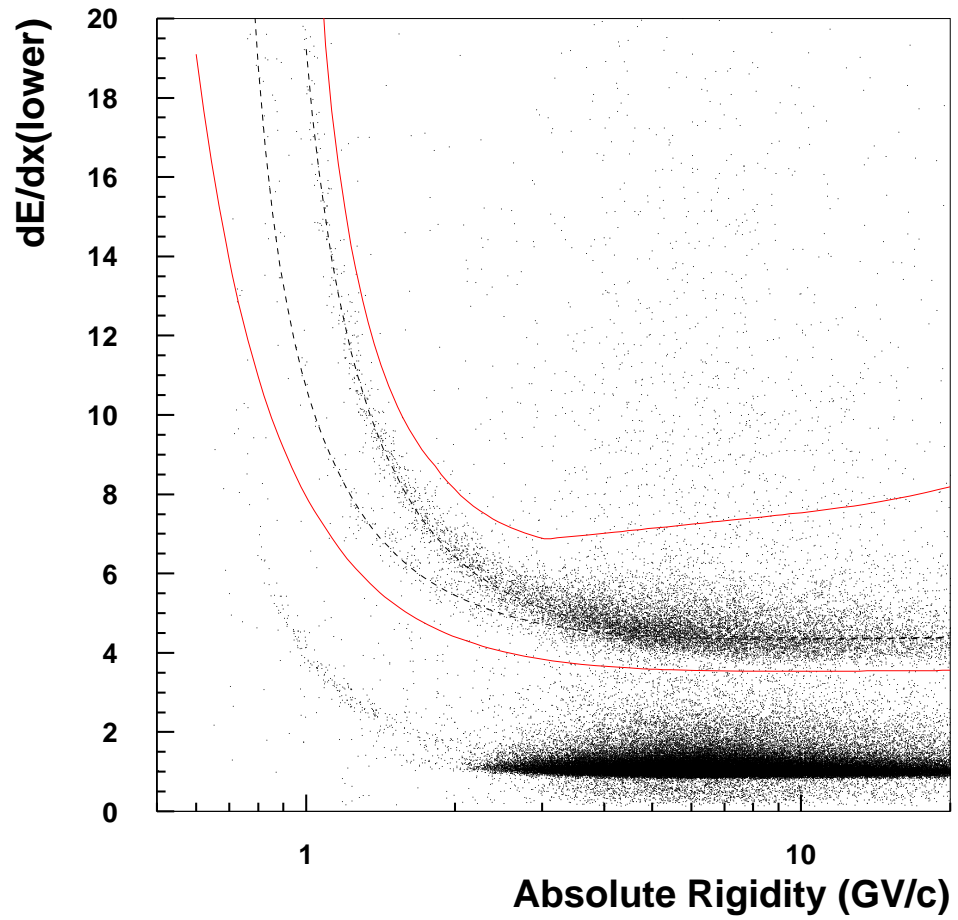


Figure 4.8: $dE/dx(\text{lower})$ vs. rigidity after β cut ('98)

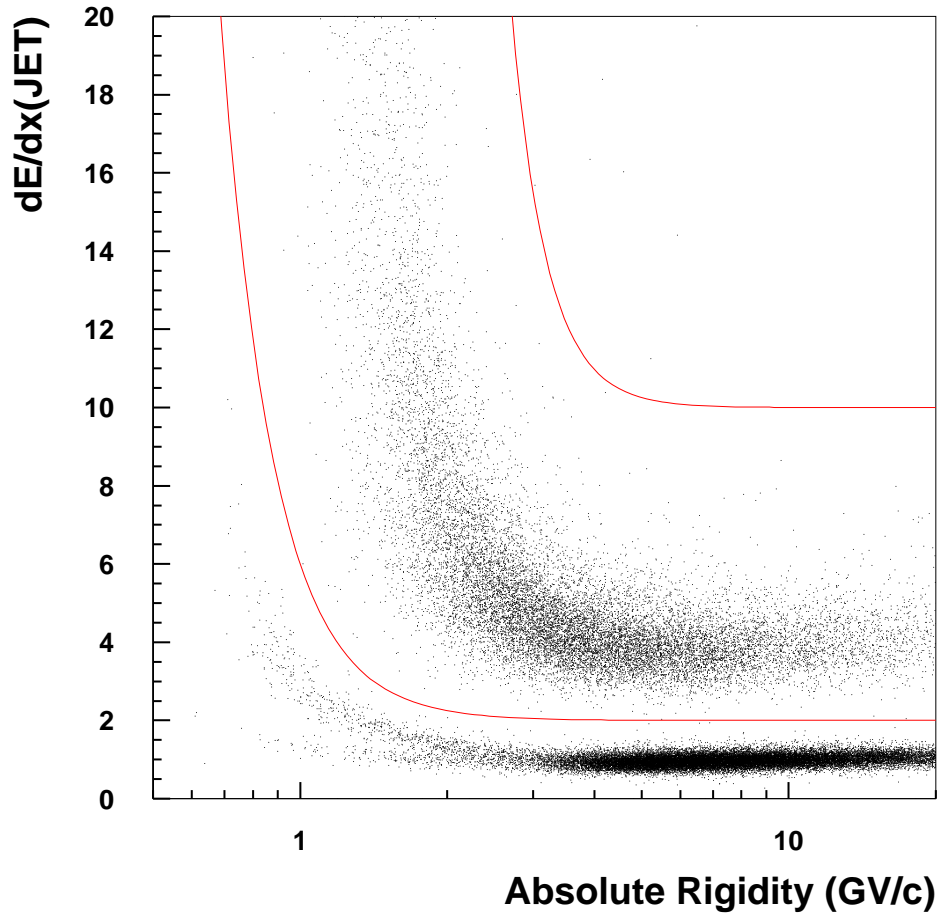


Figure 4.9: $dE/dx(\text{JET})$ vs. rigidity after β cut ('97)

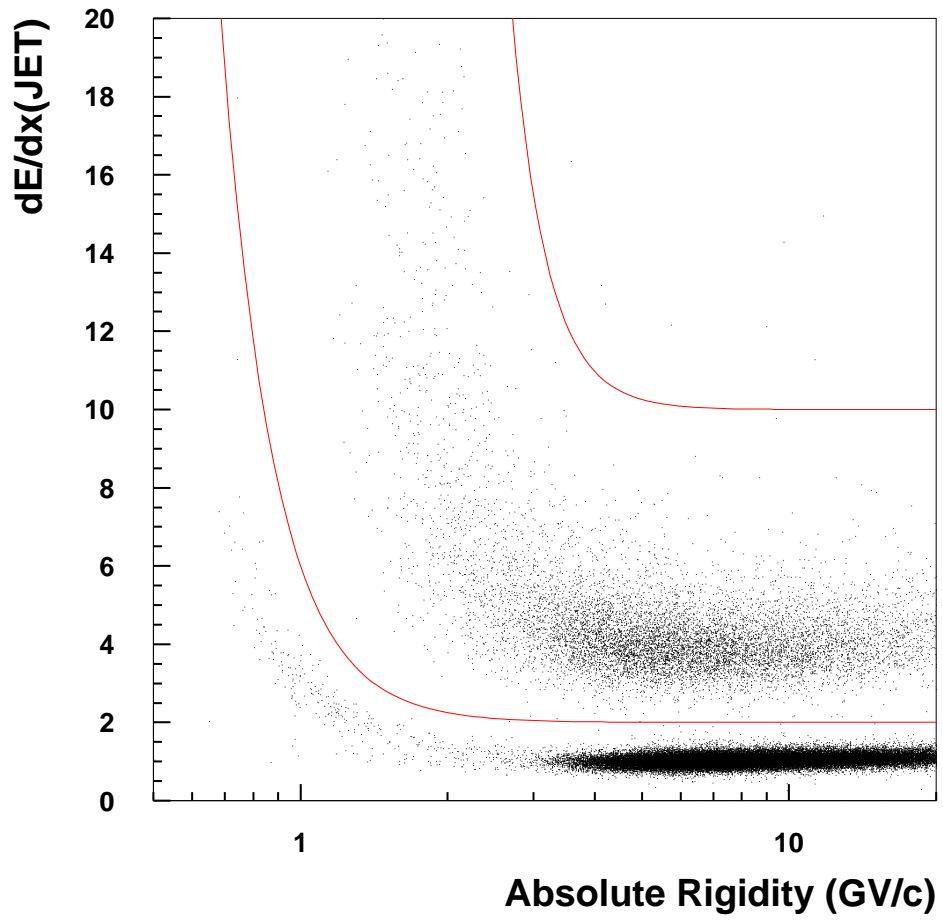
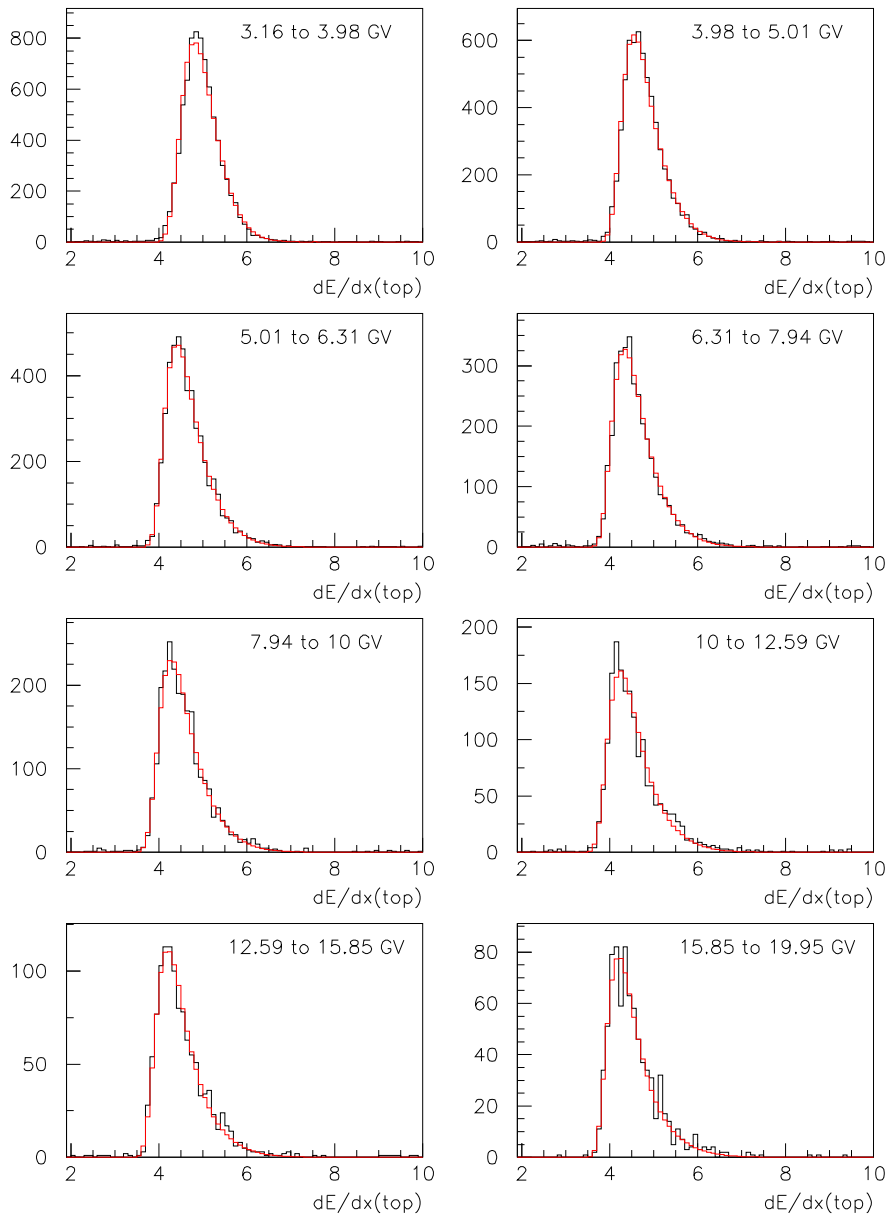


Figure 4.10: $dE/dx(\text{JET})$ vs. rigidity after β cut ('98)

Figure 4.11: $dE/dx(\text{upper})$ distribution at various rigidities.

4.4 Track Quality Cut

Following cuts were applied to ensure a quality of the single track.

1. $N_{r\phi\text{-fit}} \geq 16$
The accuracy of the track information depends on the number of hits used in the trajectory fitting.
2. $N_{z\text{-fit}} \geq 6$
Since the number of wires to determine z -position is less than that for $r\phi$ -position determination, the limit on the number of utilized hits in z -trajectory fitting is lowered than in $r\phi$ -fitting.
3. $\chi_{r\phi}^2 < 5$
4. $\chi_z^2 < 5$
The goodness of fits can be checked using the reduced chi-square parameters:

$$\chi_{r\phi}^2 \equiv \frac{1}{\sqrt{N_{r\phi\text{-fit}} - 3}} \sqrt{\sum \frac{(\Delta(r\phi)_i)^2}{\sigma_{r\phi,i}^2}},$$

$$\chi_z^2 \equiv \frac{1}{\sqrt{N_{z\text{-fit}} - 2}} \sqrt{\sum \frac{(\Delta(z_i))^2}{\sigma_{z,i}^2}}.$$

5. $N_{\text{drop}} < 4$.
A “dropped” hit is a JET hit satisfying the following two conditions; (1) which is expected from the trajectory (2) while actually not existing close to the expected position. We count the number of “dropped” hits (N_{drop}), which should be less 4 to avoid wrong reconstruction of the trajectory.
6. $\Delta(r\phi)_{IDC1i}, \Delta(r\phi)_{IDC1o} \leq 1.0\text{mm}$,
 $\Delta(r\phi)_{IDC2i}, \Delta(r\phi)_{IDC2o} \leq 1.0\text{mm}$

The IDC hits are outermost hits used in trajectory fitting and provide information independent of JET hits. We required that good hit in each IDC is close enough to the trajectory. In the data summary files are stored the information of one hit in each layer of IDCs (IDC1i for the inner layer of the upper IDC, or IDC1; IDC2o for the outer layer of the lower IDC, or IDC2, and so on), and both hits of the two layers of each IDC are required to be consistent with the trajectory.

7. $R_{TOF}\Delta\phi_{TOFU} < W_{TOF}/2 + 10.0\text{mm}$,
 $R_{TOF}\Delta\phi_{TOFL} < W_{TOF}/2 + 10.0\text{mm}$

where R_{TOF} is the distance from the center of the instrument to the center of a TOF counter, $R_{TOF}\Delta\phi$ is the distance in ϕ -direction from the trajectory to the center of the nearest hit TOF counter, and W_{TOF} is the width of a TOF counter. In the $r\phi$ -plane, the extrapolated trajectory should pass through a hit TOF counter with an accuracy of 10mm.

Figures 4.12 to 4.18 show the histograms of these track-quality variables together with the cut boundaries. Open histograms are for the events that pass the single-track selection, and the shadowed histograms are for the events that remain after applying the track-quality cut.

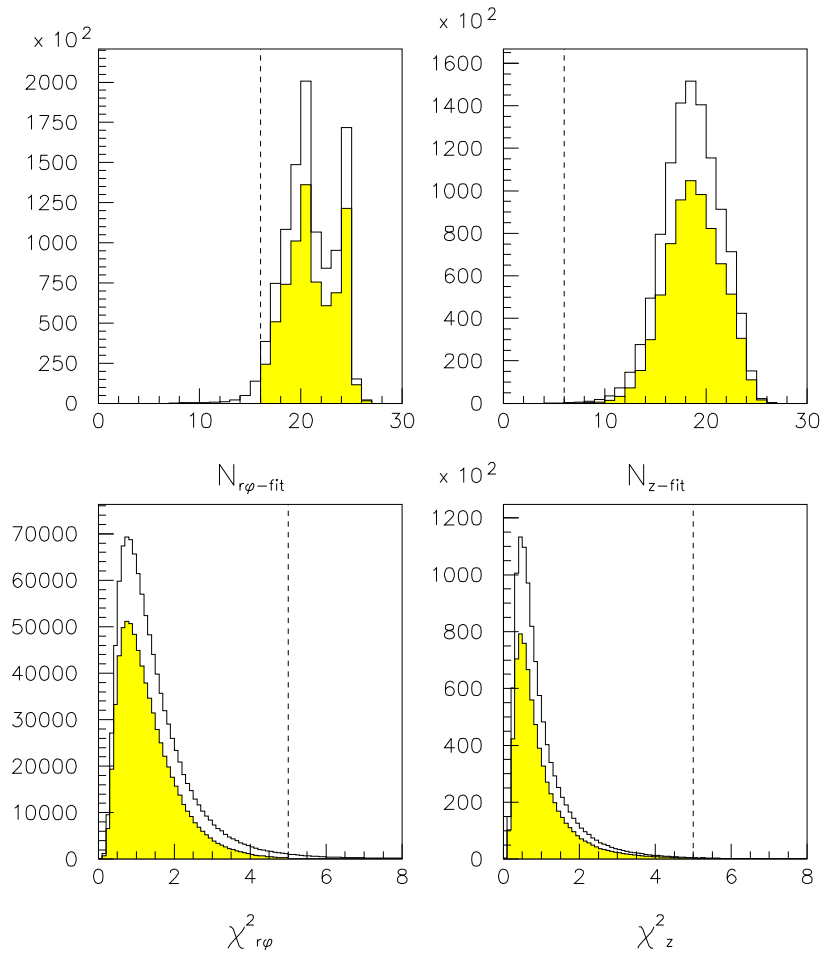


Figure 4.12: Track Quality Cut 1,2,3,4. ('97)

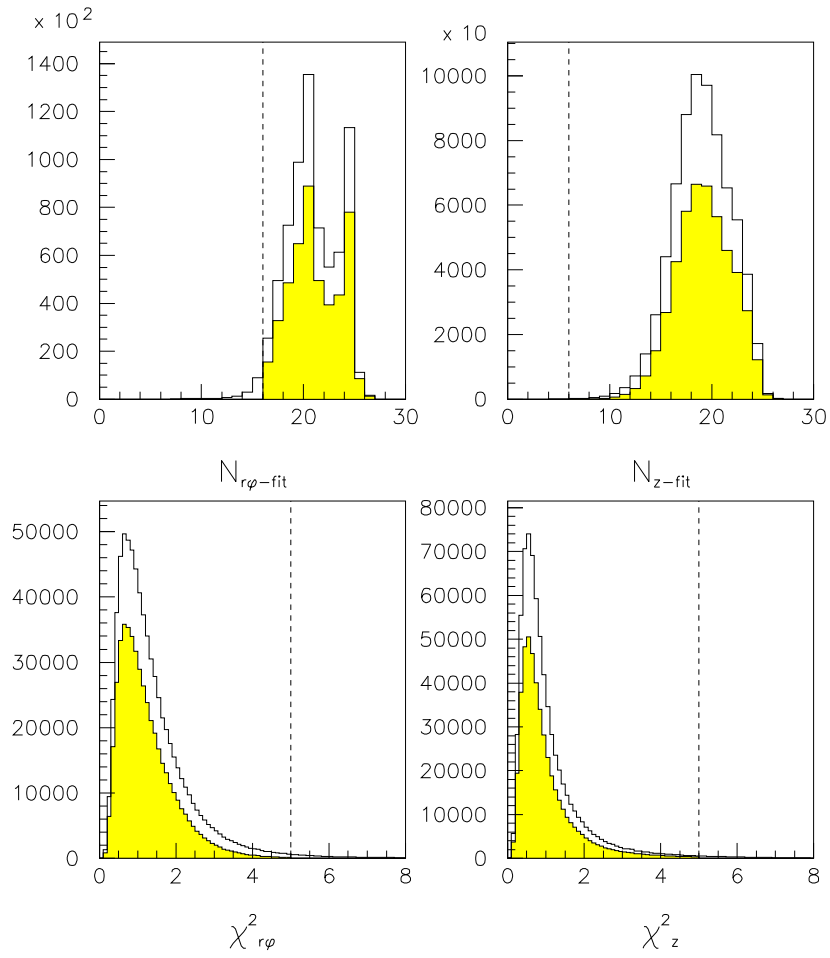


Figure 4.13: Track Quality Cut 1,2,3,4. ('98)

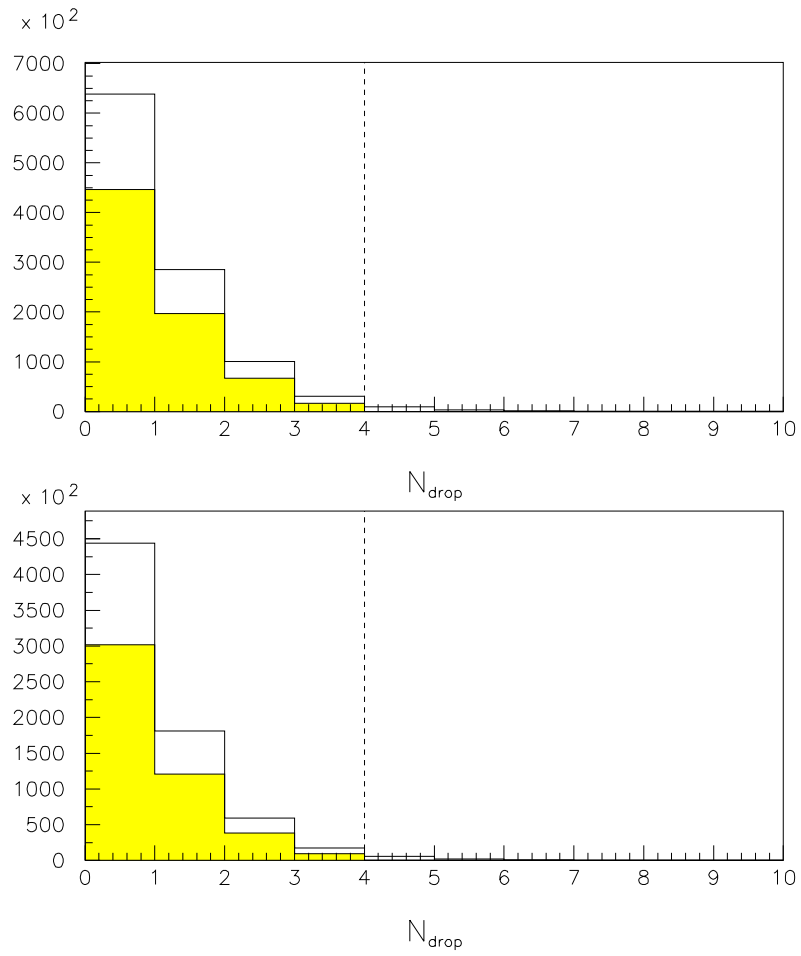


Figure 4.14: Track Quality Cut 5. ('97 (top) and '98(bottom))

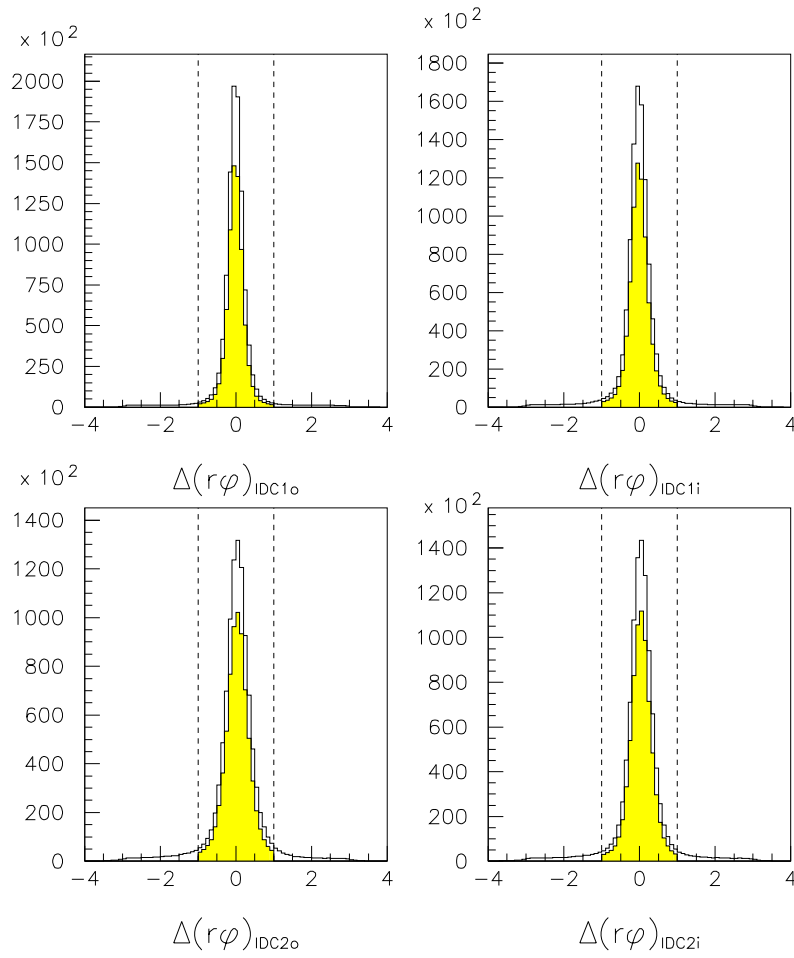


Figure 4.15: Track Quality Cut 6. ('97)

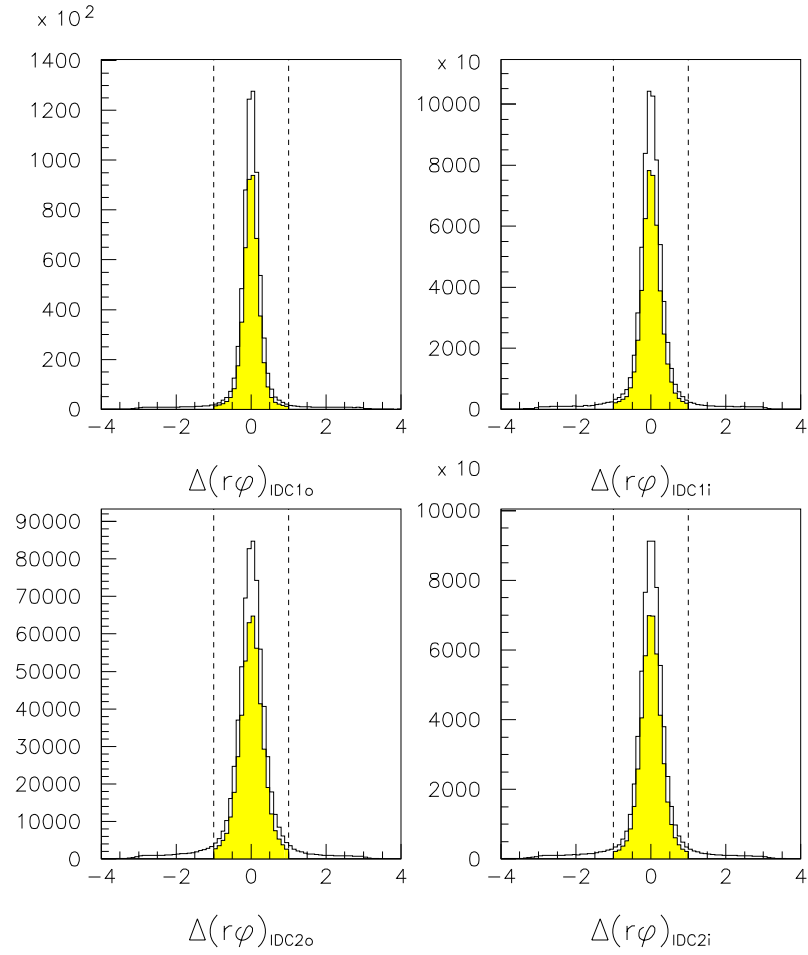


Figure 4.16: Track Quality Cut 6. ('98)

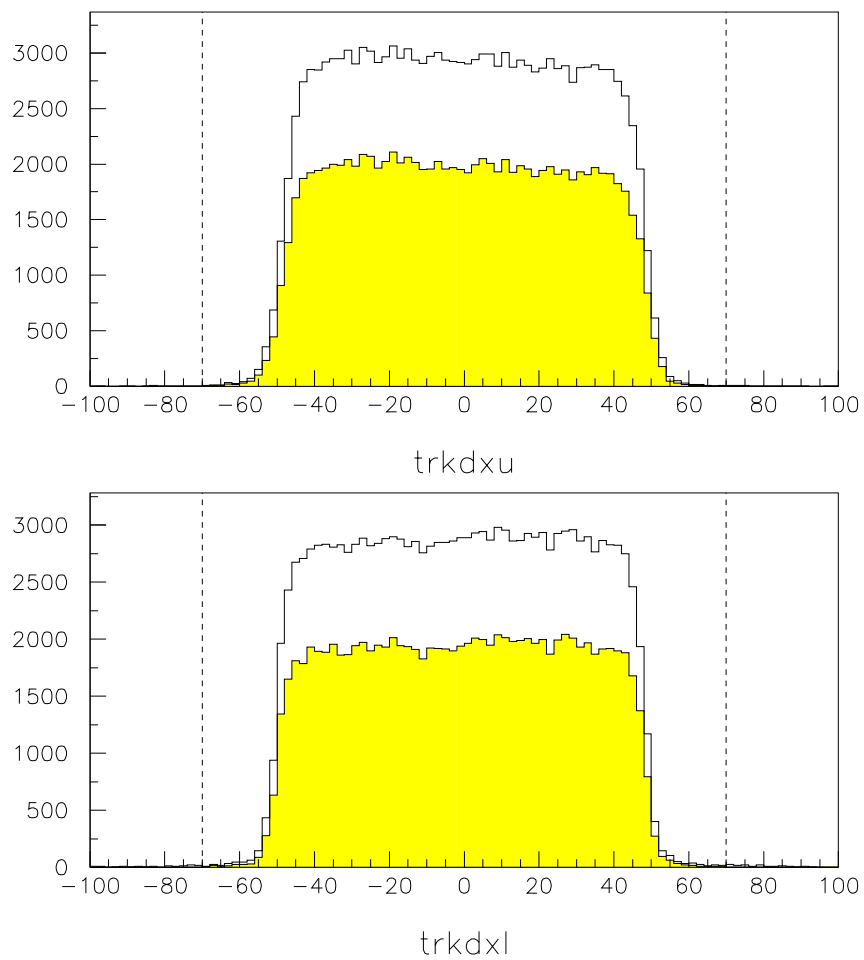


Figure 4.17: Track Quality Cut 7. ('97)

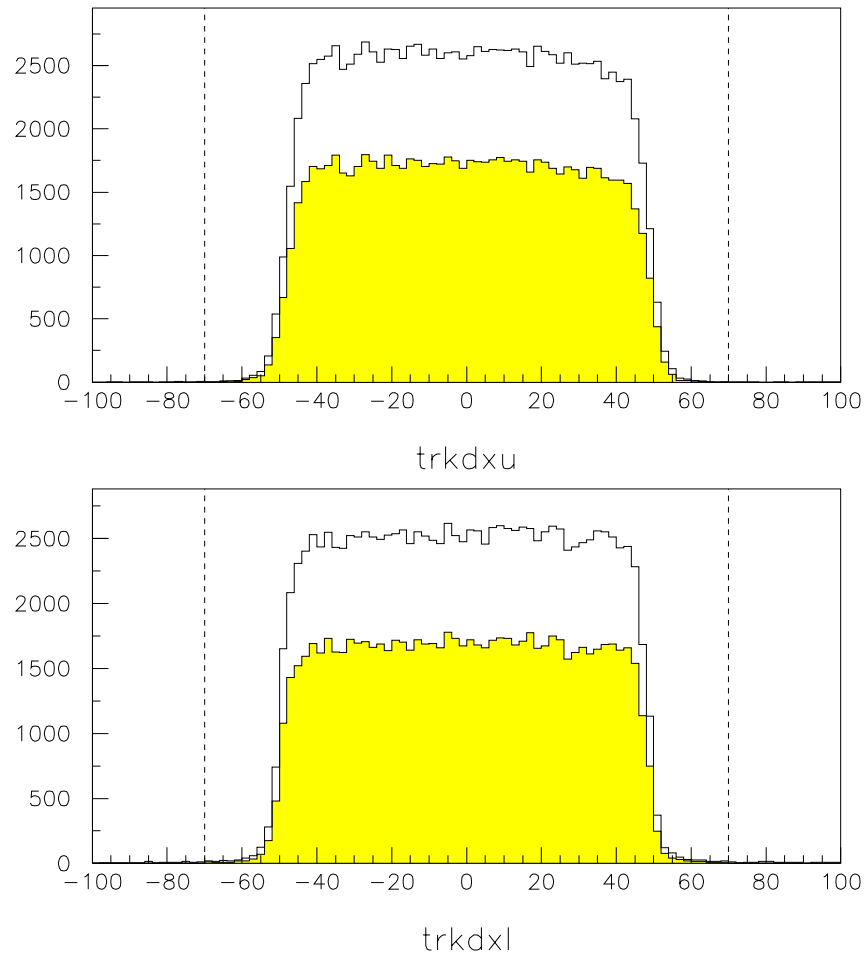


Figure 4.18: Track Quality Cut 7. ('98)

4.5 Antihelium Search

All selections up to this level do not discriminate the positive and negative rigidity. Figure 4.19 shows the $1/\text{rigidity}$ distribution with all selections but the track quality cut. Those events that are in the region of negative rigidity are apparently spilling over from the high energy region of positive rigidity due to the finite chamber resolution. Figure 4.20 shows the $1/\text{rigidity}$ distribution after all cuts. In this figure, because of the strict track quality cut criteria, the spillover from the high energy region is suppressed. This spillover can be suppressed more if stricter track quality cuts are applied, however such cuts sacrifice the high selection efficiency. The applied preselection was determined by a trade-off of the suppression of spillover and the high selection efficiency.

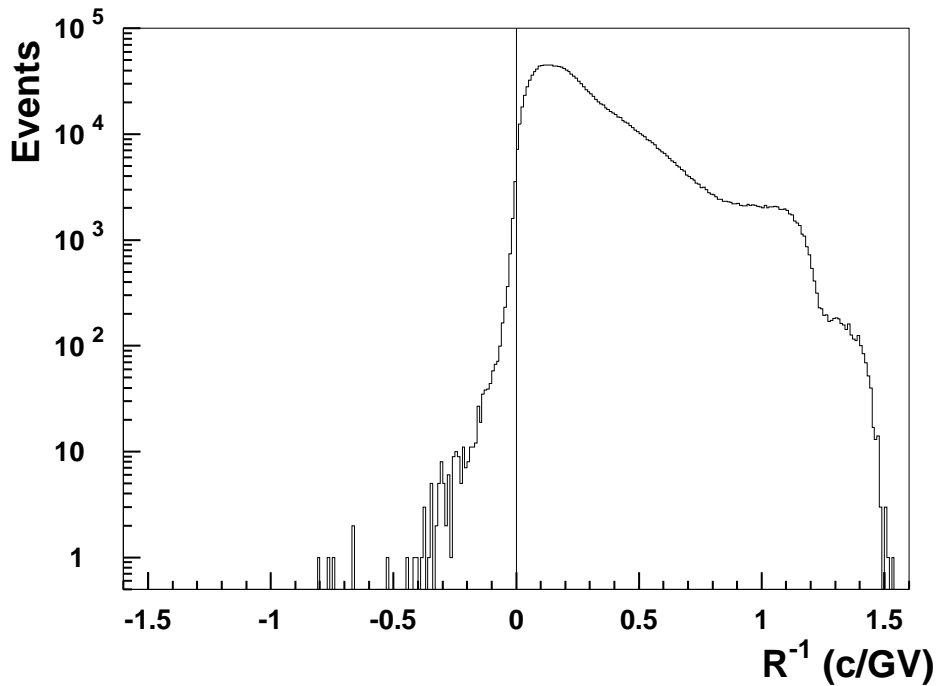


Figure 4.19: $1/\text{rigidity}$ distribution without track quality cut ('97 + '98)

The resultant edge of the spillover in the negative rigidity region in Figure 4.20 corresponds to the rigidity of -16 GV. Therefore, it is concluded that we have no antihelium candidate in the rigidity region below 16 GV. The other edge in the positive rigidity region is determined by the events that

stop in the bottom scintillator. The edge corresponds to the rigidity of 0.71 GV, as shown in the figure.

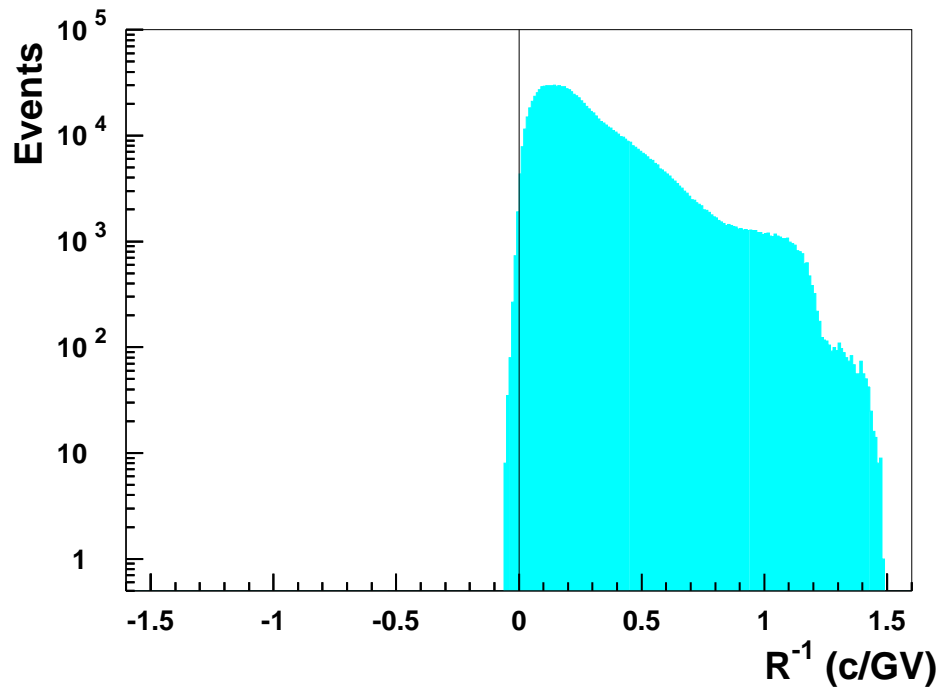


Figure 4.20: 1/rigidity distribution ('97 + '98)

Chapter 5

Determination of the upper limit on $\overline{\text{He}}/\text{He}$

As showed in Chapter 4, no antihelium candidates were found in detected data. The resultant upper limit for the ratio of antihelium to helium in cosmic rays $R_{\overline{\text{He}}/\text{He}}$ at the top of the atmosphere is

$$R_{\overline{\text{He}}/\text{He}} = \frac{\int N_{Obs,\overline{\text{He}}}/(S\Omega \times \overline{\eta} \times \overline{\epsilon}_{sn\text{gl}} \times \overline{\epsilon}_{trig} \times \overline{\epsilon}_{dE/dx} \times \overline{\epsilon}_{\beta} \times \overline{\epsilon}_{DQ})dE}{\int N_{Obs,\text{He}}/(S\Omega \times \eta \times \epsilon_{sn\text{gl}} \times \epsilon_{trig} \times \epsilon_{dE/dx} \times \epsilon_{\beta} \times \epsilon_{DQ})dE}, \quad (5.1)$$

where

1. N_{obs} is number of observed He ($\overline{\text{He}}$) events,
2. $S\Omega$ is geometrical acceptance of BESS detector,
3. $1 - \eta(1 - \overline{\eta})$ is a probability to lose by Air of He ($\overline{\text{He}}$).
4. $\epsilon_{sn\text{gl}}(\overline{\epsilon}_{sn\text{gl}})$ is single track efficiency of He ($\overline{\text{He}}$),.
5. $\epsilon_{trig}(\overline{\epsilon}_{trig})$ is trigger efficiency of He ($\overline{\text{He}}$).
6. $\epsilon_{dE/dx}(\overline{\epsilon}_{dE/dx})$ is dE/dx cut efficiency of He ($\overline{\text{He}}$),
7. $\epsilon_{\beta}(\overline{\epsilon}_{\beta})$ is β cut efficiency of He ($\overline{\text{He}}$),.
8. $\epsilon_{DQ}(\overline{\epsilon}_{DQ})$ is Data Quality Cut efficiency of He ($\overline{\text{He}}$),.

Numerator in (5.1) is total events number of antihelium which hits the top of atmosphere and denominator is that of helium.

5.1 Ionization Energy Loss

The observed helium (and antihelium if exist) had lost their energies while they had traversed typically 5 g/cm^2 of the atmosphere above the instrument and also 9.0 g/cm^2 of the upper half material of the instrument before they were detected at JET chamber in the solenoidal magnetic field. The energy of a particle after traveling into a depth x is given as:

$$E(x) = E(0) - \int_0^x \frac{dE}{dx}(E) dx.$$

The energy at the top of the atmosphere $E(0)$ is then derived by using $E(x)$, the energy measured at JET chamber, dE/dx , the ionization energy loss per unit depth, and x , the thickness of the materials. The actual thickness of the material for a particle to traverse depends on the inclination of the particle trajectory. The total energy loss is calculated for each event by summing up the energy losses at every steps in the detector components and in the atmosphere.

5.2 Monte Carlo Simulation

To determine the upper limit on $\overline{\text{He}}/\text{He}$, we have to know geometrical acceptance or probability to lose by Air or some efficiency mentioned above. Some of them is difficult to estimate only by the data. For that case, we need to rely on Monte Carlo simulation.

We have built a simulation model of the BESS instrument based on the GEANT/GHEISHA [31] code, assembling the detector components, support frames and others which are defined with the actual dimensions and materials. The effects of energy loss, multiple scattering, bremsstrahlung, δ -rays and nuclear interactions in the detector media were originally taken into account and nuclear interactions of helium nuclei were developed from these sources by matsumoto [33]. Interactions of antihelium nuclei were not taken into account on these code but easy to define except nuclear interactions. Nuclear interactions of antihelium nuclei was developed from these codes with following assumptions:

- The inelastic cross sections of antihelium obey the model of hard spheres with overlap [34].

$$\sigma(A_i, A_t) \propto (A_i^{1/3} + A_j^{1/3} - 0.71 \times (A_i^{-1/3} + A_j^{-1/3}))^2,$$

where $\sigma(A_i, A_t)$ is the cross section of an incident particle with atomic weight A_i to a target with atomic weight A_t .

- The elastic cross sections of antihelium is the same as that of helium.
- Antihelium was broken without fail when inelastic interaction was occurred.

Since the signals generated by the detector components include no measurement errors and statistical fluctuations, we smeared those signals with the detector resolutions to reproduce the measured detector performance. We adjusted following parameters to reproduce the detector responses:

- Resolution of the position measurement in JET chamber and IDC.
- Efficiency of detecting hits by JET chamber.
- Number of photo-electrons in each PMT for minimum ionizing particles.
- TOF counter resolution.

5.2.1 Geometrical Acceptance

The geometrical acceptance of the BESS instrument was calculated using Monte Carlo simulation by GEANT code. In calculation, we presumed there is no preference for direction cosmic ray particles come in the Earth's atmosphere, although in fact there is a little direction tendency caused by terrestrial magnetism. The result is shown in Fig.5.1, where we use the term 'energy' to refer to the energy at the top of the instrument (TOI). Energy dependence is not found to geometrical acceptance and about $0.25m^2sr$ for whole energy range.

5.2.2 Single Track Efficiency

As explained in Section 4.3.1, single track events were chosen to analyze events. To estimate this efficiency, we need to rely on the Monte Carlo simulations. Again, in calculation, we assumed no direction tendency for incident cosmic rays. The result is shown in Fig.5.2, where the energy refer to TOI. The efficiency of helium was decrease as Kinetic Energy was increase, and, caused by JET fiducial region cuts, it was decrease at low energy.

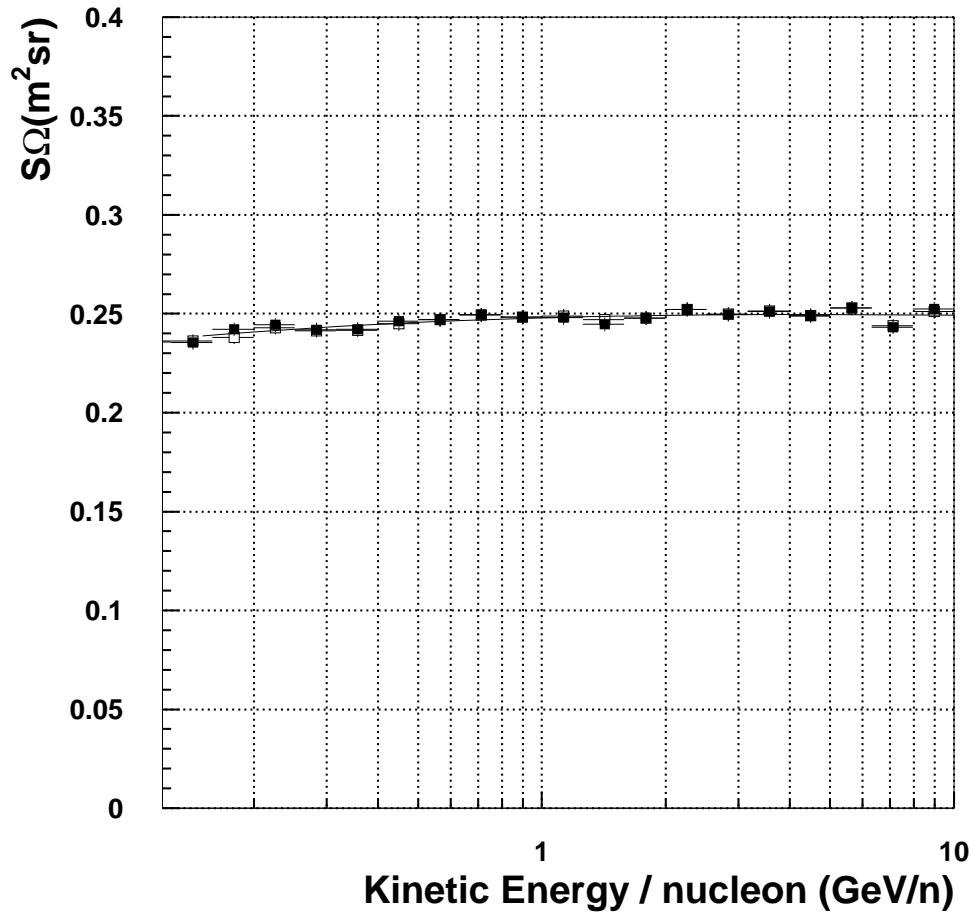


Figure 5.1: Acceptance

5.2.3 Loss of He and $\overline{\text{He}}$ in the air

Interactions in the $5\text{g}/\text{cm}^2$ of the atmosphere above the instrument reduce the number of helium (antihelium) to be observed in the experiment. On the other hand, the observed helium nuclei include the atmospheric secondary helium nuclei which are produced in the atmosphere above the instrument by collisions of the cosmic rays with air nuclei. For the helium, these effect had been studied by Matsumoto in detail [33], so we concentrate for the antihelium. Since we have no idea for the flux of cosmic ray anti-nuclei which are heavier than antihelium nuclei and, if exist, the contributions of the atmospheric secondary antihelium should be small compared with primary antihelium, we neglect it. We simulated the loss of antihelium with

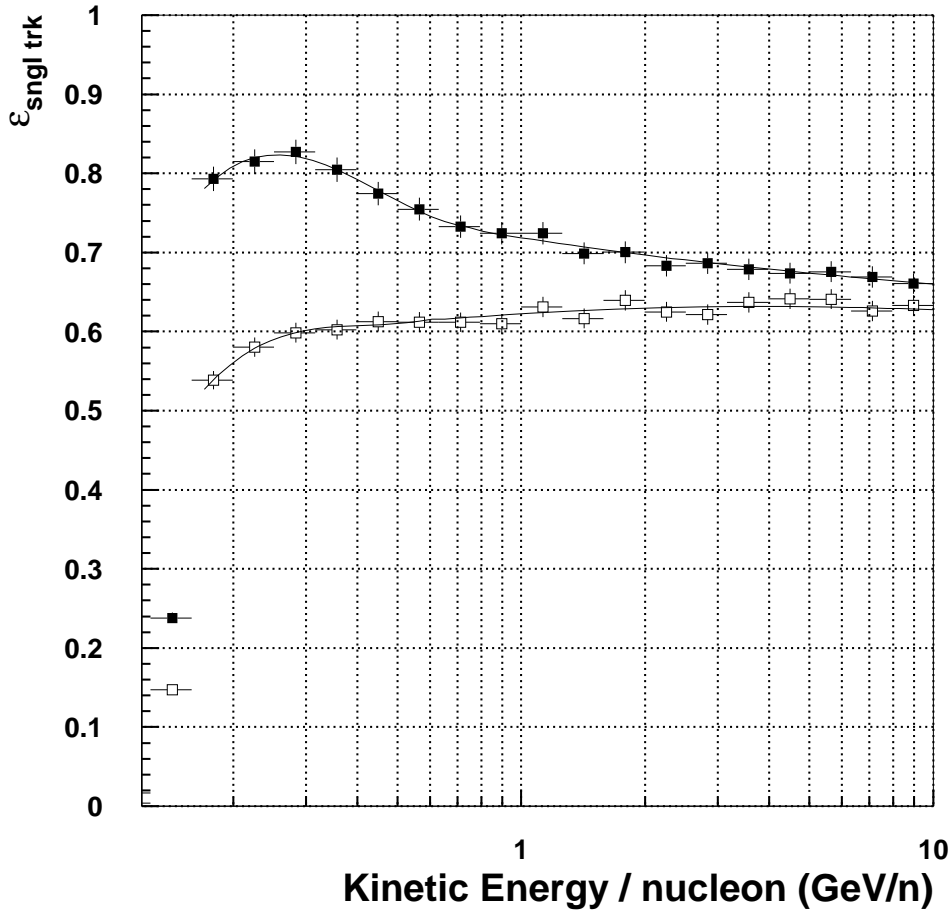


Figure 5.2: Single Efficiency

interactions of the atmosphere by the GEANT code with the standard model atmosphere. Figure 5.3 shows the survival probability of antihelium nuclei (open squares) together with that of helium (filled squares), where we use the term 'energy' to refer to the energy at the top of the atmosphere (TOA).

5.3 Trigger Efficiency

In this section we use the energy or rigidity refer to the value of the center of JET (COJ). As explain in Section 2.6.1, the trigger generation proceeds in three stages. The first stage was the T0 trigger which is generated by the coincidence of the top and bottom layers of TOF scintillators. We consider the

T0 trigger efficiency was 100%. The second stage was the T1 trigger (track trigger) which is generated by IDC/TOF hit informations. The track trigger efficiencies can be decomposed into the ‘hit-pattern selection efficiency (ϵ_{patt})’ and the ‘rigidity selection efficiency (ϵ_{rig})’. Shown in Figure 5.4 is the ϵ_{patt} efficiency determined by the unbiased helium sample. The ‘rigidity selection efficiency (ϵ_{rig})’ is estimated by fitting a theoretical efficiency function of track-rigidity selection with unbiased helium sample. Since the real data of helium events reside only in positive rigidity region, we assume that this fitted function is correct even in the negative rigidity region. Figure 5.5 shows the measured efficiency values and fitted efficiency curve of the track-rigidity selection as a function of rigidity⁻¹. The third stage was the on-line selection which is generated using the whole detector informations. The efficiency of on-line selection (ϵ_{online}) was determined by utilizing the whole of the unbiased samples with $|Z|=1$ and result was shown in Figure 5.6. Note that, in 1997 flight, for the first half of the flight (Run2 \sim 16) the efficiency is 100%, because Transputer bank turned off during this period (i.e., all events passed track trigger were accepted during the period).

The total trigger efficiency of antihelium were then

$$\bar{\epsilon}_{trig} = \epsilon_{patt} \times \epsilon_{rig},$$

for the first half of the 1997 flight (Run2 \sim 16) and

$$\bar{\epsilon}_{trig} = \epsilon_{patt} \times \epsilon_{rig} \times \epsilon_{online}$$

for the last half of the 1997 flight and whole period of the 1998 flight.

For selecting helium events, we used only the ‘unbiased trigger (CD)’. So the trigger efficiency (ϵ_{trig}) only depend on the sampling rate (N_{CD}). The trigger efficiency of helium were

$$\epsilon_{trig} = N_{CD},$$

for whole periods of the flights. The value of N_{CD} was 1/25.

5.4 Off-line Selection Efficiency

5.4.1 β Cut Efficiency

The efficiency of the β -cut is derived from the actual flight data for helium events. $1/\beta$ has Gaussian distribution, and cut lines defined

$$\frac{1}{\beta} - \sqrt{\left(\frac{m}{e}\right)^2 \frac{1}{R^2} + 1} < 3.89\sigma(\beta^{-1})$$

for upper-cut, where β , m and e are the value of ${}^4\text{He}$, and

$$\frac{1}{\beta} - \sqrt{\left(\frac{m}{e}\right)^2 \frac{1}{R^2} + 1} > 3.89\sigma(\beta^{-1})$$

for lower-cut, where β , m and e are of ${}^3\text{He}$.

5.4.2 dE/dx Cut Efficiency

The efficiency of the dE/dx-cut is derived from the actual flight data for helium events, too. The distribution of TOF dE/dx are well described as Gaussian distribution at low energy, and as Landau-Vavilov distribution at high energy. The cut lines defined as efficiency 99.9 %. In order to determine the JET dE/dx-cut efficiency, we select helium events using tight-cut of TOF dE/dx and β (efficiency 63.5% for each), and for those events, we perform the JET dE/dx-cut. The efficiency of JET dE/dx-cut was evaluated by dividing the number of events after the JET dE/dx by the number before the cut. The efficiency around 100% was achieved.

5.4.3 Track Quality Cut Efficiency

The quality cut was applied to squeeze out the best performance of rigidity determination especially in high rigidity region. The efficiency of the quality cut is evaluated by just dividing the number of events after the quality cut by the number before the cut. The various quality cuts efficiencies are shown in Figure 5.7 and the total quality cut efficiency in Figure 5.8, where we use the energy refer to COJ.

5.5 Upper limit on $\overline{\text{He}}/\text{He}$

Now we are ready to determine the upper limit on the $\overline{\text{He}}/\text{He}$. All we have to do is to integrate the Eq.5.1. The integration interval correspond to the rigidity region which no antihelium candidate was found, and are determined by the 1/rigidity distribution (See Fig. 4.20). The upper bound of integral is determined by the edge of the spillover in the negative rigidity region and the lower bound of integral is determined by the edge of the events in the

positive rigidity region which correspond to the event stopped in the bottom scintillator. They are 7.5 GeV/n and 0.14 GeV/n at TOA respectively. In calculation, however, we determined the lower bound of integral 0.18 GeV/n at TOA which correspond to the rigidity 1 GV/c at COJ. The reason why is some efficiencies are not high enough in low rigidity regions. (See Fig. 5.2) The geometrical acceptance of the BESS instrument slightly depends on the energy, however, we think of it as constant in the energy regions of integral (see Fig.5.1), then we have

$$R_{\overline{\text{He}}/\text{He}} = \frac{\int N_{Obs,\overline{\text{He}}} / (\overline{\eta} \times \overline{\epsilon}_{sn\text{gl}} \times \overline{\epsilon}_{trig} \times \overline{\epsilon}_{dE/dx} \times \overline{\epsilon}_{\beta} \times \overline{\epsilon}_{DQ}) dE}{\int N_{Obs,\text{He}} / (\eta \times \epsilon_{sn\text{gl}} \times \epsilon_{trig} \times \epsilon_{dE/dx} \times \epsilon_{\beta} \times \epsilon_{DQ}) dE}. \quad (5.2)$$

We should note that values we determined above section (N_{obs} , $\epsilon_{sn\text{gl}}$, ϵ_{trig} and ϵ_{DQ}) are not the values at TOA, but TOI or COJ. However, we explained in section 5.1, we calculated the ionization energy loss for each event, we could know the energy at TOA, TOI and COJ for each event. Taking account of it, we could integrate the equation 5.2 using the values we determined above. The integral of the denominator in Eq. 5.2 were 3.4×10^6 in 1997 flight and 3.0×10^6 in 1998 flight, respectively.

Since no antihelium candidate was found, we take 3.1 as the number of antiheliums (\overline{N}_{obs}) for the calculation of the 95 % confidence level upper limit. This means that we assume a Poisson distribution with the mean value of 3.1 for the expected number of antiheliums, where zero observed result will be expected at the probability of 5 %. To integrate the numerator in Eq. 5.2, we must assume the energy spectrum of antihelium, since the efficiencies are functions of energy. In order to obtain the most conservative limit, we take the minimum value of the antihelium efficiency-product in the energy region. Figure 5.9 shows efficiency-product together with each efficiency. We take the minimum value of 0.22 to integrate the numerator. The integral of the denominator in Eq. 5.2 (N_{helium}) and the minimum efficiency-product of antihelium ($\overline{\epsilon}_{min}$) are summarised in table 5.1. Combined with previous data, the resultant upper limit $R_{\overline{\text{He}}/\text{He}}$ is

$$R_{\overline{\text{He}}/\text{He}} < \frac{3.1 / \left(\overline{\epsilon}_{min}^{95} \times N_{helium}^{95} / N_{helium}^{total} + \overline{\epsilon}_{min}^{97,98} \times N_{helium}^{97,98} / N_{helium}^{total} \right)}{N_{helium}^{total}} \quad (5.3)$$

$$= 1.3 \times 10^{-6}$$

We can also give a upper limit with model dependent assumption that the \overline{He} energy spectrum coincide with the He spectrum. Under this assumption, Eq. 5.2 becomes

$$R_{\overline{He}/He} < \int \frac{3.1dE}{N_{Obs,He} \times \overline{\eta} \times \overline{\epsilon}_{snl} \times \overline{\epsilon}_{trig} / (\eta \times \epsilon_{snl} \times \epsilon_{trig})}. \quad (5.4)$$

The result was summarized in table 5.2.

Table 5.1: Summary of the number of heliums and minimum efficiency-product of antihelium.

flight year	total helium numbers N_{helium}	minimum efficiency-product $\overline{\epsilon}_{min}$
~ 1995	5.1×10^6	0.19
1997	3.3×10^6	0.24
1998	2.9×10^6	0.24

Table 5.2: Summary of the calculation of upper limit with model dependent assumption.

flight year	$\int N_{Obs,He} \times \overline{\eta} \times \overline{\epsilon}_{snl} \times \overline{\epsilon}_{trig} / (\eta \times \epsilon_{snl} \times \epsilon_{trig})$
~1995	1.5×10^6
1997	1.1×10^6
1998	0.93×10^6

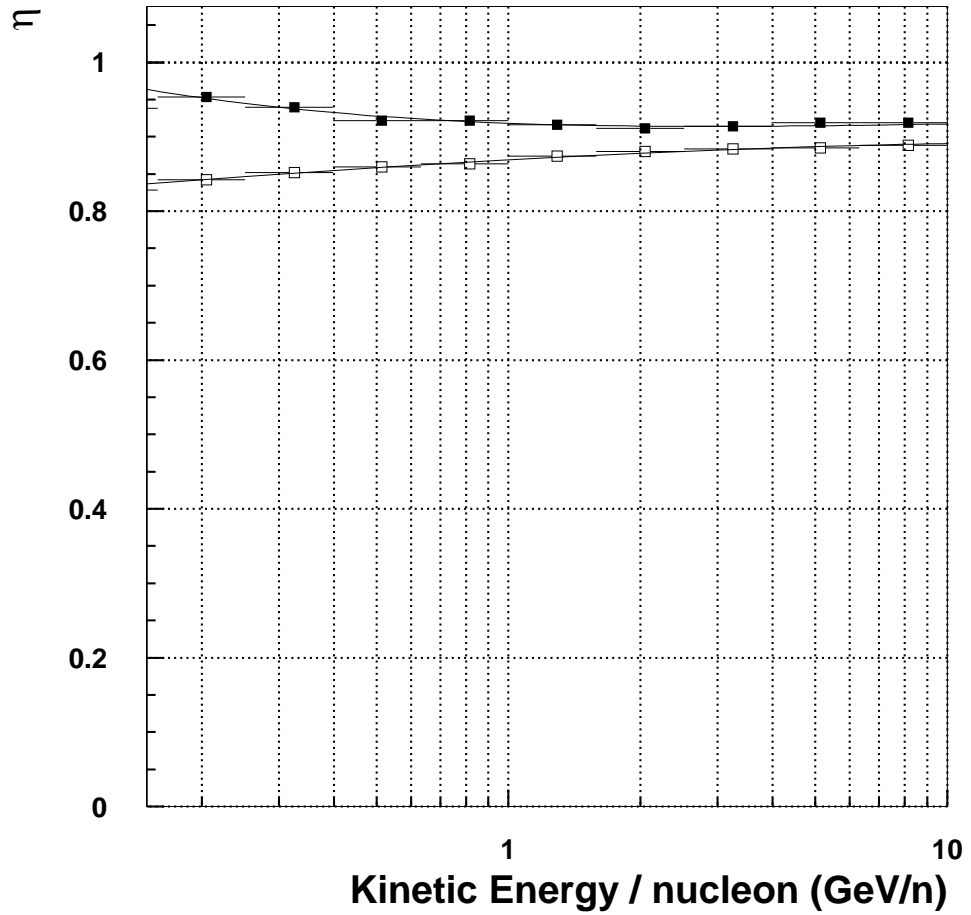


Figure 5.3: Survival probability of helium nuclei (filled squares) and anti-helium (open squares) for 5 g/cm^2 of the atmosphere.

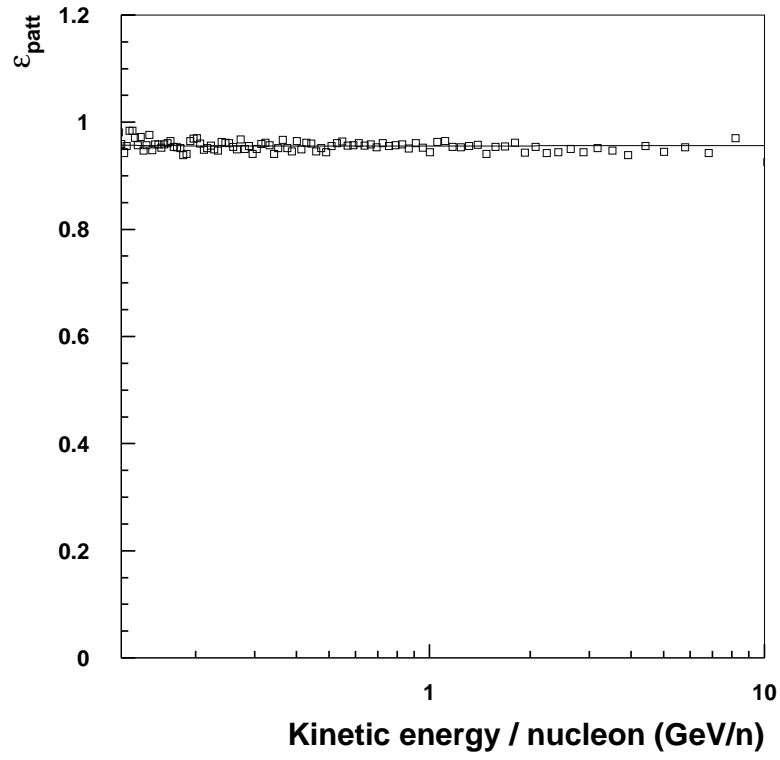


Figure 5.4: Track pattern selection efficiency.

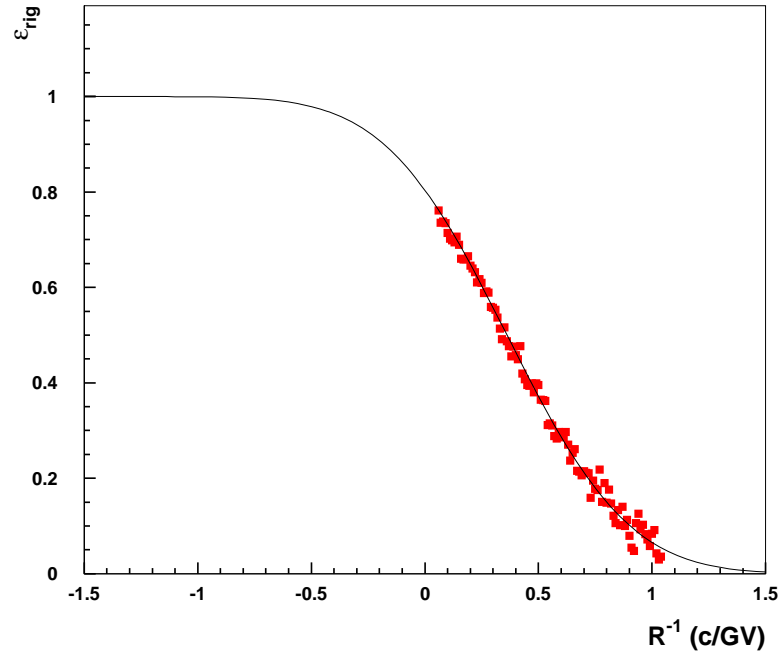


Figure 5.5: Track rigidity selection efficiency.

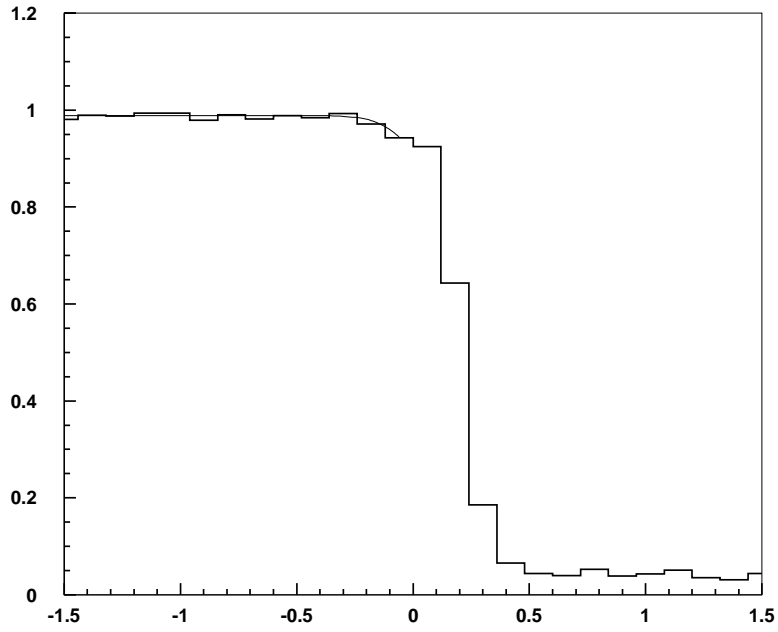


Figure 5.6: Online selection efficiency.

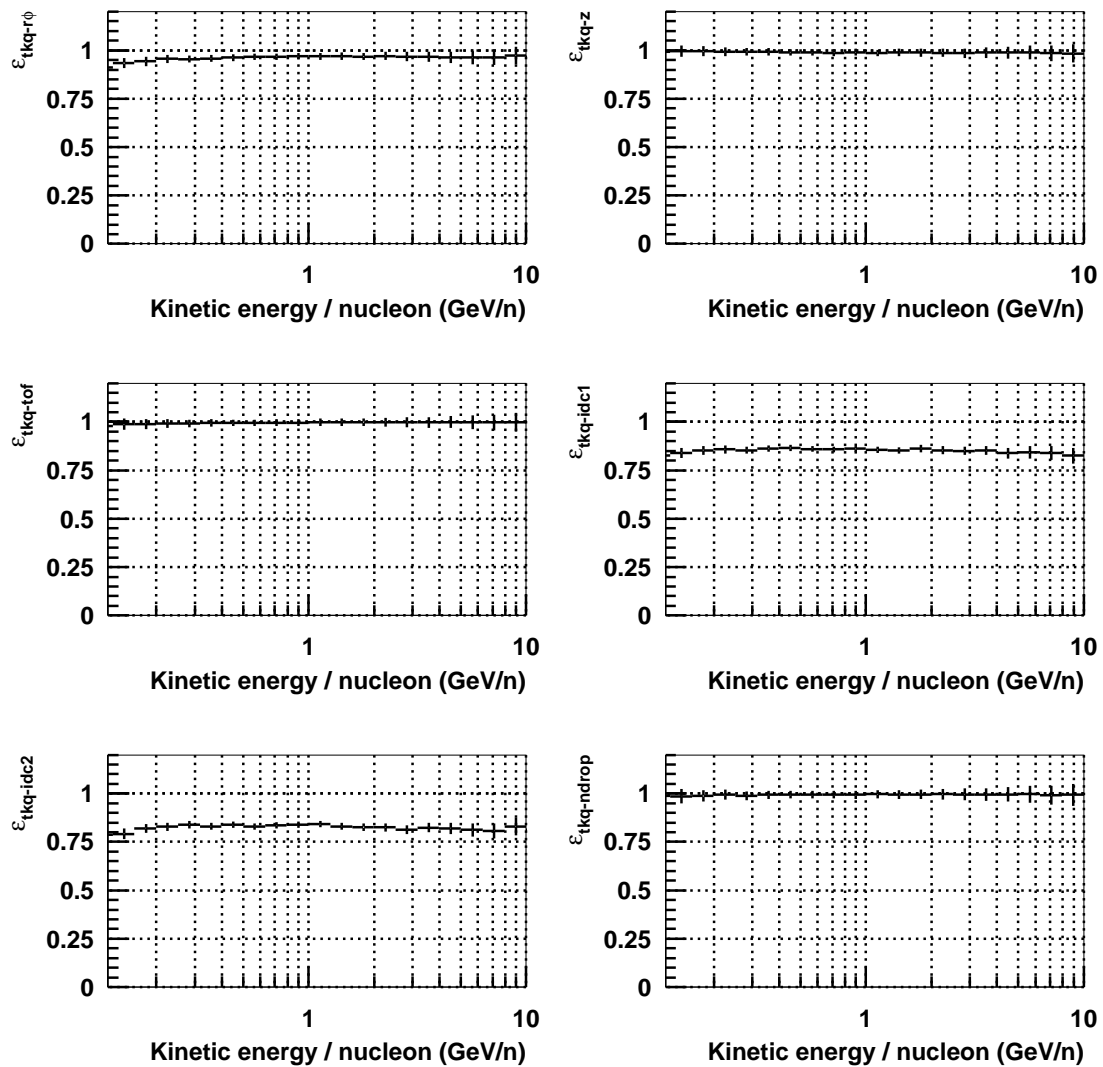


Figure 5.7: The efficiency of the various quality cuts

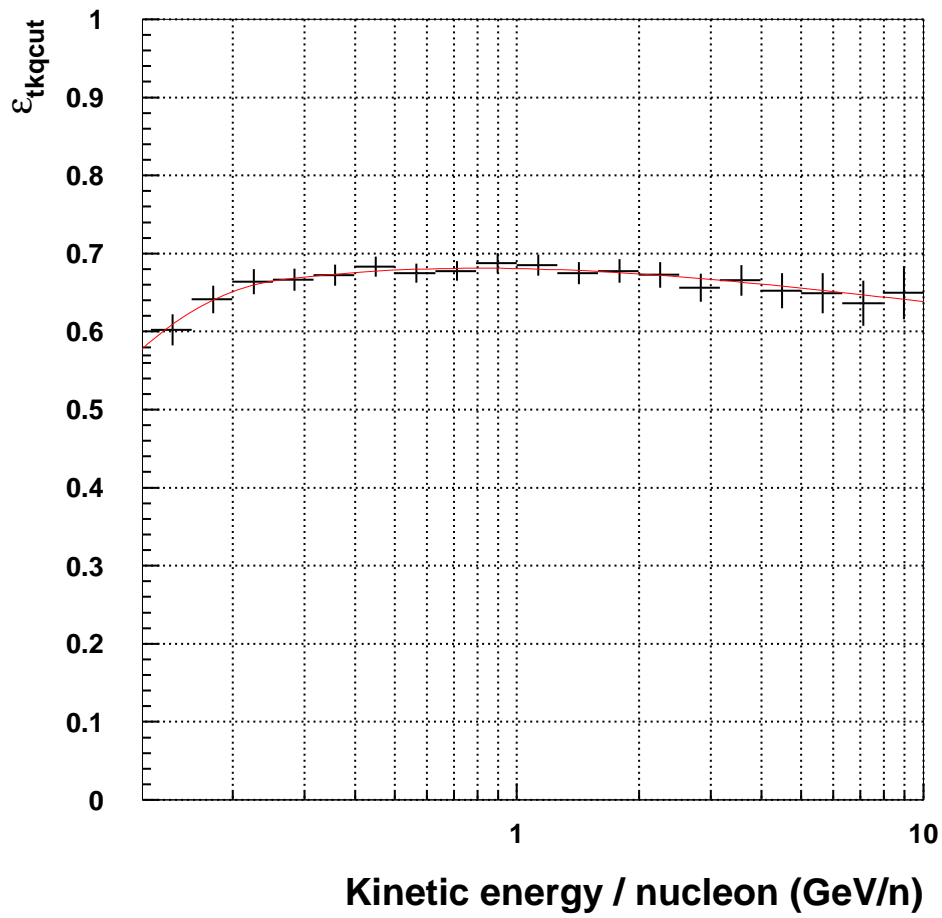


Figure 5.8: The efficiency of the all quality cut

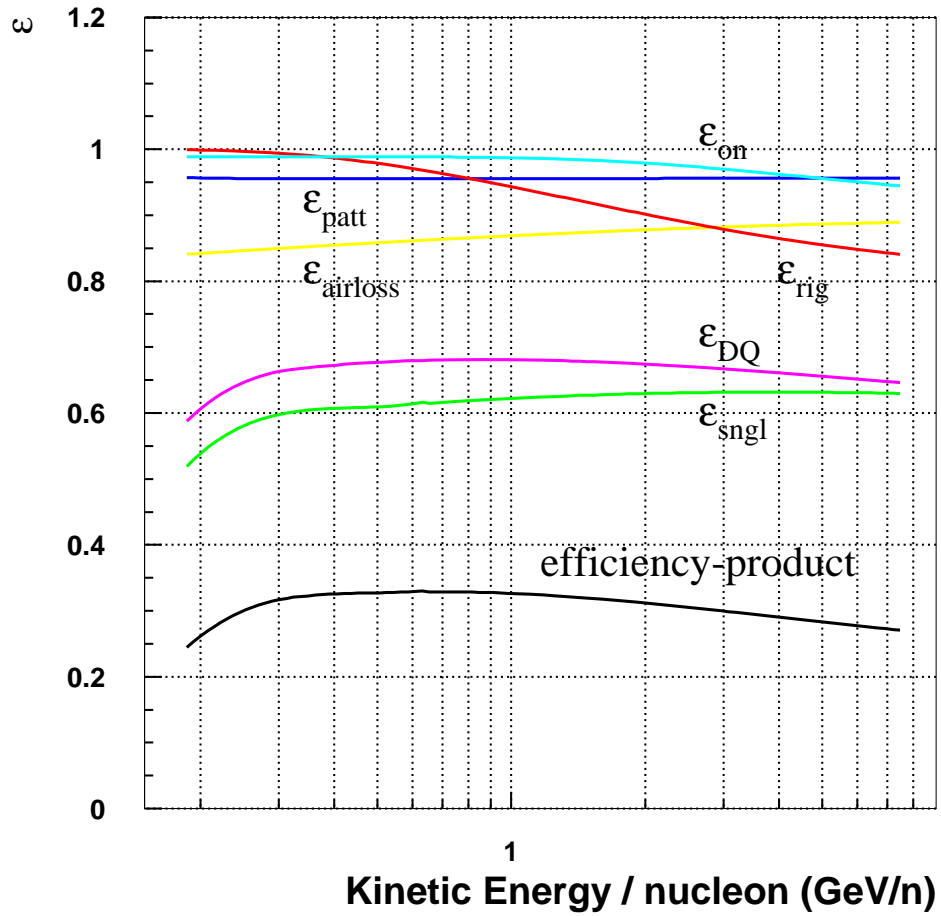


Figure 5.9: The antihelium efficiency-product in the energy region.

Chapter 6

Results

The total number of helium nuclei observed in the BESS '97 and '98 flight data is 6.2×10^6 in the rigidity region from 0.7 GV to 16 GV. Since we found no antihelium candidate with a rigidity below 16 GV, only the upper limit can be set using equation 5.1 in this rigidity region. The resultant 95 % confidence level upper limit on the $\overline{\text{He}}/\text{He}$ flux ratio at the top of the atmosphere is 1.3×10^{-6} in the rigidity range from 1 to 16 GV which does not depend on the unknown $\overline{\text{He}}$ energy spectrum, and 8.8×10^{-7} with the model dependent assumption that the $\overline{\text{He}}$ energy spectrum coincide with the He spectrum. This result is shown 6.1 and compared with previous limits. As seen in the figure, this work has improved the previous BESS result about a factor of 3. It is the most direct and stringent evidence that our Galaxy (or nearby part of Universe?) consist only of the matter.

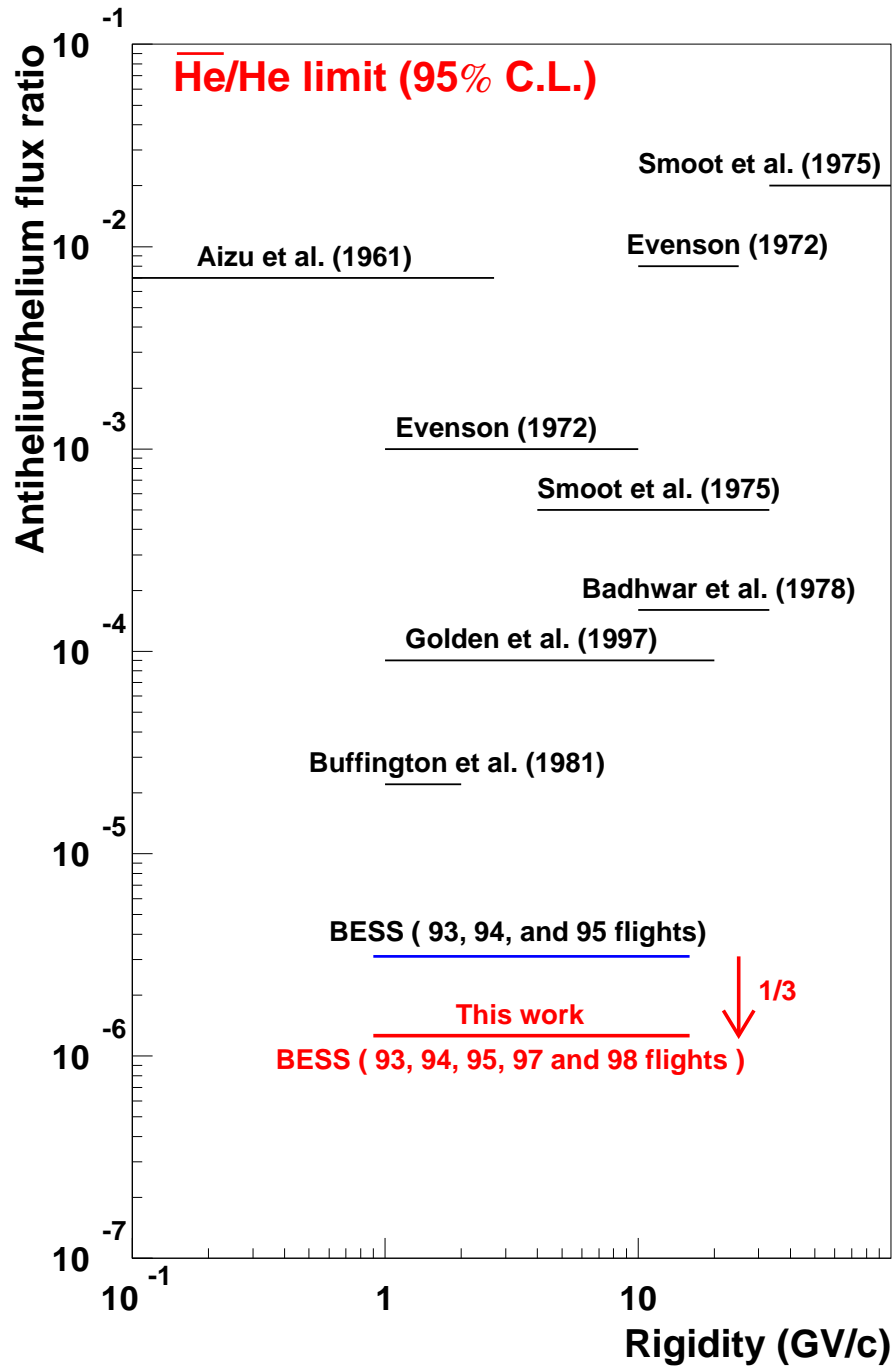


Figure 6.1: Upper limit

Acknowledgements

I wish to express my sincere thanks to Professor S. Orito who has led the BESS experiment, for his guidance throughout my research reported in this thesis. I also wish to gratefully appreciate Professor A. Yamamoto and Professor T. Yoshida who have managed the campaign and lead it to a success. The analysis were done owing a lot to Prof. S. Orito, Prof. M. Nozaki, Dr. K. Yoshimura, Dr. H. Matsunaga, Dr. M. Motoki, Dr. T. Sanuki, and Dr. H. Matsumoto. I would like to acknowledge them for their suggestions and helpful discussions and assistance at the various stages of the analysis.

I would like to thank all the BESS colleagues for their effort to make a success of the experiment.

Furthermore, I am grateful to Dr. V. Jones and all other people at NASA who supported BESS, and to the balloon campaign team from the National Scientific Balloon Facility for their professional and skillful work in carrying out the BESS flights. I greatly acknowledge Prof. A. Nishida, Director General of ISAS, Prof. H. Sugawara, Director General of KEK, and Prof. S. Iwata of KEK for their support and encouragement. Sincere thanks go to International Center for Elementary Particle Physics (ICEPP) of University of Tokyo for kindly allowing me to use their workstations. The data of the CLIMAX neutron monitor were provided by Space Physics Data System of University of Chicago, supported by National Science Foundation Grant ATM-9420790. The BESS experiment has been supported by Monbusho International Scientific Research Grant and Scientific Research Grant, Kurata Research Grant, and Sumitomo Research Grant.

References

- [1] A.D. Sakharov ZhETF Pis'ma 5, No.1 (1967) 32-35.
- [2] H. Aizu et al., Phys. Rev. **121** (1961) 1206.
- [3] P. Evenson, Astrophys. J. **176** (1972) 797-808.
- [4] G.F. Smoot et al., Phys. Rev. Lett. **35** (1975) 258.
- [5] G.D. Badhwar, R.L. Golden et al., Nature **274** (1978) 137.
- [6] R.L. Golden et al. Astrophys. J. **479** (1997) 992.
- [7] A. Buffington et al. Astrophys. J. **248** (1981) 1179.
- [8] T. Saeki, et al., Phys. Lett. B 422 (1998) 319-324.
- [9] A. Yamamoto et al, Adv. Space Res., **14** (1994) (2)75.
- [10] A. Buffington et al, The Astrophys. J. **199** (1975) 669.
- [11] R.L. Golden et al, Nucl. Instr. Method, **148** (1978) 179.
- [12] M.H. Salamon et al, The Astrophys. J. **349** (1990) 78.
- [13] R.L. Golden et al, Nucl. Instr. Method, **A306** (1991) 366.
- [14] S.W. Barwick et al, Nucl. Instr. Method, **A400** (1997) 34.
- [15] A. Yamamoto et al, IEEE Trans. Mag. **24** (1988) 1421.
- [16] Y. Makida et al, Adv. Cryog. Eng., **37** (1992) 401.
- [17] Y. Makida et al, IEEE Trans. Applied Superconductivity **5** (1995) 658.
- [18] EUROTOM reports, EUR-4100e (1972).

- [19] R.J. Yarema, FERMILAB-TM-1284 (1984).
- [20] M. Imori *et al.*, IEEE Trans. Nucl. Sci. **39** (1992) 987.
- [21] T. Massam, GUIDE7: a general program for evaluating the properties of scintillation and Čerenkov counter optical systems, CERN 76-21 (1976).
- [22] H. Matsumoto *et al.*, IEEE Trans. Nucl. Sci., **43** (1996) 2195.
- [23] K. Anraku, S. Inaba and M. Imori, IEEE Trans. Nucl. Sci. **40** (1993) 717.
- [24] I. Adachi *et al.*, Nucl. Instr. and Meth. A 355 (1995) 390.
- [25] INMOS, Transputer Reference Manual, Prentice Hall (1998).
- [26] G. Jones and M. Goldsmith, Programming in Occam2, Prentice Hall (1998).
- [27] V. Karimäki, Comput. Phys. Commun., **69** (1992) 133.
- [28] Goossens, M., *ZEBRA - Overview of the ZEBRA system*, CERN Program Library Q100/Q101. CERN, 1993
- [29] Application Software Group, *HEPDB - Database Management Package*, CERN Program Library Q180. CERN, 1993
- [30] Karimäki, V., Nucl. Instr. and Meth. **A305**, 187 (1991).
- [31] Bruyant, F., *et al*, *GEANT - Detector Description and Simulation Tool*, CERN Program Library W5013. CERN, 1993
- [32] Karimäki, V., Nucl. Instr. and Meth. **A305**, 187 (1991)
- [33] H. Matsumoto, A doctoral thesis of Kobe University, (1999)
- [34] N.S. Grigalashvili *et al.* Yad. Fiz. **48** (1998) 476-482.
- [35] R.L. Golden *et al.*, The Astrophys. J. **248** (1997) 992.